ATOMISTIC SIMULATION OF SURFACES EFFECTS ON MAGNETIC PROPERTIES OF ALLOY NANOMATERIALS

by

Zhenyu Liu

B.S. in Materials Science and Engineering, Tsinghua University, 2010

M.S. in Materials Science and Engineering, University of Florida, 2012

Submitted to the Graduate Faculty of

Swanson School of Engineering in partial fulfillment

of the requirements for the degree of

Doctor of Philosophy

University of Pittsburgh

2017

UNIVERSITY OF PITTSBURGH

SWANSON SCHOOL OF ENGINEERING

This dissertation was presented

by

Zhenyu Liu

It was defended on

November 9, 2017

and approved by

Scott Mao, Ph.D., Professor,

Department of Mechanical Engineering and Materials Science

Wei Xiong, Ph.D., Assistant Professor,

Department of Mechanical Engineering and Materials Science

Markus Chmielus, Ph.D., Assistant Professor,

Department of Mechanical Engineering and Materials Science

Giannis Mpourmpakis, Ph.D., Assistant Professor,

Department of Chemical and Petroleum Engineering

Dissertation Director: Guofeng Wang, Ph.D., Associate Professor,

Department of Mechanical Engineering and Materials Science

ATOMISTIC SIMULATION OF SURFACE EFFECTS ON MAGNETIC PROPERTIES OF ALLOY NANOMATERIALS

Zhenyu Liu, PhD

University of Pittsburgh, 2017

In the magnetic recording industry, $L1_0$ ordered CoPt and FePt nanoparticles have been considered as promising material candidates to advance the recording density beyond 1Tbit/in^2. Compared with their bulk form, these alloy nanoparticles exhibit inferior magnetic properties. Surface effects, which are much more pronounced in nanometer scale, have been suggested to contribute to the deteriorated properties. In this work, surface related phenomena in these alloys are explored using atomistic simulation method.

Density Functional Theory (DFT) calculations on the surface segregation effect have been performed in cuboidal, cuboctahedral nanoparticles and the related low index surfaces of $L1_0$ ordered CoPt alloy. Pt surface segregation to the outermost surface is found thermodynamically favorable in both nanoparticles and crystallographic surfaces. This segregation causes directly the break in structural, chemical ordering and accordingly the reduction in magnetic moment and change in magnetic anisotropy. Under 2nd order perturbation theory, the magnetic anisotropy energy on surface slabs has been associated with the change in d_{z^2} state density of surface Co atoms in the minority spin channel. Moreover, the magnetic properties of CoPt and FePt nanoparticles are demonstrated to be affected by particle shape using DFT calculations. This shape dependent magnetism is found correlated with the contraction in atomic spacing and local chemical composition. In addition, the surface spin canting mechanisms are identified for CoPt and FePt cuboctahedral nanoparticles. The different spin canting fashions for these two materials have been reproduced by micromagnetic simulation using Néel's surface anisotropy model. The relationship

between magnetoelastic coupling and Néel's anisotropy constant in tetragonal lattice has been established. Through the calculation of Néel's anisotropy constant from first principles, the different spin canting mechanisms have been explained. Finally, the effect of doping Cu, Ag and Au atoms on CoPt and FePt surfaces has been investigated. The Pt surface segregation has been found suppressed by the impurity atoms and the magnetic moment of surface Co/Fe atoms is restored up to the value of corresponding bulk-terminated surface. These additive atoms are proved to be beneficial for the improvement of magnetic properties on CoPt (001) surface and FePt (100) surface.

Keywords: Density Functional Theory, Micromagnetic Simulation, Surface Magnetism, Surface Segregation, Magnetic Anisotropy, Magnetic Moment, Cobalt Platinum Alloy, Iron Platinum Alloy, Néel's surface anisotropy, Magnetic Nanoparticle

TABLE OF CONTENTS

LIST OF TABLES

LIST OF FIGURES

PREFACE

Pursuing a Ph.D. degree at University of Pittsburgh has been a memorable journey. To me, this degree is a long-awaited dream since my childhood and I'm really glad I could finally achieve it. I'm reaching the end point of student status, but my research and exploration of the unknowns will never end in my lifetime.

At this very special juncture in life, I would like to express my acknowledgement to people who helped me, accompanied me during my 5 years' study.

First and foremost, I'm sincerely grateful to my advisor Prof. Guofeng Wang for the opportunity to pursue my dream and for the patient guidance and inspiration he provided. I'm thankful to my doctoral committee, Dr. Scott Mao, Dr. Wei Xiong, Dr. Markus Chmielus and Dr. Giannis Mpourmpakis for their insightful suggestion and comments on my research.

I feel lucky to work with those intelligent members in Prof. Guofeng Wang's group: Dr. Shyam Kattel, Dr. Zhiyao Duan, Dr. Yinkai Lei, Dr. Corinne Gray, Kexi Liu, Siming Zhang and Boyang Li. I'm thankful for their help and valuable discussion in this work. My special thank goes to Dr. Yinkai Lei who generously shared his broad and deep knowledge with me.

I would like to thank my friends at Pittsburgh, especially Dr. Baomin Wang, Dr. Tongchuan Gao, Ruichen Sun, Dr. Can Liu and Dr. Bing Ma for the joyful time we spent together.

Finally, I reserve my deepest gratitude to my parents for their unconditional love and support. Thank you for giving me the world.

1.0 INTRODUCTION

Plenty of information was created every day since the incoming of big data era. Not only is it important to analyze these data but also, one of the most important challenge is where these data could be stored. Various data storage devices have been invented, among whom the magnetic recording, particularly hard disk drive (HDD) has become the core media. Massive application of HDD in house-hold electronics and cloud storage has been realized because of its high reliability, low cost, and high capacity.

The first commercialized magnetic HDD was built in 1956 by IBM with a recording density of 2Kbit in^{-2} [1] Since then, progress has been made in the past decades to increase areal density of magnetic recording to meet the consumer demands. Figure 1.1 shows the road map of magnetic recording technology applied in HDD, as well as the areal density, reported by Seagate Technology LLC [2]. Despite the slowing down of growth rate due to the approach of physical limit, the areal density keeps increasing with an annual growth rate of 30%. Today, the areal density is approaching 1Tbit/in^2 and a total capacity up to 8TB is available in a single hard disk drive device.

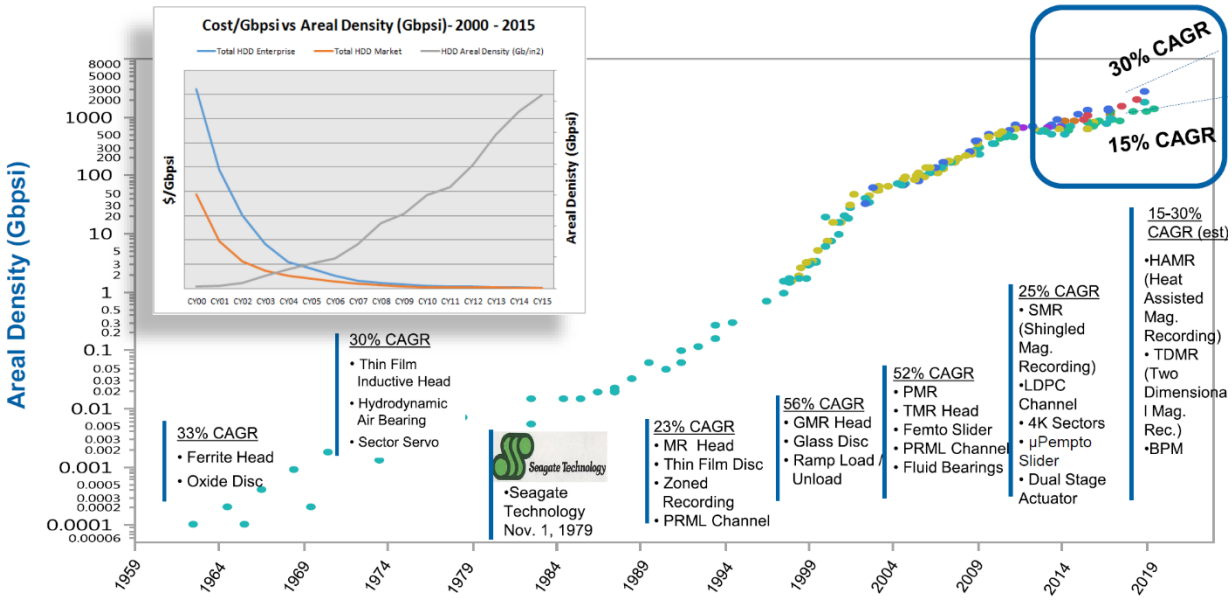

Figure 1.1 Areal density growth of magnetic hard disk drive along with the innovation of new technologies [2].

In the conventional recording media, the magnetization direction of the recording bit lies primarily in the plane (longitudinal recording) or normal to the plane (perpendicular recording) of the thin film coating [3]. The recording media are in polycrystalline state and each recording bit is composed of a group of grains, whereas the grains are randomly oriented [4]. The signal to noise ratio (SNR) depends on the number of grains in 1 bit, therefore a reduction of grain size is desired for the purpose of higher areal density [4]. However, as the grain size decreases, the large demagnetization field at the transition between adjacent opposing bits makes the magnetization unstable and change its magnetization direction under thermal fluctuation. This thermal driven random orientation of magnetization is named superparamagnetism. As a consequence, the grain size could not be unlimitedly small, resulting an upper bound of recording density. The limit was

estimated to be 100 to 200 Gbit/in^2 for longitudinal recording [5-7] and 500 Gbit/in^2 or slightly beyond for perpendicular recording [8,9].

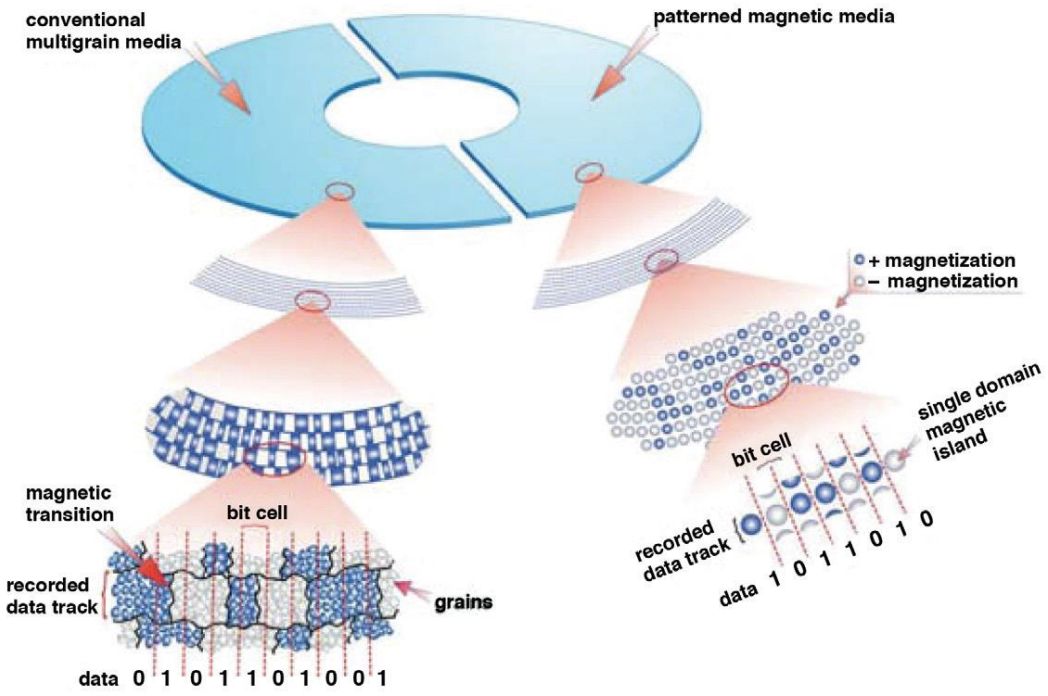

Figure 1.2 Comparison between conventional multigrain media and bit patterned media [10].

The idea of bit patterned media provides a practical way to solve the grain density problem in the traditional granular recording media. Figure 1.2 shows a schematic comparison between multigrain media and bit patterned media [10]. Contrary to the conventional continuum media, each data bit is now recorded in a single domain magnetic island in bit patterned media. The immediate advantage of such a scheme is the elimination of transition noise between oppositely magnetized grains and the larger anisotropic volume defined by the single island rather than individual grain [11]. Therefore, the single island could be scaled to a much smaller size without

reaching the superparamagnetic limit, giving a much higher recording density. The patterned media could be fabricated by lithography or self-assembly. Self-assembly of monodispersed nanoparticles with uniform particle size, shape, composition is more fascinating since it goes beyond the resolution limits of lithography patterning.

In order to validate the application of bit patterned media in magnetic recording industry, research problems need to be solved, such as orientations of nanoparticles and packing of nanoparticles. In the aspect of materials selection, high anisotropy materials are desired to overcome the superparamagnetism and to improve the thermal stability and coercivity. Among various types of hard magnetic materials, $L1_0$ ordered FePt and CoPt nanoparticle has a relatively higher uniaxial magnetocrystalline anisotropy [12]. As a result, these nanoparticles with a diameter as small as around 3 nm can sustain their magnetization at room temperature. While the size is reduced into nanometer scale, the magnetic nanoparticles behave significantly different from the bulk materials. Because of the high specific surface area, the surface effect will essentially impact on the magnetic properties. Therefore, it is of great research interest to understand how this effect would influence the magnetic properties of nanoparticles.

Computational simulations functions as a complementary to the experiments in materials science through providing theoretical explanation of the experimental observation and instructing the experimental design. The observations in experiments are always the interplay of several factors. It is usually unable to identify the principal affecting components, while in computational simulations individual factor may be controllable. Computational simulation can also provide information of materials that are hard to be measured in experiments. Moreover, recent idea of materials informatics [13] helps scientists with the search of new materials with desired properties using computational machine learning algorithm, which will significantly reduce the amount of

massive experimental trial and error. These benefits make computational simulation a valuable tool in understanding and designing materials.

In this thesis, atomistic simulations of magnetic properties for alloy nanoparticles, specifically FePt and CoPt, have been performed. How the surface effects would impact on the magnetic properties has been studied. The underlying physical mechanism of the observed surface magnetisms has been identified.

2.0 BACKGROUND

2.1 STRUCTURAL PROPERTIES OF CO-PT AND FE-PT

Among various hard magnetic materials, $L1_0$ ordered FePt and CoPt are most promising candidates that will be used in ultra-high areal density magnetic recording due to their high magnetic anisotropy. The anisotropy is measured by a constant K_u which characterizes the energy required for magnetization reversal along the easy axis. The associated energy term is usually called magnetic anisotropy energy (MAE). Table 2.1 summarizes common hard magnet alloy properties [12,14]. It can be seen from the table that the magnetic anisotropies of FePt and CoPt are highest in non-rare earth alloys and the values are comparable to those of the rare-earth alloys. This offers thermally stable grain diameters D_p down to 3.6 nm for CoPt and 2.8 nm for FePt. This high anisotropy originates not only from the basic element features of specific transition metal, such as the hybridization between Co/Fe 3d and Pt 5d orbitals, but also from the unique crystal structures these materials have.

Table 2.1 Magnetic properties and theoretical minimal grain diameters of various recording media candidates [12,14].

Alloy system	Material	K_u (10^7erg/cm^3)	M_s(emu/cm^3)	T_c(K)	D_p (nm)
Co-alloys	CoPtCr	0.20	298	-	10.4
	Co	0.45	1400	1404	8.0
	Co3Pt	2.0	1100	-	4.8
$L1_0$ phases	FePd	1.8	1100	760	5.0
	FePt	6.6-10	1140	750	3.3-2.8
	CoPt	4.9	800	840	3.6
	MnAl	1.7	560	650	5.1
Rare earth	Fe14Nd2B	4.6	1270	585	3.7
	SmCo5	11-20	910	1000	2.7-2.2

Figure 2.1 gives the equilibrium phase diagram of Co-Pt and Fe-Pt materials system [15,16]. As can be seen from Figure 2.1, stoichiometric CoPt and FePt alloy have two phases – the high termperature face-centered cubic (fcc) phase (shown in Figure 2.2 (a)) and the low temperature $L1_0$ phase (shown in Figure 2.2 (b)). In the disordered fcc structure, the Pt and the Fe/Co atoms randomly occupy the lattice sites. This randomness implies isotropy along x, y and z direction, which would lead to a soft magnetic phase (anisotropy value in the order of 10^4ergs/cm^3). On the other hand, in $L1_0$ structure, alternating layered structures of two different type of atoms are formed along the c axis in a tetragonal cell. As a consequence, this ordering induced symmetry breaking yields the high anisotropic hard magnetic phase (anisotropy value in the order of 10^7ergs/cm^3). The $L1_0$ phase is stable at the temperature less than 825℃ and 1300℃ for CoPt and FePt, respectively. Unless otherwise specified, the CoPt and FePt nanoparticles in this thesis refer to the stoichiometric CoPt and FePt or near stoichiometric particles in $L1_0$ structure.

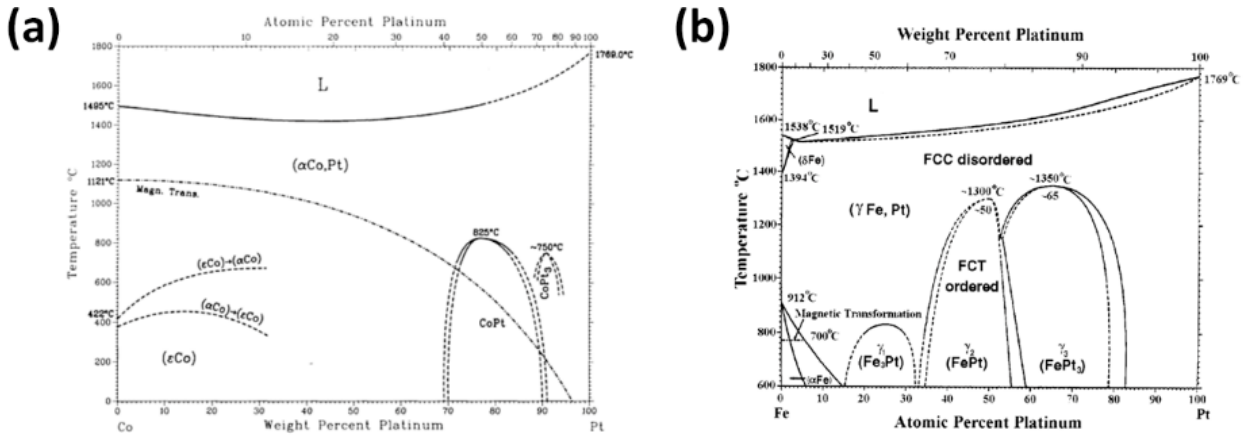

Figure 2.1 Equilibrium phase diagrams of (a) Co-Pt and (b) Fe-Pt systems [15,16].

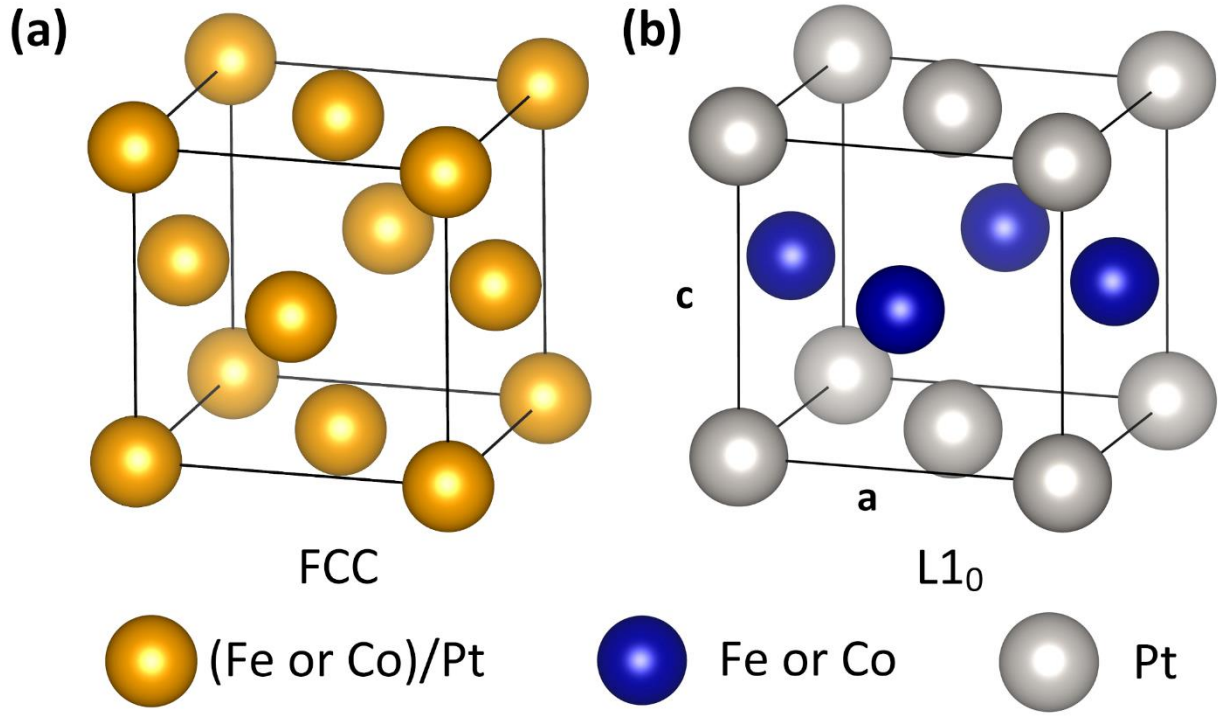

Figure 2.2 unit cell structures of (a) face centered cubic (fcc) (b) $L1_0$ lattice

The challenge in applying $L1_0$ ordered FePt and CoPt as bit patterned media is to design and assemble the magnetic nanoparticles with controlled packing density and performance. Extensive research effort has been devoted to fabricating the FePt and CoPt alloy nanoparticles, where a homogeneous distribution of size, shape and orientation is desired. By investigating the morphology of 2.4-3 nm CoPt nanoparticles under TEM, Alloyeau demonstrated that the order-disorder transition temperature (and hence the magnetic properties) is sensitive to the shape of the nanoparticles [17]. Therefore, it is inferred that the morphology is one of the dominant aspects in determining the magnetic properties of nanoparticles. Recently, Di Paola studied the geometrical effects on the magnetic properties of Pt nanoparticles using first principles calculations and found that the total magnetization strongly depends on the local atomic arrangement through partial charge transfer between surface and sub-surface atoms [18]. By means of DFT calculation, Gruner reported a variation of the magnetization for CoPt and FePt nanoparticles with different shapes [19]. However, how the local geometric factors impact on the magnetic properties (such as atomic magnetic moment and non-collinear spin structures) in these alloy systems has not been examined yet.

The thermodynamically stable morphology of ~5 nm CoPt and FePt nanoparticles has been debated. First principles calculations combined with Wulff theorem predicted a stable structure of cuboctahedral shape for both nanoparticles, which is comprised of two six (001) facets and eight (111) facets [20]. However, further theoretical study revealed that the ordered icosahedral and decahedral structure are more favorable than the $L1_0$ phase in FePt, while for CoPt the surface segregated core-shell icosahedral structure is more energetically stable [19]. The icosahedron is a multiply twinned structure which are composed of twenty twin-related tetrahedra packed along (111) faces, where the decahedron is comprised of five structural domains of nearly identical size

and the five domains (also the five twin plains) intersect at the five-fold symmetry axis in the structure. Experimentally, all the three shapes of nanoparticles were observed at different synthesis conditions, as are shown in Figure 2.3 [21-25]. For example, the CoPt nanoparticles of 1-3 nm possess an icosahedral structure if grown at room temperature. Followed by an annealing at 500℃, the nanoparticles would evolve into a decahedral shape. Meanwhile, growth at 500℃ would yield truncated octahedral (or cuboctahedral) structures [26]. Although nanoparticles in some other shapes, such as spherical and cubic [27], have been synthesized in experiment, the cuboctahedral, icosahedral and decahedral morphologies are more energetically stable and can be chosen as representatives in investigating the shape effect on the magnetic properties.

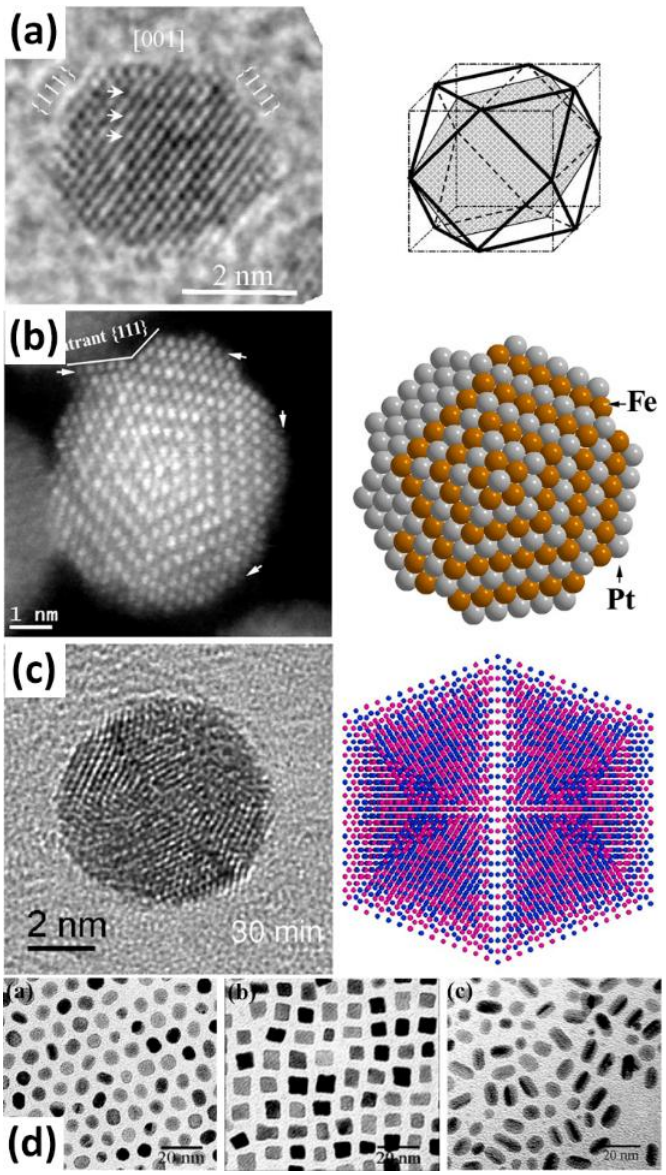

Figure 2.3 Microscopic images of FePt nanoparticles in various shapes. (a) HRTEM image of an FePt nanoparticle after annealing at 530℃ for 1 h and a schematic cubocahedron model [21]; (b) high-resolution HAADF (Z-contrast) image of a 6-nm decahedral FePt nanoparticle and a simulated atomic model [22]; (c) Dynamic HRTEM images of an icosahedral FePt nanoparticle taken under an electron beam flux of ~50 A/cm^2 at 300 kV and a simulated atomic model [24,28]; (d) TEM images of FePt nanoparticles with other shapes – spherical shape, cuboidal shape and rod shape [27].

2.2 MAGNETIC PROPERTIES OF CO-PT AND FE-PT NANOPARTICLES

As the particles size decreases into nanometer scale, the surface atoms make up a large proportion in a particle. As compared to those inside bulk crystal, the surface atoms will have less number of adjacent neighbors, reduced symmetry group, and stronger local relaxation. It is believed that these structural changes can modify the electronic structure of the surface atoms in terms of the spin up and spin down density of states, exchange coupling interaction between the surface and subsurface layers, and stabilization of magnetic phases different from that of bulk crystal field [29]. Thus, the surface of magnetic materials could possess magnetic properties (such as, magnetic moment, magnetic anisotropy, and spin canting) distinct from those of the corresponding bulk crystal. Owing to its important technological ramifications and contributions to fundamental understanding of the physics of magnetism, surface magnetism of magnetic materials has been of great interest to the researchers [29]. In this section, the surface effect on magnetic properties (basically spin and energy based properties that could be directly obtained from theoretical calculations) of Co-Pt and Fe-Pt related nanoparticles are reviewed.

Surface effects can lead to an increase in the magnetization of small metallic particles with respect to the bulk value. For instance, in elementary Co nanoparticles, an enhancement of over 25% in the magnetic moment of Co atoms has been reported by Respaud et al. This increment was proved to be more significant with decreasing particle size. The authors associated this result with the large influence of the surface atoms [30]. In another research, Osuna et al. found a strong enhancement of about 0.2 μ_B per atom in the surface magnetic moment in 1.6 nm sized Co nanoparticles [31]. Billas et al. investigated small Fe, Co and Ni clusters with size ranging from several tens to several hundreds of atoms by means of molecular beam deflection measurement.

Their results showed that the magnetic moment increased from bulk value to the atomic value as the particle size was reduced [32].

In addition, another surface-driven effect is the improvement of the magnetic anisotropy so that it could exceed the value obtained from the crystalline and shape anisotropy. Luis et al. measured the effective magnetic anisotropy constant of spherical Co clusters (0.8nm - 5.2nm) to be about 2.3×10^6 J/m^3 to 0.7×10^6 J/m^3, which is one to two orders of magnitude larger than the bulk value of 6.5×10^4 J/m^3 for fcc Co [33]. Recently, Oyarzún et al. reported an effective magnetic anisotropy constant of 2.18×10^5 J/m^3 for Co nanoparticle embedded in Cu matrices [34]. Both these two researches showed a negative correlation between the anisotropy energy and particle size. Gambardella et al. showed that the magnetic anisotropy energy is dependent on single-atom coordination changes in cobalt nanoparticles containing up to 40 atoms, which evidenced the contribution of surface anisotropy [35]. Moreover, Peng et al. estimated the magnetic anisotropy constant K to be 10^5 J/m^3 in monodispersed Fe cluster assemblies with size of 7-16 nm, which is also one order of magnitude larger than the bulk value [36]. Bødker et al. reported an increase of magnetic anisotropy constant of Fe nanoparticles with decreasing Fe particle size up to 5 times the bulk value. They attributed this finding to the influence of surface effects as well [37].

Complementary to experimental measurements, theoretical researches have been conducted to elucidate the microscopic origin of magnetic anisotropy and magnetic moment increment. In agreement to the experimental observations, computational simulation has successfully predicted this enhancement in transition metal clusters [38-40]. The enhancement of the magnetic moment at the surface follows several mechanisms [29,38,41,42]: (1) at surface, the local structural symmetry is broken, the electron orbital is localized and the quenching of orbital moment by strong crystal field is suppressed on surface atoms; (2) the electronic band is narrower

at surface, resulting in an increase in the spin magnetic moment; (3) the interatomic distance change induced by surface relaxation would lead to the imbalance of spin up and spin down electron density of states (DOS); (4) the large DOS at fermi level gives rise to a larger orbital magnetic moment at surface.

On the other hand, in some cases (in particular, metal alloys), it was observed that the properties of magnetic metal nanoparticles could become worse than those of bulk metals. The magnetic anisotropy energy of CoPt nanoparticles was measured to be about 3.85×10^5 J/m^3 [43,44], and 1.7×10^6 J/m^3 [45], all of which were much smaller than the value (4.9×10^6 J/m^3) of bulk $L1_0$ CoPt crystal [46]. This reduction in magnetic properties showed direct correlation with the reduced size of $L1_0$ CoPt nanoparticles. Tzitzios et al. reported a positive variation of coercivity (a parameter also measuring the anisotropy) with an increasing CoPt nanoparticle size [47]. Same scenario was also found in FePt nanoparticles. In Rellinghaus et al.'s work, the anisotropy constant measured fell into the range of 1.7×10^5 J/m^3 to 7.7×10^5 J/m^3 [48]. Sun et al. [49] and Okamoto et al [50] synthesized highly ordered $L1_0$ nanoparticle assemblies and extracted the anisotropy constant to be 5.9×10^6 J/m^3 and 6.2×10^6 J/m^3, respectively. All these values are to some extent below the bulk value of $6.6\text{-}10\times10^6$ J/m^3 [12]. Moreover, the magnetic moment of 3d element in CoPt [51,52] and FePt [53] nanoparticles was also measured in some experimental research to be smaller than the corresponding bulk value. It was revealed that the saturation magnetization of both $CoPt_3$ [54] and FePt [55] magnetic nanoparticles exhibited clear reduction with a decrease in particle size, as is indicated by the hysteresis loop of nanoparticles in Figure 2.4. All these researches implied that some surface effect has negative impact on the magnetic properties of alloy nanoparticles.

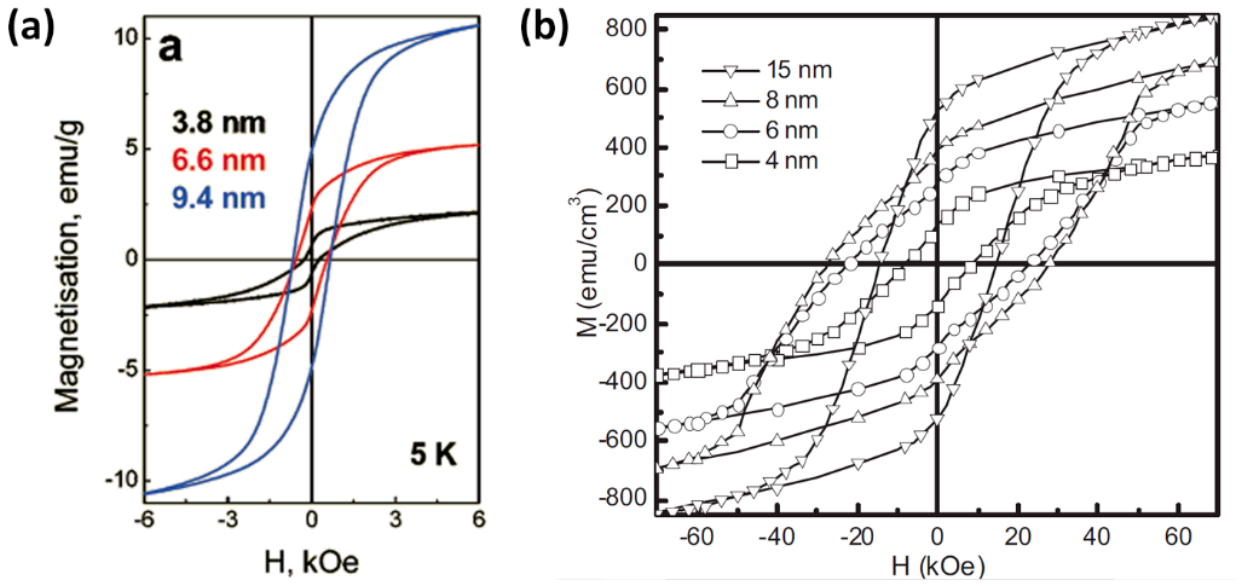

Figure 2.4 Magnetization vs applied field hysteresis loop measured for (a) FePt and (b) $CoPt_3$ nanoparticles with different size.

In addition, theoretical predictions on CoPt and FePt to some extent disagree with the experimental observations above. Pustogowa et al. investigated the magnetic properties of CoPt thin film superstructures on Pt (100) and Pt (111) using DFT calculation. Their results showed that an enhancement in magnetic moments was found on surface Co atoms [56]. Similar results were also reported in a much recent study on pure FePt and CoPt slab surfaces by Dannenberg et al. using first principles calculations. In their work, a magnetic moment enhancement of about $0.07\mu_B$ was found for the subsurface Co atoms on Pt-terminated (001) and (110) surfaces with respect to a Co atom in the bulk CoPt crystal. The magnetic moment of surface Pt atoms in CoPt was found higher than the bulk value for the (110) surface, whereas lower than the bulk value for the (001) surface Similarly, they predicted an enhancement of $0.08\mu_B$ for surface or subsurface Fe atoms on (001) and (111) surfaces but the magnetic moment of surface Pt atoms was found higher than the

bulk value for the (001) surface and lower for (111) surface [20]. In spite of small decrease in magnetic moment of surface Pt atoms, the overall magnetization of CoPt/FePt slabs is still increased. These discrepancies between experimental and theoretical results raise the research interest in understanding the surface effects in alloy nanoparticles.

Various mechanisms have been suggested to contribute to the observed magnetic property deterioration of these magnetic nanoparticles. For example, the chemisorption of large molecules could introduce additional interactions on surface spins [57]. Also, the demagnetization field originate from the interactions between particles would lead to rotation of spins [43]. Intrinsically, the surface spins might not align parallel to the bulk magnetization direction due to the broken symmetry at surface [58]. However, these effects would as well occur in elementary metallic nanoparticles such as Co and Fe. Some aspect is missing particularly in alloys. There must be at least one type of surface effect that the elementary metallic nanoparticles do not possess and only occurs in alloy nanoparticles.

Quantitative experimental study on FePt nanoparticles suggested that the reducing long-range chemical ordering correlated well with the variation in the magnetic properties with a reduction in nanoparticle dimension [55,59]. In a very recent research, Yang et al. reproduced the 3D reconstruction of a partially $L1_0$ ordered FePt nanoparticle through scanning transmission electron microscopy. Using the atomic coordinate as an input to DFT, they predicted that the distribution of local MAE matches with the $L1_0$ order parameter difference [60]. Among various surface effects, surface segregation is believed to be an important material process affecting the chemical ordering in alloy nanoparticles [61-66]. Therefore, we propose that the surface segregation effect would be one of the reason dominating the magnetic properties in alloy nanoparticles.

The intrinsic surface effects (such as surface spin canting and surface segregation) are hardly measured in experiment because of the difficulty to find a control group that does not possess those effects. But in computational simulation, these conditions could be well controlled. In this work, we have applied computational method to investigate these intrinsic surface effects on the magnetic properties in alloy nanoparticles.

2.3 SURFACE SEGREGATION

Surface segregation refers to the phenomena that one particular element in a multi-component alloy prefers to migrate to the surface atomic layer [67,68]. Consequently, the composition of that element in the top few atomic layers at surface could deviate significantly from bulk materials. Figure 2.5 is a schematic diagram of this phenomena. The red and grey balls in Figure 2.5 correspond to two composing elements in a binary alloy. The top two atomic layers represents the surface layers exposed to gas or vacuum, while the bottom five atomic layers represents bulk region. The grey atoms prefer to segregate to the surface layer resulting an atomic ratio in the surface region different from that in the bulk. The change in surface composition controls various properties in alloys that depends on surface processes such as surface diffusion in crystal growth, heterogeneous catalytic reaction, oxidization corrosion reaction and the nucleation of dislocation [69-74]. Therefore, it becomes important to fully understand the surface segregation in alloys, particularly nanostructured alloys with enormous specific surface area.

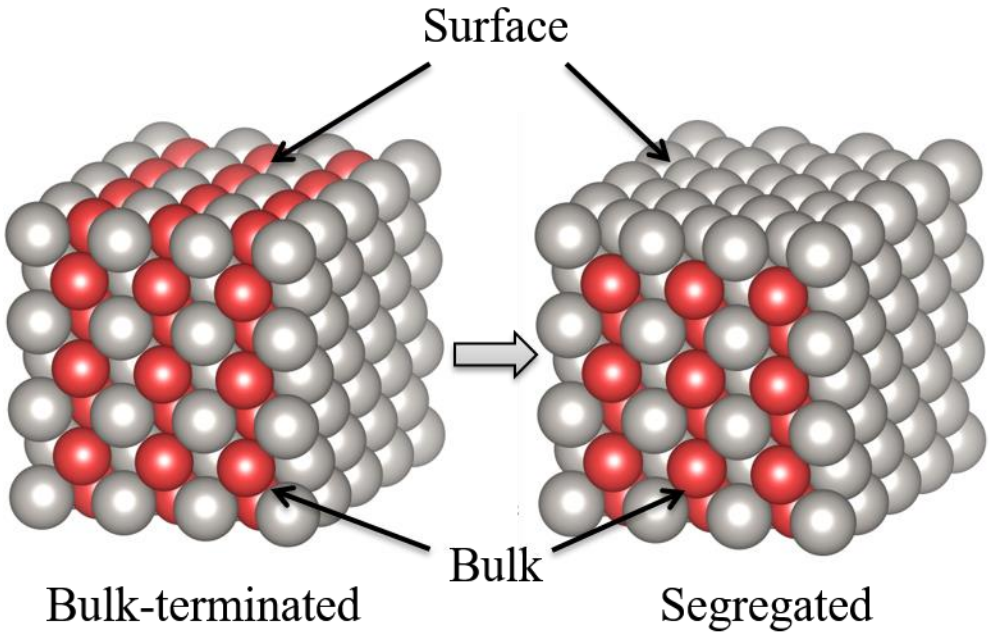

Figure 2.5 Schematic diagram of the surface segregation in a binary alloy. The red and grey balls correspond to the two composing elements.

Thermodynamically, surface segregation is driven by the need to minimize the total free energy. If the total free energy is reduced when one component of alloy migrates to the surface, then the surface segregated structure is more energetically stable than the mixed alloy structure (order or disorder). It has been known that the surface segregation process in alloy systems is mainly governed by the three following mechanisms: [75,76] (1) the majority component of the alloy will segregate to the surface when the heat of the solution is negative in order to maximize the mixing of the two components in bulk; (2) the larger component in a smaller-component-rich alloy (and vice versa) will segregate to the surface to release the strain energy when the atomic mismatch is enormous; and (3) the component with the lowest surface energy will segregate to the alloy surface to reduce the total surface energy. Furthermore, surface composition is also

determined by atom chemisorption and impurities doping on surface [66,77-80]. Adsorbed species such as oxygen atom may have stronger bonding with one component than the others so that those atoms will be attracted to move to the surface. Doping impurities might introduce additional bonding between elements. The mixing composition profile would therefore be affected because of the preference of attraction or repulsion with the impurity elements.

Consequently, surface segregation is a result of the complicated interaction between composing elements and environmental factors. All these effects (heat of solution, surface strain and surface energy, chemical adsorption and doping impurities) can be reliably reproduced in first principles calculations.

Surface segregation was theoretically predicted [81-83] and experimentally confirmed [22,25,28,84,85] on FePt/CoPt slabs and nanoparticles. For example, the complicate interplaying of chemical ordering and surface segregation effects in $Co_{1-c}Pt_c$ (Pt concentration varies from 0 to 1) nanoparticles have recently been studied in detail by Lopes et al. using the Monte Carlo simulations within a tight-binding Ising model [81]. Chepulskii et al. calculated the cluster expansion coefficient from first principles simulation. By coupling the cluster expansion with Monte Carlo algorithm, they predicted a 'core/Co/Pt' sandwich structure in $L1_0$ ordered CoPt nanoparticles [82]. Experimentally, Farle et al. observed preferential Pt surface segregation in both the icosahedral and decahedral shaped $L1_0$ ordered FePt nanoparticles with size of 5-6 nm using dynamic high-resolution transmission electron microscopy (HRTEM) [22,24,28]. Pt surface segregation has also been observed by Wang et al. in annealed $L1_2$ ordered $CoPt_3$ nanoparticles [85]. It should be noted that, in a recent HRTEM study on multi-$L1_0$ domain CoPt nanoparticles, no sign of Pt surface segregation was observed [86]. This implies that some kinetic factors might

also play roles in suppressing the Pt surface segregation in those synthesized $L1_0$ ordered CoPt nanoparticles.

Although surface segregation mostly takes place at the regions near particle surface, it indeed causes appreciable changes to the magnetic properties of alloy nanoparticles. Bohra et al. confirmed the occurrence of Cr surface segregation in Ni-rich NiCr alloy nanoparticles using aberration-corrected environmental transmission electron microscopy and further showed that this Cr segregation was responsible for the significant reduction in the measured magnetic coercivity and effective magnetic coupling strength of the annealed NiCr nanoparticles [87]. More relevant to current research project, W Grange et al. suggests that Pt segregation to the surface was responsible for the orbital magnetic moment reduction on surface Pt atoms while maintaining magnetocrystalline anisotropy, through x-ray magnetic circular dichroism (XMCD) measurements on CoPt thin films [88,89].

Except for the experiments mentioned above, the influence of surface segregation on magnetic properties has been rarely explored. This is because of the difficulty in direct experimental measurement of samples with and without segregation. This knowledge gap needs to be filled with the help of computational simulation method.

2.4 SURFACE ANISOTROPY

In magnetic nanoparticles, the spin direction on surface atoms would deviate from the external magnetic field as well as the corresponding bulk magnetization axis. This phenomenon is called surface spin canting. It occurs when the easy axis associated with the surface anisotropy is different from the bulk easy axis [90]. If the surface anisotropy is locally in-plane, the surface spins tilt

towards a direction parallel to the surface, whereas they tilt towards a direction perpendicular to the surface when the surface anisotropy is locally out-of-plane. Physically, this surface anisotropy originates from the interaction of electrons subject to spin-orbit coupling (SOC) at the surface magnetic atoms where the inversion symmetry is broken. Néel proposed a pair interaction model to explain the existence of surface anisotropy in which the symmetry breaking is captured by the reduced coordination number at surface atoms [91]. In his original work, the interatomic pair interaction energy is given by

$$H = -\sum_{i,j} K_{S_{ij}} \left(\overrightarrow{S_i} \cdot \overrightarrow{e_{ij}}\right)^2 \tag{2.1}$$

where $\overrightarrow{S_i}$ is the unit spin vector, $\overrightarrow{e_{ij}}$ is the unit vector connecting neighboring atoms and K_S is the Néel's constant describing the interaction strength. The summation is over all nearest neighbors of all atoms in the nanoparticle or thin film, however it ends up being a constant energy (in cubic materials) for an atom in bulk. Therefore, only atoms on surface contribute to the surface anisotropy energy that depends on the local magnetization direction.

Though Néel's model is phenomenological, it already contains part of the influence of band structures, as was demonstrated by Skomski using the tight-binding moments theorem [92,93]. Meanwhile, the predictions in Néel's model have been found in good agreement with experiments on nanoparticles and thin films [94-96]. For example, the giant magnetic coercivity in cubic granular $FeCo/SiO_2$ and $NiCo/SiO_2$ thin films as a function of Co concentration is successfully explained by the existence of surface anisotropy. Chen found that the effective anisotropy constant is in accordance with the value extracted from Néel's model [95].

The magnitude of Néel's constant depends on the interacting element and the interatomic distance r_{ij}.

$$K_{S_{ij}} = K_{S_{ij}}\left(r_{ij}\right) \tag{2.2}$$

Under 1st order expansion with respect to the bond strain η

$$K_{S_{ij}} = K_{S_{ij}}(r_{ij}^0) + \left(\frac{dK_{S_{ij}}}{dr}\right)_{r_{ij}^0} r_{ij}^0 \eta, \eta = \frac{r_{ij}}{r_{ij}^0} - 1 \tag{2.3}$$

where r_{ij}^0 is the equilibrium bond length in a bulk unit cell. $K_{S_{ij}}(r_{ij}^0)$ and $\left(\frac{dK_{S_{ij}}}{dr}\right)_{r_{ij}^0}$ are two independent parameters that are related to the magnetostriction properties of materials. In an fcc system, by equating the Néel's energy with the magnetoelastic energy, Néel's constant and its first order derivative are given by [96]

$$K_{S_{ij}}(r_{ij}^0) = \frac{1}{2} b_1 - \frac{1}{4} b_2$$

$$\left(\frac{dK_{S_{ij}}}{dr}\right)_{r_{ij}^0} = -b_1 + \frac{3}{2} b_2 \tag{2.4}$$

where b_1 and b_2 are magnetoelastic coupling constants, which can be determined by DFT calculations. In $L1_0$ system, the breaking symmetry brings additional degree of freedom, both in magnetoelastic coupling energy and Néel's anisotropy energy. The relations between these parameters should be reevaluated.

Within this formulism, the surface anisotropy of each surface atoms could be calculated by adding up all the pair interaction connecting the atom. Therefore, the surface anisotropy in a nanoparticle could be characterized by a simple parameter K_S. Though Néel's model does not provide more physical insights on the origin of surface anisotropy, it provides a bridge from first principles to micro scale as well as a bridge from atomistic simulation to experimental observation.

3.0 HYPOTHESIS AND RESEARCH OBJECTIVES

The main purpose of this thesis is to investigate in detail how the surface effects would influence the magnetic properties of CoPt and FePt nanoparticles. To this end, the following hypothesis are proposed:

1. Surface segregation would break the local $L1_0$ ordering at surface and therefore the magnetic properties of CoPt and FePt nanoparticles would be depressed.

2. The change in nanoparticle shapes would give rise to the variation in magnetic properties, owing to the change in coordination number, structural relaxation, chemical bonding etc. The site resolved magnetic moment would depend upon the local environment.

3. The surface magnetism of nanoparticle is the result of the collective effect of composing crystallographic surface.

4. The magnetic anisotropy energy originates from the relativistic spin-orbit coupling effect. Therefore, the change of MAE would be reflected in the electronic structures.

5. Surface spin canting is governed by the Néel's surface anisotropy, while the Néel's surface anisotropy could be correlated with magnetostriction. The surface spin canting fashion could be explained by the magnetoelastic properties of bulk materials

6. Doping with impurity elements would modify the surface segregation profile because of the introduction of additional bonding. Through this approach, the local atomic arrangement would be controlled.

To test the hypotheses, the following objectives are accomplished:

1. Predict the magnetic and energetic properties of bulk-terminated and surface-segregated alloy nanoparticles.

2. Investigate the magnetism of alloy nanoparticles in three different shapes, namely cuboctahedra, decahedra, and icosahedra. Evaluate the local structural and chemical factors to identify the underlying physics.

3. Investigate the magnetism of low-index crystallographic surfaces. Establish a correlation between the predicted magnetic properties with the electronic structures.

4. Calculate the magnetoelastic response and the Néel's anisotropy constant of bulk alloys. Explain the predicted spin structures in nanoparticles.

5. Test the surface composition profile of low-index crystallographic surfaces doped with different elements.

4.0 ATOMISTIC SIMULATION ON MAGNETIC PROPERTIES OF ALLOYS

4.1 DENSITY FUNCTIONAL THEORY IN MAGNETISM

The ground state properties of a materials are governed by the fundamental interactions between electron-electron, electron-core and core-core in a many-atom system. Quantum mechanically, these interactions could be described by the many-body Schrödinger equation, which could be solved theoretically with very few experimental inputs. Therefore, these kinds of atomistic simulation of materials properties is usually referred as *ab initio* or first principles calculation in solid state physics. Among multiple approaches in dealing with the many-body Schrödinger equation, density functional theory (DFT) has developed into one of the most successful methods since its first establish, owing to the relatively high computational accuracy achieved when consume reasonable computational resources. In simulating the magnetic properties, DFT could serve to be a valuable tool not only to directly determine the magnetic moment on each atom, the magnetic anisotropy energy and magnetic order of materials, but also to provide basic physical quantities, such as exchange coupling constant and magnetoelastic constant, that can be used in other theoretical approaches.

The central theorem of DFT was proposed by Hohenberg and Kohn in 1964: [97] (1) the many body wavefunction Ψ and external potential v caused by nuclei are uniquely determined by the electron density, which is to say, the total energy is uniquely determined by the electron density;

(2) for a given external potential, the ground state density minimizes the total energy functional $E[n]$. This theorem is valid in any system of electrons moving in an external potential in a nondegenerate ground state. The DFT total energy functional $E[n]$ has the form

$$E[n] = T[n] + E^H[n] + E^{xc}[n] + \int v(r)n(r)d^3r \tag{4.1}$$

where $T[n]$ is kinetic energy for the non-interacting electrons, $E^H[n]$ is the electron-electron repulsion energy (Hartree energy) and $E^{xc}[n]$ is sum of the exchange energy which is caused by the Pauli exclusion principle and correlation energy between the electron-electron interaction with respect to the non-interaction electrons. According to theorem (2), the ground state energy can be formulated variationally with respect to the electron density. This gives the famous Kohn-Sham Equation: [98]

$$\left\{-\frac{\hbar^2}{2m}\nabla^2 + v(r) + e^2\int\frac{n(r')}{|r-r'|}dr' + \frac{\delta E^{xc}[n]}{\delta n(r)}\right\}\phi_i(r) = \varepsilon_i\phi_i(r) \tag{4.2}$$

where $\hbar$ is the Planck's constant, m is the mass of electron, e is the charge of electron and ε_i, ϕ_i are the effective single electron energy and wave function, respectively. This equation is much more tractable than the full many body Schrödinger equation because it depends on only one single spatial coordinate r rather than the spatial coordinate of all the electrons r_i. This distinguished series of work wins Kohn half share of the Nobel Prize in Chemistry in 1998.

The Kohn-Sham Equation looks deceptively clear and simple, however, to find an accurate solution to the equation is still troublesome. One of the main difficulties comes from the exchange correlation term $E^{xc}[n]$. Though DFT has proved its existence, its exact form is unknown. Several levels of approximation were made to evaluate the exchange potential $v^{xc} = \frac{\delta E^{xc}[n]}{\delta n(r)}$. The first level is Local Density Approximation (LDA) [98,99], which assumes the inhomogeneous electron density behaves locally like a homogeneous electron gas on average. Therefore, the exchange-correlation functional is a functional of electron density only:

$$E_{LDA}^{xc}[n] = -\frac{3}{4}\left(\frac{3}{\pi}\right)^{1/3} \int n\left(r^{4/3}\right)dr \tag{4.3}$$

Despite the simple idea adopted from homogeneous electron gas, LDA works reasonably well in predicting the lattice parameters in elemental ferromagnets. However, LDA fails in some cases. For example, it predicts that both the non-magnetic and anti-ferromagnetic fcc Fe have lower energy than the ferromagnetic bcc phase, which is contradictory to the experimental observation [100]. To fix this problem as well as to achieve more accurate E^{xc}, higher order approximation in the exchange-correlation functional could be made by including the local gradient in the density, which is usually referred to the Generalized Gradient Approximation (GGA). Several formulism of GGA has been put forward, including Perdew-Wang 91 (PW91) [101], Perdew-Burke-Ernzerhof (PBE) [102], Perdew-Burke-Ernzerhof revised for solids (PBEsol) [103], Armiento-Mattsson 05 (AM05) [104] etc., among which PW91 and PBE are most commonly used. Modern development also includes addition terms such as 2nd order derivative of electron density (meta-GGA) [105], Hartree-Fock exchange functional (HSE03) [106] in the exchange-correlation term. However, these methods require much more extensive computation cost. In this work, the calculations are restricted in GGA approximation.

In a magnetic system, we are interested not only in the electron density $n(r)$ but also in the spin magnetization density $m(r)$. From quantum mechanics, we know the spin angular moment operator of electron is usually written in terms of Pauli spin operator, which is represented by 2×2 matrices. The spin-polarized version of the density functional theory (or spin-density-functional theory) can be formulated by replacing scalar densities and potentials with 2×2 spin density matrices and potential matrix [107]. If the density matrix could be diagonalized, the magnetic moments on all atoms in a unit cell are aligned along the same quantization axis and the magnetism is called collinear. The total electron density $n(r)$ can therefore be decoupled into the spin-up

$n^{\uparrow}(r)$and spin-down $n^{\downarrow}(r)$ contributions. The spin magnetic moment μ_S for a collinear system is then the consequence of imbalance of electrons in the spin-up and spin-down channel and could be simply expressed as (in units of μ_B, Bohr magneton)

$$\mu_S = \int (n^{\uparrow}(r) - n^{\downarrow}(r)) dr \tag{4.4}$$

Within an atom, the total magnetic moment is a sum of spin and orbital contributions, $\mu_J = \mu_S + \mu_L$. The orbital moment results mainly from the spin-orbit coupling term, which describes the interaction between the spin of electrons and its motion. A traveling electron near a nucleus experiences an electric field. This electric field translates relativistic into an effective magnetic field, which interact with the electron spin moment. Consequently, the spin angular momentum aligns of an electron preferentially parallel to its orbital angular momentum. The spin-orbit coupling contribution to the Hamiltonian near a nucleus could be expressed as

$$H_{SO} = \frac{1}{r}\frac{dv(r)}{dr}(\sigma \cdot L) \tag{4.5}$$

where $v(r)$ is the radial potential, σ is the Pauli spin matrix and L is the orbital angular momentum operator. This term will break the decoupling of spin-up and spin-down electrons, leading to noncollinear magnetism. Moreover, in this formulism, the total energy of materials depends on the magnetic moment directions on each atom. The total energy difference when the solid is magnetized in two different directions is known to be the magnetic anisotropy energy (MAE). MAE is usually small for high symmetric materials systems, for example, bcc Fe or fcc Ni [108], and is larger for materials with a unique crystallographic axis, such as hcp Co [109], $L1_0$ CoPt and FePt [14]. In low dimensional systems, the breaking of structural symmetry will give rise to additional MAE, which indeed is the surface anisotropy discussed in previous chapter.

To conclude, the MAE and magnetic moments are well determined in DFT and DFT is capable in simulating basic magnetic properties of nanoparticles. In this regime, the accurate

ground state properties can be extracted ab-initio from the ground state energy and wave function, without any empirical input.

In this work, the first principles DFT calculations have been performed via a plane-wave basis formulation and Projector Augmented-Wave (PAW) method as implemented in the Vienna Ab-initio Simulation Package (VASP) [110,111]. The generalized gradient approximation in the form of Perdew-Wang-91 (GGA-PW91) functional [101] was used for exchange correlation energy evaluation. The kinetic energy cutoff of 500 eV was set for plane wave expansion. In our calculations, all the structures were fully relaxed until the Hellmann-Feynman force acting on each atom was less than 0.01 eV/Å and the total energy was converged within 10^{-6} eV at every ionic relaxation step. In order to optimize the magnetic configurations of magnetic nanostructures, the spin-orbit coupling and noncollinear magnetization were used [112].

4.2 MAGNETOELASTIC THEORY

Magnetoelastic coupling describes the interaction between magnetic polarization and the lattice deformation, from which two phenomenological effects can be derived – the mechanical strain induced by applied magnetic field (magnetostriction) and the magnetic susceptibility response under stress (Villari effect). Mathematically, the magnetoelastic energy density f_{me} relative to the equilibrium reference state can be expressed as a function of applied strain and the magnetization direction [113]. For tetragonal lattice, under 1st order expansion with respect to small strain,

$$f_{me} = b_{11}(\varepsilon_{xx} + \varepsilon_{yy}) + b_{12}\varepsilon_{zz} + b_{21}\left(\alpha_z^2 - \frac{1}{3}\right)(\varepsilon_{xx} + \varepsilon_{yy}) + b_{22}\left(\alpha_z^2 - \frac{1}{3}\right)\varepsilon_{zz}$$
$$+1/2b_3(\alpha_x^2 - \alpha_y^2)(\varepsilon_{xx} - \varepsilon_{yy}) + b_3'\alpha_x\alpha_y\varepsilon_{xy} + b_4(\alpha_y\alpha_z\varepsilon_{yz} + \alpha_z\alpha_x\varepsilon_{zx}) \qquad (4.6)$$

where b is the magnetoelastic coupling constant and ε is the elastic strain component and α is the magnetization direction cosine. The first two terms in the equation above describes pure volumetric contribution that does not depend on the magnetization direction. The rest five terms describe the anisotropic dependence of total energy under strain, which are of most concern in current research. The associated magnetoelastic constants b_{21}, b_{22}, b_3, b_3' and b_4 could be extracted from the linear regression of MAE with respect to small strains by deforming the unit cell in four different ways.

(1) epitaxial strains $\varepsilon_{xx} = \varepsilon_{yy}$

The lattice constant is constrained on *x*-*y* plane (in-plane) according to the applied strain and is relaxed along *z* (out-of-plane) direction. The ratio of the relaxed normal strain ε_{zz} to the fixed normal strain ε_{xx} is evaluated as the two-dimensional Poisson ratio, $\nu_{2D} = -\varepsilon_{zz}/\varepsilon_{xx}$. Substituting ε_{xx} and ε_{zz} into equation 4.6, then the energy difference between in-plane [100] and out-of-plane [001] magnetization orientations is

$$(E_{001} - E_{100})/V = (2b_{21} - \nu_{2D} b_{22})\varepsilon_{xx} \tag{4.7}$$

which is a linear equation in terms of b_{21} and b_{22}.

(2) epitaxial strains $\varepsilon_{yy} = \varepsilon_{zz}$

The lattice constant is constrained on *y*-*z* plane (in-plane) according to the applied strain and is relaxed along *x* (out-of-plane) direction. The ratio of the relaxed normal strain ε_{xx} to the fixed normal strain ε_{zz} is evaluated as the two-dimensional Poisson ratio, $\nu_{2D} = -\varepsilon_{xx}/\varepsilon_{zz}$. Substituting ε_{xx} and ε_{zz} into equation 4.6, then the energy difference between in-plane [010] and out-of-plane [100] magnetization orientations is

$$(E_{100} - E_{010})/V = -b_3(\nu_{2D} + 1)\varepsilon_{zz} \tag{4.8}$$

which is a linear equation in terms of b_3. Meanwhile, the energy difference between in-plane [010] and in-plane [001] magnetization orientations is

$$(E_{010} - E_{001})/V = (1/2\mathrm{b}_3(\nu_{2D} + 1) - (b_{21} + b_{22} - \nu_{2D} b_{21}))\varepsilon_{zz} \quad (4.9)$$

which is a linear equation in terms of b_3, b_{21} and b_{22}.

(3) Volume-conserving shear strain ε_{xy}

The lattice constant and angles between unit cell vector are constrained on *x*-*y* plane (in-plane) according to the applied strain. The out-of-plane strain ε_{zz} is computed according to ε_{xy} so that the total volume of the unit cell does not change.

$$\varepsilon_{zz} = \varepsilon_{xy}^2/(1 - \varepsilon_{xy}^2) \quad (4.10)$$

Substituting ε_{xy} and ε_{zz} into equation 4.6, then the energy difference between in-plane [110] and in-plane [010] magnetization orientations is

$$(E_{110} - E_{010})/V = 2b_3' \, \varepsilon_{xy} \quad (4.11)$$

which is a linear equation in terms of b_3'.

(4) Volume-conserving shear strain ε_{yz}

The lattice constant and angles between unit cell vector are constrained on *y*-*z* plane (in-plane) according to the applied strain. The out-of-plane strain ε_{xx} is computed according to ε_{yz} so that the total volume of the unit cell does not change.

$$\varepsilon_{xx} = \varepsilon_{yz}^2/(1 - \varepsilon_{yz}^2) \quad (4.12)$$

Substituting ε_{yz} and ε_{xx} into equation 4.6, then the energy difference between in-plane [110] and in-plane [010] magnetization orientations is

$$(E_{01\bar{1}} - E_{011})/V = b_4 \, \varepsilon_{yz} \quad (4.13)$$

which is a linear equation in terms of b_4.

The magnetic anisotropy energy of the mechanically strained material could be calculated using DFT simulation. Solving the system of linear equations above, we could get full description of anisotropic magnetoelastic coupling in $L1_0$ CoPt and FePt.

4.3 MICROMAGNETIC SIMULATION

When the Hamiltonian of a system is known, the equilibrium thermodynamic properties can be calculated using Monte Carlo (MC) method. The main idea of MC is to sample all the possible states with certain probability distribution. Then the stochastic thermodynamic property is then evaluated by the ensemble average of corresponding physical quantity. In Metropolis Algorithm [114], the states are sampled in a sequence of events (Markov Chain), in which a new state is proposed with an acceptance probability solely depending on the old state. If the materials system follows Boltzmann distribution, the acceptance probability of the new state is given by

$$P = \min(1, a \cdot \exp(-\beta \Delta H)) \tag{4.14}$$

where a is a pre-exponential factor depending upon the proposal distribution, $\beta = 1/k_B T$, k_B is the Boltzmann constant, T is the temperature and ΔH is the energy difference between old state and new state.

If the Hamiltonian is described by classical model, instead of by solving the many body Schrödinger equation, the thermodynamic properties of much larger material systems up to millions of atoms are accessible in MC simulations [115]. MC based micromagnetic simulations have already been employed to simulate the magnetic properties of isolated nanoparticle [116,117] and nanoparticle ensembles [118,119]. Specifically, surface effect in nanoparticles has attracted extensive research interest [120-128]. By simulating spherical nanoparticles with simple cubic

lattice, it is showed that the competition between surface and bulk magnetocrystalline anisotropy imposes a canted spin structure at the surface while the core spins remain parallel to each other [121,128]. Through MC simulation, Salazar-Alvarez et al. explained their experimental observation that the spherical nanoparticles exhibiting larger blocking temperature T_B (a parameter that characterize the transition to superparamagnetic state) than cubic nanoparticles. These effects were attributed to the different random surface anisotropy of the two morphologies [125].

In these simulations, the Hamiltonian is expressed as

$$H = -J \sum \overrightarrow{S_i} \overrightarrow{S_j} + H_{ani} \tag{4.15}$$

where J is the exchange constant and $\overrightarrow{S_i}$ is the spin moment at site i. The first term is the isotropic ferromagnetic Heisenberg exchange interaction between nearest neighbor spins while the second term accounts for a variety of anisotropy energies. For example, the term $H_u = -K_u \sum S_{iz}^2$, $H_S = -K_S \sum \left(\overrightarrow{S_i} \cdot \overrightarrow{e_{ij}}\right)^2$ describe the uniaxial anisotropy and Néel surface anisotropy [91], respectively, where K_u, K_S are anisotropy constant and $\overrightarrow{e_{ij}}$ is a unit vector pointing from site i to site j. In this work, the same formulism has been used to simulate the surface effect of alloy nanoparticles. The equilibrium state of magnetic configurations has been calculated using the recently developed Constrained Monte Carlo (CMC) method [129], which conserves the total magnetization direction of the nanoparticles. In each CMC step, a random rotation of random spin i direction is firstly proposed. Subsequently, another random spin j is picked and rotate accordingly so as to maintain the total magnetization direction. The acceptance probability is given by

$$P = \min(1, \frac{M'_z}{M_z} \frac{S_{jz}}{S'_{jz}} \exp(-\beta \Delta H)) \tag{4.16}$$

where M_z and S_{iz} are the total magnetization and local spin on site i along the magnetization direction z, the prime sign denotes the spin states after rotation.

5.0 RESULTS AND DISCUSSION

5.1 SURFACE SEGREGATION EFFECT ON THE MAGNETIC PROPERTIES OF COPT NANOPARTICLES

Previous research in our group predicted that segregation would contribute to the deterioration of magnetic properties in FePt nanoparticles [130]. Advancing the prior work, the surface segregation effect in CoPt nanoparticles is studied.

5.1.1 Magnetic Properties of Bulk-terminated CoPt Nanoparticles

In this work, we studied the magnetic properties of two bulk-terminated CoPt nanoparticles, one with a cuboidal shape (Figure 5.1(a)) and the other one with a cuboctahedral shape (Figure 5.1(b)), using noncollinear spin-polarized DFT calculations. Both nanoparticles were constructed based on the $L1_0$ ordered lattice structure of CoPt crystal, consist of 38 atoms in total, and have diameters of about 1 nm. Previous theoretical study predicted that the cuboctahedron (whose external surfaces are mostly (111) facets) was a lowest-energy structure of the CoPt nanoparticles containing 13, 19 or 55 atoms [131], motivating us to perform computation on the cuboctahedral shaped CoPt nanoparticle in this work. However, some other low-index surfaces (such as (100), (010), and (001)) could also appear frequently in actual Co-Pt alloy nanoparticles, as evidenced in a recent study on ordered $CoPt_3$ nanoparticles [132]. Consequently, we carried out computational

study in this work on a hypothetical cuboidal shaped CoPt nanoparticle (whose external surfaces are (100), (010), and (001) facets) in order to examine the influence of external facets on the magnetic properties of the CoPt nanoparticles.

In the cuboidal CoPt nanoparticle, there are 26 Co atoms in the top and bottom (001) layers and 12 Pt atoms lying in a (001) layer between the two Co layers. As a result, all the Co atoms and eight Pt atoms reside on the particle surface whereas four Pt atoms lie in the core of the particle. In the bulk-terminated cuboctahedral CoPt nanoparticle, there are three Pt (001) layers which are the top, middle, and bottom of the nanoparticle and two Co (001) layers lying in between the three Pt layers. Hence, there are in total 18 Co atoms and 20 Pt atoms in the particle. Among these atoms, four Pt atoms and two Co atoms reside in the core of this cuboctahedral CoPt nanoparticle. Consequently, as compared to the stoichiometric composition (Co:Pt=1:1) of $L1_0$ CoPt crystal, our modelled cuboidal $Co_{26}Pt_{12}$ nanoparticle has a higher content of Co with an overall composition of (Co:Pt=2.17:1) whereas our modelled cuboctahedral $Co_{18}Pt_{20}$ nanoparticle has a slightly lower content of Co with an overall composition of (Co:Pt=0.9:1). Moreover, the cuboidal nanoparticle is enclosed by rectangular (100) and (010) surfaces as well as square (001) surfaces. In comparison, the cuboctahedral nanoparticle contains mainly hexagonal (111) external surfaces in addition to square (100), (010), and (001) surfaces.

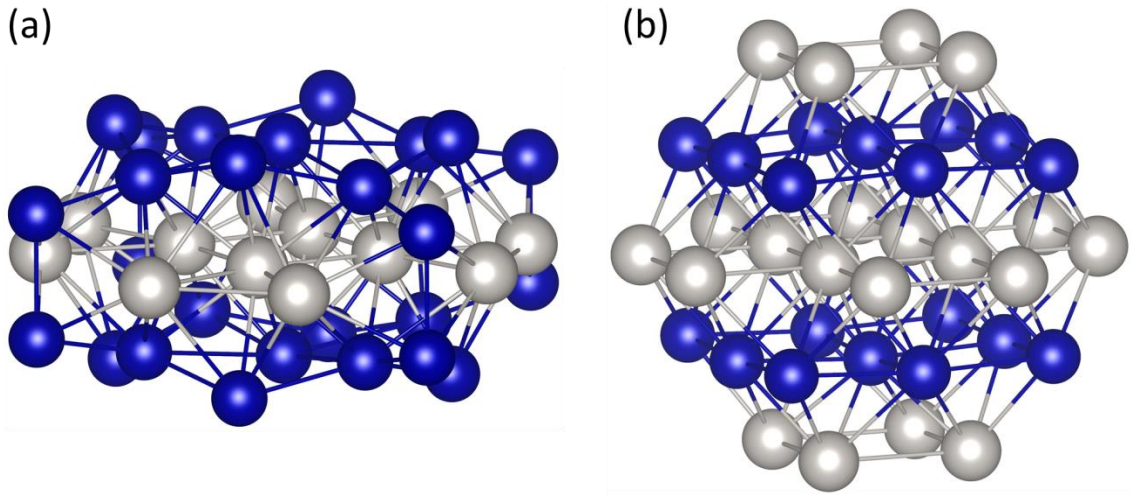

Figure 5.1 Fully relaxed atomic structures of bulk-terminated (a) cuboidal $Co_{26}Pt_{12}$ and (b) cuboctahedral $Co_{18}Pt_{20}$ nanoparticles. In the figure, the blue balls represent Co atoms and the gray balls represent Pt atoms.

Using the noncollinear magnetic DFT calculations, we predicted the magnetic properties of the two bulk-terminated $L1_0$ CoPt nanoparticles along the [001], [100], and [110] high symmetric magnetization directions. In Figure 5.2, we present the relaxed structural and magnetic configuration of the two bulk-terminated CoPt nanoparticles under [001] magnetization. It can be seen in Figure 5.2 that the magnetic moment of Co atoms (about 2.06 μ_B in the cuboid nanoparticle and 2.15 μ_B in the cuboctahedral nanoparticle) is remarkably higher than that of Pt atoms (about 0.45 μ_B in the cuboid nanoparticle and 0.60 μ_B in the cuboctahedral nanoparticle) in the same particle and hence the magnetic moment of the whole nanoparticle is mostly from the contributions of the Co atoms. Since the fully unconstrained approach to noncollinear magnetism permits the variation of both magnetization direction and magnetization magnitude as a function of atomic

positions, our DFT calculations are capable of revealing the extent of surface spin canting in the CoPt nanoparticles.

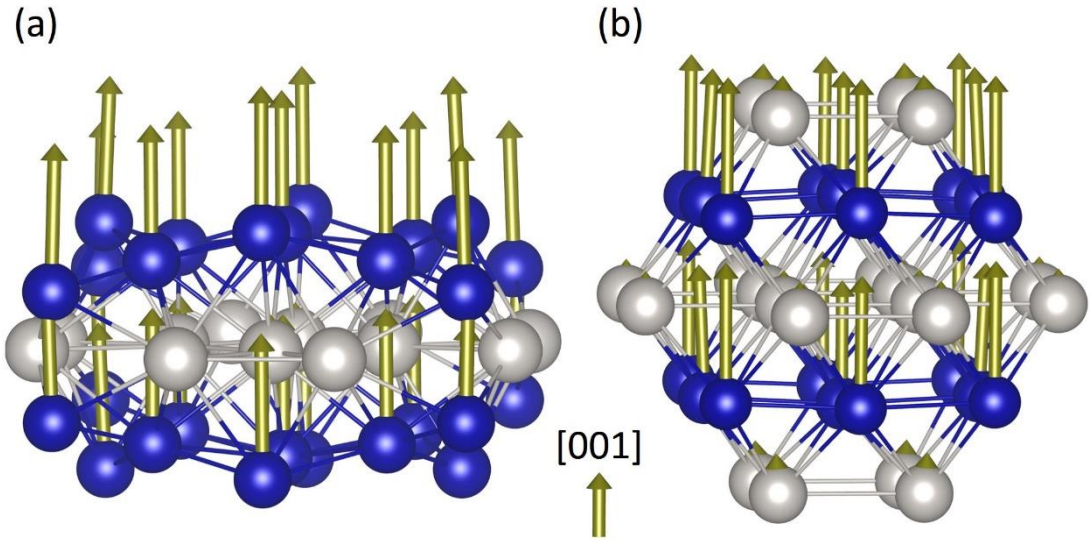

Figure 5.2 Relaxed structure and magnetic configuration of (a) cuboidal and (b) cuboctahedral nanoparticles under [001] magnetization. In the figure, the blue balls represent Co atoms and the gray balls represent Pt atoms. The direction of the golden arrows points to magnetic moment direction, and the length of the golden arrows is proportional to total magnetic moment of atoms. The unit magnitude of the scale arrow in the figure represents a magnetic moment of 1.0 μ_B

Surface spin canting refers to the phenomenon that some of the spins of surface atoms are not aligned with the external magnetic field due to a non-collinear coupling of spins at the surface of magnetic particles [133-135]. The extent of surface spin canting can be gauged using canting angle which is the angle between the magnetic moment and magnetization direction. Our DFT

calculation results reveal that the canting angles are about 2.54° for the Co atoms at the edge sites, about 2.13° for the Co atoms at the corner sites, whereas nearly zero for the other Co and Pt surface atoms of the bulk-terminated cuboidal $Co_{26}Pt_{12}$ nanoparticle. On the surface of the bulk-terminated cuboctahedral $Co_{18}Pt_{20}$ nanoparticle, we find that the canting angles are about 2.77° for the Co atoms residing at the (111) facet sites, about 0.38° for the Co atoms at the (111)/(111) edge sites, about 5.36° for the Pt atoms in the top and bottom (001) surfaces, and nearly zero for the Pt atoms in the middle (001) plane.

In Table 5.1, we summarize the calculated magnetic properties of the two bulk-terminated CoPt nanoparticles. The magnetic moments of the two particles are presented as relative values as compared to those of bulk CoPt crystal. Namely, for a particle containing m Co atoms and n Pt atoms, the relative magnetic moment of a whole particle is given as $\Delta\mu_J = \mu_J(particle) - m \cdot \mu_J^{Co}(bulk) - n \cdot \mu_J^{Pt}(bulk)$. Thus, the positive values of $\Delta\mu_J$ in Table 5.1 indicate enhancement in the overall magnetic moments of the bulk-terminated CoPt particles with respect to the bulk CoPt crystal. Our DFT calculations predict that along the [001] magnetization, the total magnetic moments of the bulk-terminated cuboidal $Co_{26}Pt_{12}$ and cuboctahedral $Co_{18}Pt_{20}$ nanoparticles will respectively increase by 2.38 μ_B and 5.98 μ_B, in comparison to the CoPt crystal with the same number of Co and Pt atoms.

Table 5.1 Magnetic properties calculated for bulk-terminated nanoparticles. Spin magnetic moment change ($\Delta\mu_s$), orbital magnetic moment change ($\Delta\mu_L$) and total magnetic moment change ($\Delta\mu_J$) are calculated with respect to the corresponding values of bulk crystal under [001], [100] and [110] magnetization directions. Magnetic anisotropy energy (MAE), which is defined as energy per atom of magnetized particle relative to that of the same particle under easy axis [001] magnetization, is also presented.

	Cuboidal Nanoparticle			Cuboctahedral Nanoparticle		
	[001]	[100]	[110]	[001]	[100]	[110]
$\Delta\mu_s(\mu_B)$	2.08	1.62	1.60	5.03	4.82	5.12
$\Delta\mu_L(\mu_B)$	0.30	0.71	0.72	0.95	0.61	0.68
$\Delta\mu_J(\mu_B)$	2.38	2.33	2.32	5.98	5.43	5.80
MAE(meV/atom)	0.0	0.41	0.52	0.0	1.36	1.27

To illustrate the origin of the observed overall magnetic moment enhancement shown in Table 5.1 for the bulk-terminated magnetic nanoparticles, we plot in Figure 5.3 the calculated atomic magnetic moment changes with respect to the corresponding element in the bulk CoPt. In these figures, the length of the arrows is proportional to the magnitude of the atomic magnetic moment change and the direction of the arrows indicates the enhancement (parallel to magnetization direction) or reduction (anti-parallel to magnetization direction) in the atomic magnetic moment. It can be seen that the enhancement in the overall magnetic moment of the nanoparticles exclusively comes from the enhanced atomic magnetic moments of the surface atoms of the particles. In the cuboctahedral CoPt nanoparticle, the surface Pt atoms are predicted to have much pronounced magnetic moment enhancement as compared to those Pt atoms in bulk crystal. Interestingly, we observe that surface Pt atoms of the cuboidal nanoparticle have reduced

atomic magnetic moments under the [100] and [110] magnetization (as shown using the antiparallel arrows in Figure 5.3(b) and (c)). It is worth mentioning that we do not observe such a reduction in the atomic magnetic moments of the Pt surface atoms in an un-relaxed cuboidal nanoparticle. Hence, we believe that observed atomic magnetic moment reduction of the Pt surface atoms in the relaxed cuboidal nanoparticle is related to the structural disordering severely deviated from the $L1_0$ ordering of bulk crystal.

Moreover, our DFT results in Table 5.1 predict that the two bulk-terminated CoPt particles still keep the [001] direction as their easy axis and the in-plane [100] or [110] direction as their hard axis. However, we find that the MAE value (1.36 meV/atom) of the bulk-terminated cuboctahedral nanoparticle is much higher than that (0.52 meV/atom) of the bulk-terminated cuboidal nanoparticle. For a CoPt nanoparticle to have the exact same MAE value as bulk crystal, its MAE would be 0.36 meV/atom. Therefore, our present DFT study suggests that size reduction would actually increase both the total magnetic moments and magnetic anisotropy of bulk-terminated CoPt nanoparticles in comparison to bulk $L1_0$ CoPt crystal.

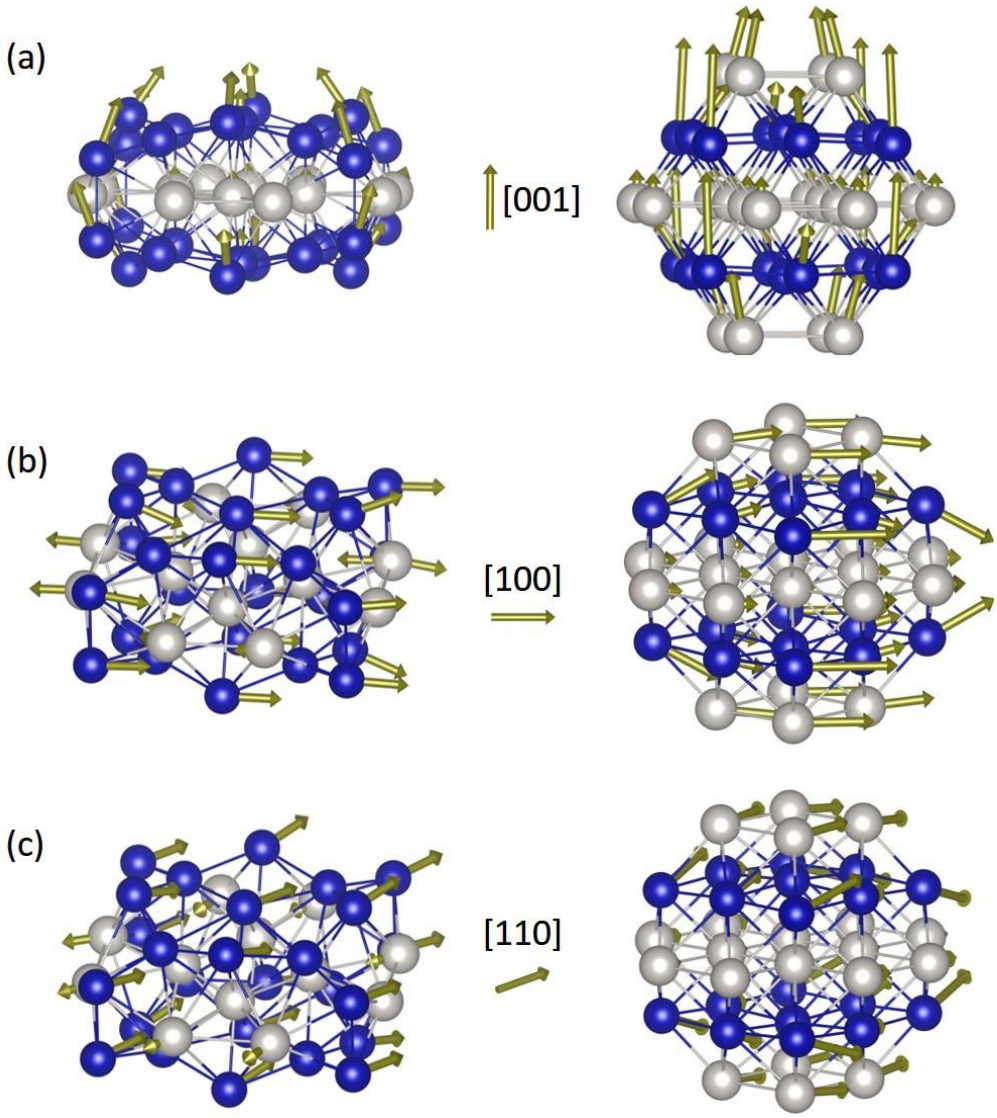

Figure 5.3 Magnetic configuration of bulk-terminated cuboidal (left) and cuboctahedral (right) nanoparticles under (a) [001], (b) [100] and (c) [110] magnetization. In the figure, the blue balls represent Co atoms and the gray balls represent Pt atoms. The golden arrows represent the atomic magnetic moment changes at each atom with respect to the corresponding bulk magnetic moment of the same element. The unit magnitude of the scale arrow in the figure represents a magnetic moment change of 0.2 μ_B.

5.1.2 Magnetic Properties of Surface-Segregated CoPt Nanoparticles

It has been theoretically predicted that Pt atoms would prefer to segregate to the extended surfaces of bulk CoPt crystal [82]. Consequently, the Pt surface segregation phenomenon could occur in our modeled CoPt nanoparticles. To examine this hypothesis, we used the DFT method to compute the Pt surface segregation energies in the cuboidal $Co_{26}Pt_{12}$ and cuboctahedral $Co_{18}Pt_{20}$ nanoparticles containing 38 atoms. In this work, the Pt surface segregation energy (ΔE_{seg}) of a CoPt nanoparticle is calculated as the energy difference between the nanoparticle with its core Pt atoms exchanged positions with the surface Co atoms and the corresponding bulk-terminated nanoparticle. Hence, negative Pt surface segregation energy indicates that it is energetically favorable for Pt to segregate in the outer surface of the nanoparticle. We have examined the Pt surface segregation energies of the CoPt nanoparticles with one, two, three, and four segregated Pt atoms, respectively, and find that the CoPt nanoparticles with four segregated Pt atom in the surface are energetically most favorable.

In Figure 5.4, we present the relaxed structures and energies (in term of ΔE_{seg}) of four possible configurations for the surface-segregated cuboidal $Co_{26}Pt_{12}$ and cuboctahedral $Co_{18}Pt_{20}$ nanoparticles with four segregated Pt atoms. Our DFT results show clearly that these Pt surface-segregated nanoparticles have lower energies than that of the corresponding bulk-terminated nanoparticles, revealing a strong Pt surface segregation tendency in the CoPt nanoparticles from a thermodynamic aspect.

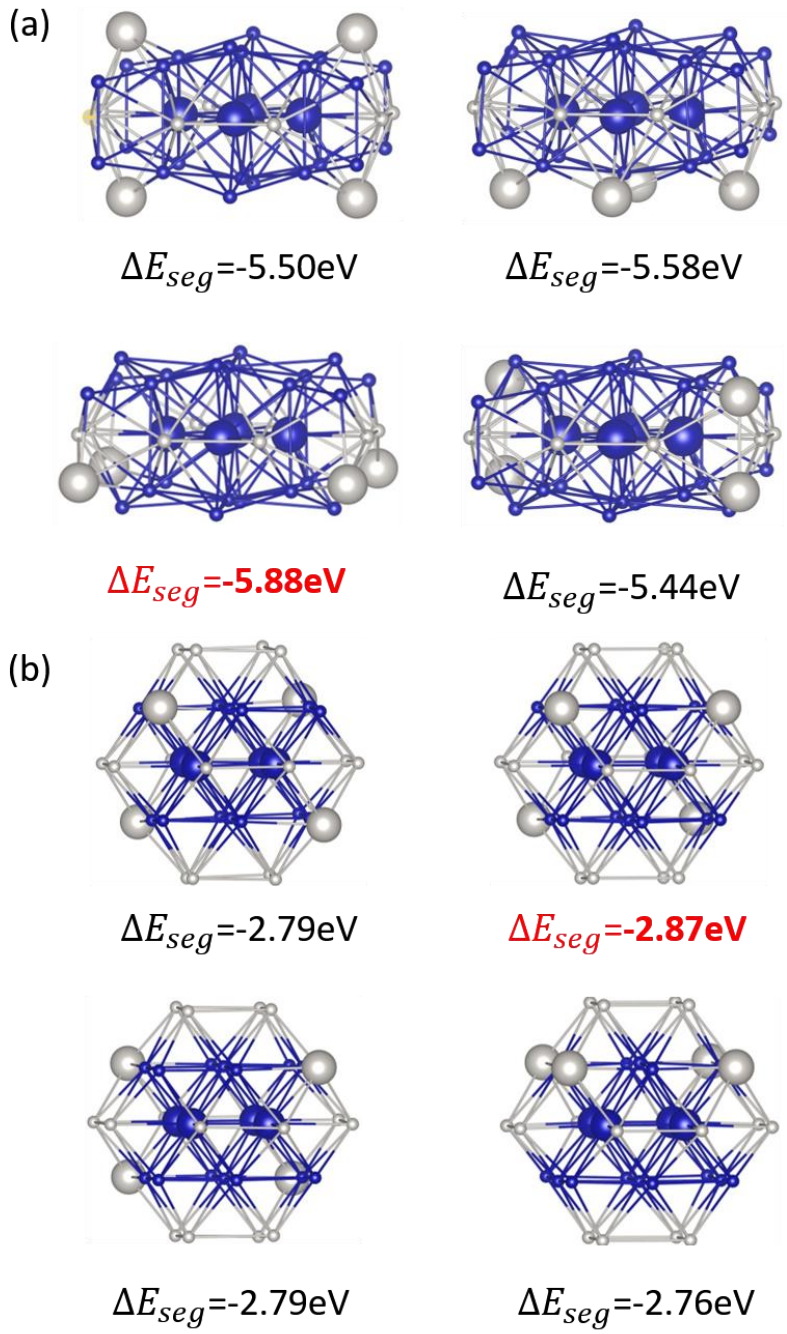

Figure 5.4 Fully relaxed atomic structures of surface-segregated (a) cuboidal and (b) cuboctahedral nanoparticles. In the figure, the blue balls represent Co atoms and the gray balls represent Pt atoms. The large balls indicate the lattice sites involved in Pt surface segregation.

In our modeled bulk-terminated cuboidal CoPt nanoparticle, there are four Pt atoms in the core of the particle. In this study, we predict that the lowest-energy configuration of the surface-segregated cuboidal nanoparticles (with ΔE_{seg} of -5.88 eV) is that all those four core Pt atoms exchanged positions with four surface Co atoms at the corner sites on the same (001) surface. In our modeled bulk-terminated cuboctahedral CoPt nanoparticle, there are four Pt atoms and two Co atoms in the core of the particle. Among the surface-segregated cuboctahedral $Co_{18}Pt_{20}$ nanoparticles, we find that the lowest-energy configuration (with ΔE_{seg} of -2.87 eV) is in which the four originally core Pt atoms segregate to the corner sites of two (001) layers of Co atoms. In this study, we chose these two configurations with the lowest energies as representative structures and used the DFT noncollinear magnetism method to calculate the magnetic properties of the two surface-segregated CoPt nanoparticles.

We present the predicted magnetic properties in Table 5.2 and magnetic configurations in Figure 5.5 for these two surface-segregated CoPt nanoparticles. It is noticeable in Table 5.2 that the overall magnetic moment of the surface-segregated cuboidal $Co_{26}Pt_{12}$ nanoparticle is reduced as compared to that of bulk CoPt crystal. This reduction in overall magnetic moment could be understood from the changes in atomic magnetic moments plotted in Figure 5.5. For example, our DFT results for the surface-segregated cuboidal $Co_{26}Pt_{12}$ nanoparticle under [001] magnetization show that the four core Co atoms (note: the ones were moved inside from surface associated with Pt surface segregation) have magnetic moments about $1.78\mu_B$, reduced by 9.2% as compared to the magnetic moment ($1.96\mu_B$) of the Co atoms in $L1_0$ bulk CoPt. Although the surface-segregated cuboctahedral $Co_{18}Pt_{20}$ nanoparticle still exhibit enhanced overall total magnetic moment as

compared to bulk crystal, its surface Pt atoms are predicted to have no enhanced atomic magnetic moments in this work.

Table 5.2 Magnetic properties calculated for surface-segregated nanoparticles. Spin magnetic moment change ($\Delta\mu_s$), orbital magnetic moment change ($\Delta\mu_L$) and total magnetic moment change ($\Delta\mu_J$) are calculated with respect to the corresponding values of bulk crystal under [001], [100] and [110] magnetization directions. Magnetic anisotropy energy (MAE), which is defined as energy per atom of magnetized particle relative to that of the same particle under easy axis [001] magnetization, is also presented.

	cuboidal nanoparticle			cuboctahedral nanoparticle		
	[001]	[100]	[110]	[001]	[100]	[110]
$\Delta\mu_s(\mu_B)$	0.13	-0.16	-0.18	1.14	0.90	0.88
$\Delta\mu_L(\mu_B)$	-0.28	0.18	0.17	-0.12	0.08	0.11
$\Delta\mu_J(\mu_B)$	-0.15	0.02	-0.01	1.02	0.98	0.99
MAE(meV/atom)	0.0	0.42	0.42	0.0	0.76	0.75

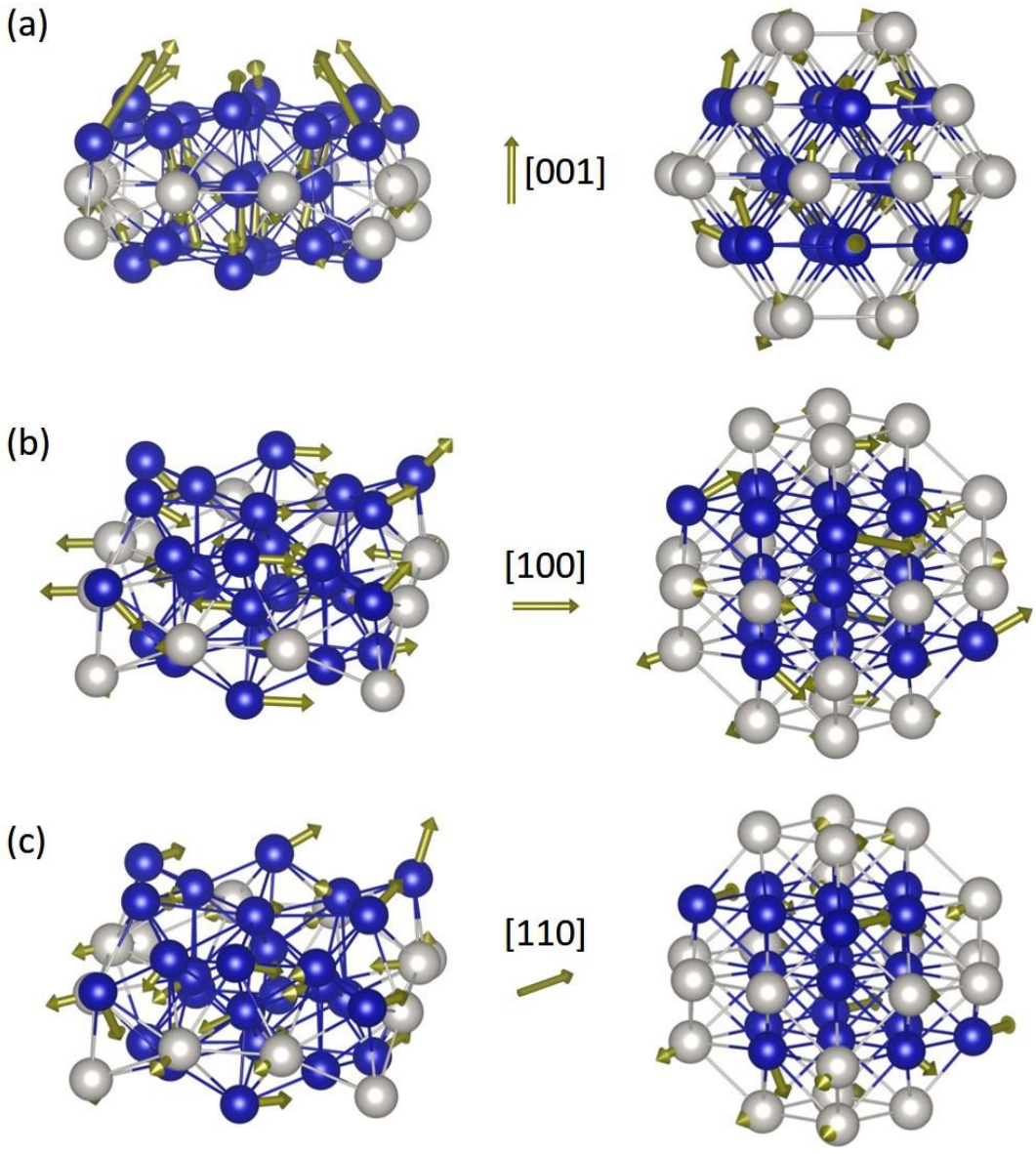

Figure 5.5 Magnetic configuration of surface-segregated cuboidal (left) and cuboctahedral (right) nanoparticle under (a) [001], (b) [100] and (c) [110] magnetization. In the figure, the blue balls represent Co atoms and the gray balls represent Pt atoms. The golden arrows represent the atomic magnetic moment change at each atom with respect to the corresponding bulk magnetic moment. The unit magnitude of the scale arrow represent a magnetic moment change of 0.2 μ_B.

5.1.3 Comparison of the properties of bulk-terminated and surface-segregated nanoparticles

In summary, we identify the following changes induced by Pt surface segregation to the physical properties of CoPt nanoparticles in this study.

(1) Chemical composition. In terms of Co atomic concentration, our modelled bulk-terminated cuboidal $Co_{26}Pt_{12}$ nanoparticle has an overall composition of 68.4 at.% (higher than the stoichiometric value of CoPt crystal), a surface composition of 76.5 at.%, and a core composition of 0.0 at.%, whereas our modelled bulk-terminated cuboctahedral $Co_{18}Pt_{20}$ nanoparticle has an overall composition of 47.4 at.% (lower than the stoichiometric value of CoPt crystal), a surface composition of 50.0 at.%, and a core composition of 33.3 at.%. In the both nanoparticles, our DFT calculations predict that it is energetically favorable for the core Pt atoms to exchange the positions with surface Co atoms. The lowest-energy configurations of both the surface-segregated cuboidal and cuboctahedral nanoparticles have a core composition of 100.0 at. %, of Co.

(2) Crystal symmetry. As same as $L1_0$ crystal, the bulk-terminated cuboidal $Co_{26}Pt_{12}$ and cuboctahedral $Co_{18}Pt_{20}$ nanoparticles possess a symmetry group of D_{4h}, which has sixteen symmetry operations including a principal 4-fold rotation (C_4) about the [001] axis, a reflection (σ_h) made through the central horizontal (001) plane, and an inversion (i) around the center of the nanoparticle. Due to surface segregation, our surface–segregated nanoparticles are found to have reduced groups of symmetry. The surface–segregated cuboidal nanoparticle is predicted to have a symmetry group of C_{4v} by losing symmetry operations σ_h and i, and the surface–segregated

cuboctahedral nanoparticle has a symmetry group of C_{2h} by losing symmetry operations C_4 and σ_h.

(3) Magnetic anisotropy. In this study, we predict that the two surface-segregated nanoparticles have the same magnetic axes ([001] magnetization direction as "easy axis" whereas in-plane [100] or [110] magnetization direction as "hard axis") as the two corresponding bulk-terminated nanoparticles. However, surface segregation is found to reduce the out-of-plane anisotropy of the CoPt nanoparticles. The out-of-plane MAE ((E[100] or E[110])-E[001]) of the surface-segregated cuboidal nanoparticle is predicted to be 0.42meV/atom which is reduced by 19 % as compared to the value (0.52meV/atom) of the bulk-terminated particle. More pronouncedly, surface segregation could diminish the MAE value by 45% (changing from 1.37meV/atom to 0.76meV/atom) for the cuboctahedral $Co_{18}Pt_{20}$ nanoparticle. Moreover, the in-plane MAE (energy difference between E[100] and E[110]) is predicted to be about 0.10 eV for the two bulk-terminated nanoparticles but to be less than 0.01 eV for the two surface-segregated nanoparticles. Hence, it is inferred that the surface segregation reduces both the out-of-plane and in-plane anisotropy of magnetic CoPt nanoparticles.

(4) Magnetic moment. Comparing the values in Table 5.1 and Table 5.2, we can find that surface segregation could also reduce the total magnetic moment of the CoPt nanoparticles. Under magnetization along [001] direction, the overall magnetic moment of the surface-segregated cuboidal and cuboctahedral nanoparticles is predicted to be $2.52\mu_B$ and $4.96\mu_B$ lower than that of the corresponding bulk-terminated nanoparticle, respectively. Our calculation results in Table 5.3 indicate that the magnetic moment reduction in the surface-segregated cuboctahedral nanoparticle is mainly due to a decrease in the atomic spin magnetic moments of the Co and Pt atoms. The results in Table 5.3 also show that our calculated atomic spin and orbital moments in bulk $L1_0$

CoPt crystal are in good agreement with the experimental values measured from CoPt thin films [89], with a notable underestimation on the orbital moment of Co atoms. Moreover, our DFT predictions for both the bulk-terminated and surface-segregated nanoparticles exhibit a similar degree of agreement with the experimental data for CoPt nanoparticles [136] and thus cannot be used to determine if the surface segregation occurred in the experimental samples.

Table 5.3 Summary of the predicted atomic spin magnetic moment (μ_S) and orbital magnetic moment (μ_L) averaged at Co and Pt sites of bulk $L1_0$ CoPt crystal and our modelled cuboctahedral nanoparticles under [001] magnetization direction. For comparison, we list the corresponding experimental values measured from $Co_{50}Pt_{50}$ thin film about 40 nm thick [89] and annealed $Co_{1-x}Pt_x$ (x=0.49) nanoparticles with average diameter of 3.3 nm [136].

	Co atoms		Pt atoms	
	$\mu_S(\mu_B)$	$\mu_L(\mu_B)$	$\mu_S(\mu_B)$	$\mu_L(\mu_B)$
Bulk crystal	1.86	0.10	0.39	0.07
Thin film (experiment) [89]	1.76	0.26	0.35	0.09
Bulk-terminated particle	2.06	0.11	0.46	0.14
Surface-segregated particle	1.96	0.06	0.36	0.13
Particle (experiment) [136]	1.98	0.20	0.52	0.10

5.2 MAGNETIC PROPERTIES OF COPT LOW INDEX SURFACES

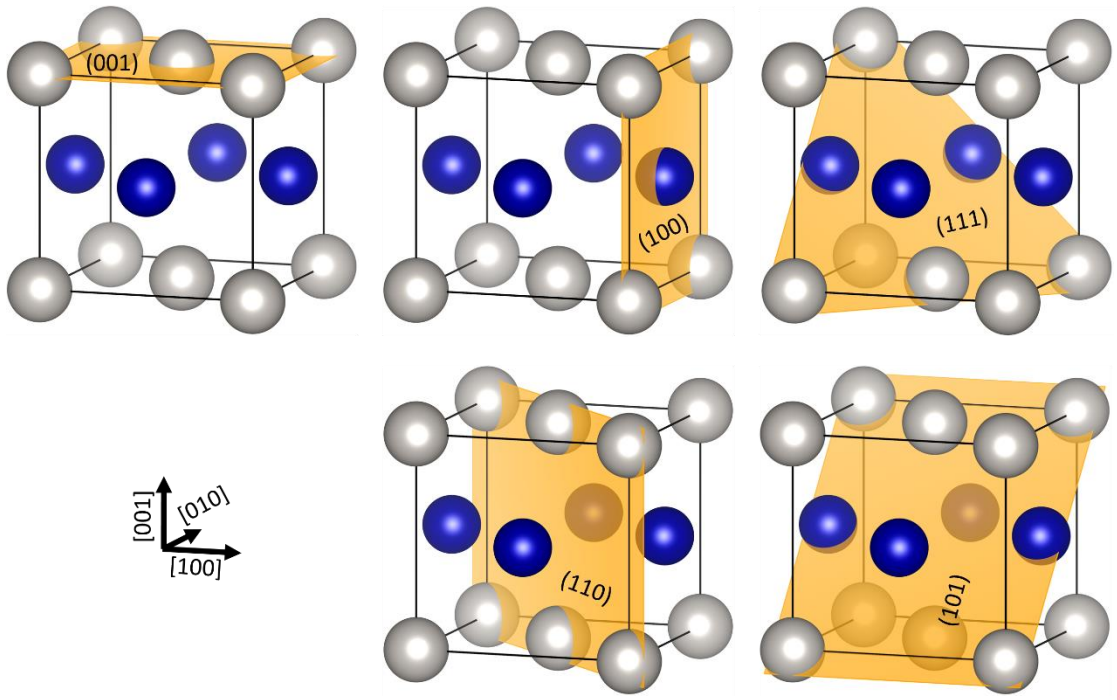

Figure 5.6 Lattice structure and crystallographic surfaces of $L1_0$ CoPt crystal. In the figure, the blue balls represent Co atoms, the gray balls represent Pt atoms, and the yellow planes showing the five low-index surfaces investigated in this work.

In this work, we studied the magnetic properties of five low-index (i.e., (001), (100), (110), (101) and (111)) surfaces (shown in Figure 5.6) of $L1_0$ CoPt alloy. Specifically, we used eight-layer slab cells in our DFT calculations for modeling (100), (101), and (111) surfaces whereas nine-layer slab cells for (001) and (110) surfaces. Thus, the top and bottom of our surface slabs have the same chemical composition and crystal structure. In each surface slab cell, we added a vacuum region of 12Å in the direction normal to the surface in order to avoid the artificial interactions between the slab and its images. In the DFT calculations, the Brillouin zone was sampled using a 10×10×1

k-point mesh for (001) and (100) surfaces, a 7×14×1 k-point mesh for (111) surfaces, and a 7×10×1 k-point mesh for (101) and (110) surfaces, respectively.

5.2.1 Bulk Terminated Surfaces

5.2.1.1 Structural Properties

In this study, we employed the DFT calculation method to fully optimize the atomic structure of bulk-terminated CoPt (001), (100), (110), (101) and (111) surfaces for which the chemical composition of all the layers is exactly determined by $L1_0$ CoPt crystal. Namely, each atomic layer of the bulk-terminated (100), (101) and (111) surface contains 50% Co and 50% Pt, whereas the bulk-terminated (001) and (110) surfaces consist of alternative pure Co and Pt layers. In the following sections, (001)-Co and (110)-Co refer to the (001) and (110) surfaces with Co-layer as the outermost termination; (001)-Pt and (110)-Pt refer to the (001) and (110) surfaces with Pt-layer as the outermost termination. Owing to surface relaxation [137], the separations in the atomic layers near the relaxed CoPt surfaces were found to differ from the corresponding layer spacing in bulk crystal. As indicated in Table 5.4, all the bulk-terminated CoPt surfaces exhibit a contraction (negative Δ_{12}) between the first and second atomic layers and an expansion (positive Δ_{23}) between the second and third atomic layers. It is noticeable in Table 5.4 that the loosely packed (101) surface was predicted to have the largest degree of surface relaxation (Δ_{12}= -16.9% and Δ_{23}=10.4%) whereas the closely packed (111) surface has the slightest degree of surface relaxation (Δ_{12}= -2.8% and Δ_{23}=1.2%). Thus, our DFT predictions for the CoPt alloy surfaces are consistent with the general trend that the most close-packed surfaces would have the least surface relaxation for transition metal surfaces [138,139].

Table 5.4 Predicted structural and energetic properties of bulk-terminated CoPt surfaces. C_s is the chemical composition of the outermost surface layer. Δ_{12} and Δ_{23} give the spacing relaxation (in percent), relative to the bulk crystal layer spacing d, between the first and second atomic layers and between the second and third atomic layers, respectively. Positive (negative) values of Δ_{12} and Δ_{23} signify expansions (contractions).

Surface	C_s	Surface Relaxation			Energy (J/m^2)	
		Δ_{12} (%)	Δ_{23} (%)	d (Å)	This work	Ref. [20]
(001)-Co	$Co_{100}Pt_0$	-4.3	+1.6	1.862	2.161	2.192
(001)-Pt	Co_0Pt_{100}	-5.1	+1.4			
(100)	$Co_{50}Pt_{50}$	-5.5	+2.9	1.912	2.107	2.125
(101)	$Co_{50}Pt_{50}$	-16.9	+10.4	1.334	1.989	2.024
(110)-Co	$Co_{100}Pt_0$	-24.3	+6.4	1.352	2.026	2.039
(110)-Pt	Co_0Pt_{100}	-7.0	+4.45			
(111)	$Co_{50}Pt_{50}$	-2.8	+1.2	2.188	1.658	1.680

In Table 5.4, we also report the calculated surface energies of these bulk-terminated CoPt surfaces. Here, the surface energy of each surface was computed as the energy difference, between the optimized surface slabs and the bulk crystal having the same chemical formula, normalized by the exposed surface area. It is noted that we report in Table 5.4 the surface energy averaged over both pure Co and pure Pt terminated (001) and (110) surfaces. In this study, we predict that the closely packed (111) surface has the lowest surface energy of 1.658 J/m^2 whereas the (001) surface has the highest averaged surface energy of 2.161 J/m^2. Our present DFT results are found to agree well with the results from a previous first principles calculation using the Perdew, Burke, and Ernzerhof (PBE) exchange-correlation functional and a low energy cutoff of 335 eV [20].

5.2.1.2 Magnetic Properties

Furthermore, we used the non-collinear spin-polarized DFT calculation method to relax the geometric and electronic structures of the bulk-terminated CoPt surfaces under the magnetization directions normal (out-of-plane) and parallel (in-plane) to these surfaces.

As depicted in Figure 5.7 and reported in Table 5.5, the atoms on the outermost layer of the bulk-terminated CoPt surfaces are predicted to have magnetic moments differing from the corresponding values of the same elements in bulk CoPt crystal. For example, Figure 5.7(a) shows that the outermost Co atoms of (001)-Co surface have magnetic moments about $0.11\mu_B$ larger than the magnetic moment ($1.96\mu_B$) of bulk Co atoms under the same [001] magnetization direction. The observed magnetic moment enhancement is believed to result from weaker ligand field surrounding these surface atoms [140]. More interestingly, our results in Figure 5.7(b) for (101) surface show that the direction of the magnetic moments of the surface atoms could deviate from the specified magnetization direction (i.e., spin canting that is originated from the antisymmetric exchange interaction between spins, known as the Dzyaloshinskii-Moriya (DM) interaction [141,142]). The spin canting is expected to occur in those magnets with electrons subjected to the spin-orbital coupling (SOC) and with a structural inversion asymmetry [143]. It should be pointed out that the spin canting angles are exaggerated in Figure 5.7(b) for the purpose of illustration. Actually, the canting angle is only about 2.2° for the surface Co atoms and 4.4° for the surface Pt atoms in the outermost layer of bulk-terminated (101) CoPt surface. The spin canting also occurs in the subsurface region but has much small extent. In this study, the surface magnetic moment enhancement and spin canting have been observed in the bulk-terminated CoPt surfaces under both the out-of-plane and in-plane magnetization directions.

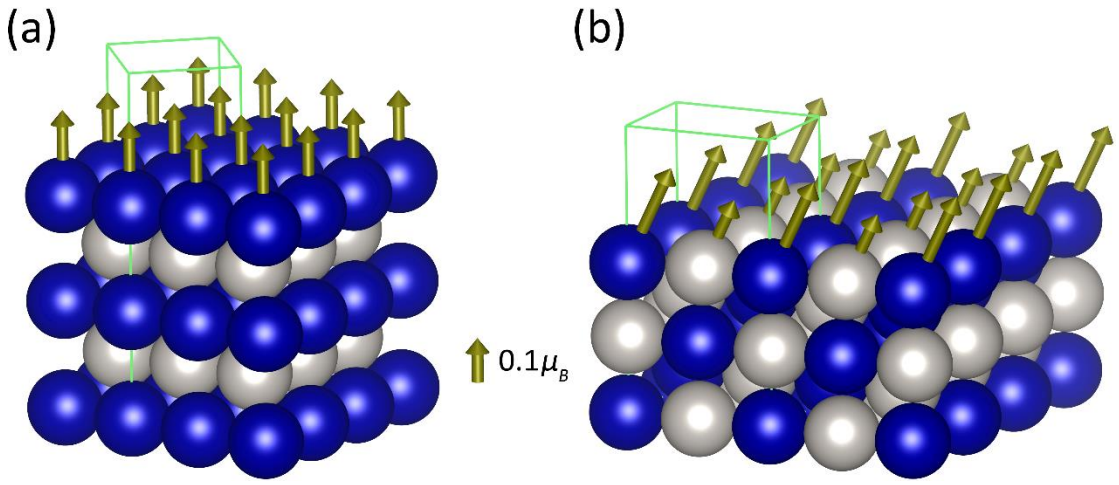

Figure 5.7 Predicted magnetic configuration of (a) (001)-Co and (b) (101) bulk-terminated surface of CoPt crystal under the magnetization direction normal to the surface. In the figure, the blue balls represent Co atoms and the gray balls represent Pt atoms. The golden arrows denote the differences in the magnetic moment of surface atoms relative to that of the corresponding bulk atoms. The green boxes show the slab cells employed in this study.

We summarize our calculated values of the spin magnetic moments (μ_S), orbital magnetic moments (μ_L) and spin canting angle of the outermost surface atoms on bulk-terminated surfaces in $L1_0$ CoPt alloy under the out-of-plane magnetization direction in Table 5.5. Our results indicate that, as compared to the corresponding bulk atoms, the surface Co atoms exhibit more pronounced magnetic moment enhancement than the surface Pt atoms. In addition, the magnetic moment enhancement of the surface Co atoms are mostly derived from their enhanced spin magnetic moments. Our predicted magnetic enhancement of bulk-terminated CoPt surface is compatible with the value (roughly $0.12\mu_B$) from a previous calculation for CoPt superstructures on Pt substrates using screened Korringa-Kohn-Rostoker (SKKR) method [56]. Our results in Table 5.5 also show that the surface spin canting is observed only on (101) and (111) surfaces. The existence

of two orthogonal mirror symmetric planes normal to the (001), (110) and (100) surfaces prevents the magnetic moment of the surface atoms deviating from the out-of-plane magnetization direction of these surfaces.

Table 5.5 Predicted spin magnetic moments (μ_s), orbital magnetic moments (μ_L) and spin canting angles of the outermost surface atoms on bulk-terminated CoPt surfaces under the magnetization direction normal to the surface.

Surface	μ_S (μ_B)		μ_L (μ_B)		Canting Angle (°)	
	Co	Pt	Co	Pt	Co	Pt
(001)-Co	1.96	-	0.11	-	0.0	-
(001)-Pt	-	0.36	-	0.09	-	0.0
(100)	1.98	0.39	0.11	0.12	0.0	0.0
(101)	2.01	0.44	0.11	0.12	2.2	4.4
(110)-Co	1.98	-	0.06	-	0.0	-
(110)-Pt	-	0.41	-	0.13	-	0.0
(111)	1.94	0.37	0.10	0.09	0.8	2.7
Bulk	1.86	0.39	0.10	0.07	0.0	0.0

Moreover, we evaluated the magnetic anisotropy energy (MAE) of each bulk terminated CoPt surface by computing its energy difference between out-of-plane ($\perp$) and in-plane ($\parallel$) magnetization. Hence, a positive value of the surface MAE implies the in-plane magnetization for the surface is more energetically favorable than the out-of-plane magnetization. Our calculation results in Table 5.6 show that the in-plane magnetization is preferable on most bulk-terminated surfaces. We also give in Table 5.6 the relevant bulk MAE value which is the energy difference of bulk CoPt crystal under the out-of-plane and in-plane magnetization directions as same as those of

the surface. Comparing the surface MAE and bulk MAE, we notice that the surface values are always more positive than the bulk values. Consequently, our calculation results suggest that the bulk-terminated CoPt surfaces lead to surface anisotropy favoring in-plane magnetization.

Table 5.6 Calculated magnetic anisotropy energy (MAE) of bulk-terminated surfaces in $L1_0$ CoPt alloy. Here, f.u. refers to a CoPt formula unit.

Surface index	⊥direction	∥direction	MAE (meV)	MAE/f.u. (meV/f.u.)	Bulk MAE (meV/f.u.)
(001)-Co	[001]	[100]	-0.12	--	-0.73
(001)-Pt	[001]	[100]	1.30		
(100)	[100]	[001]	9.24	2.31	0.73
(101)	[101]	$[\bar{1}01]$	2.06	0.51	0.00
(110)-Co	[110]	$[1\bar{1}0]$	-1.15	--	0.00
(110)-Pt	[110]	$[1\bar{1}0]$	3.48		
(111)	[111]	$[1\bar{2}1]$	0.21	0.05	-0.12

5.2.2 Pt Segregated Surfaces

5.2.2.1 Structural Properties

Surface segregation refers to the phenomenon that the chemical composition at the thermodynamically annealed surface of alloys is different from the corresponding value of bulk-terminated surface [68]. One main reason underlying the surface segregation phenomenon is that the total energy of the surface will decrease if some constituent of the alloys moves to the surface from the bulk region [68]. Illustrated in Figure 5.8 using a $\sqrt{2}\times\sqrt{2}$ supercell of Co-terminated CoPt (001) surface, our DFT calculation results show that the total energy of the surface slab

decreases by 0.69 eV with one surface-segregated Pt atom, 1.05 eV with two surface-segregated Pt atoms, 1.54 eV with three surface-segregated Pt atoms, and 1.93 eV with four surface-segregated Pt atoms, respectively. The Pt surface segregation was achieved by swapping the Pt atoms at the subsurface layer with the Co atoms at the outmost surface in the bulk-terminated (001) surface. Consequently, we predict for CoPt (001) surface that the Pt-segregated surface (with 100 at.% Pt at the outermost layer and 100 at.% Co at the second subsurface layer, shown in Figure 5.8(e)) has the lowest energy as compared to that with Co-termination (Figure 5.8(a)) or partial Pt segregation (Figure 5.8(b-d)). Following the same computational approach, we determine that the Pt-segregated surface (with 100 at.% Pt at the outermost layer and 100 at.% Co at the second subsurface layer, shown in Figure 5.9) is always the most energetically favorable one for the (001), (100), (110), (101) and (111) surfaces of the $L1_0$ CoPt crystal.

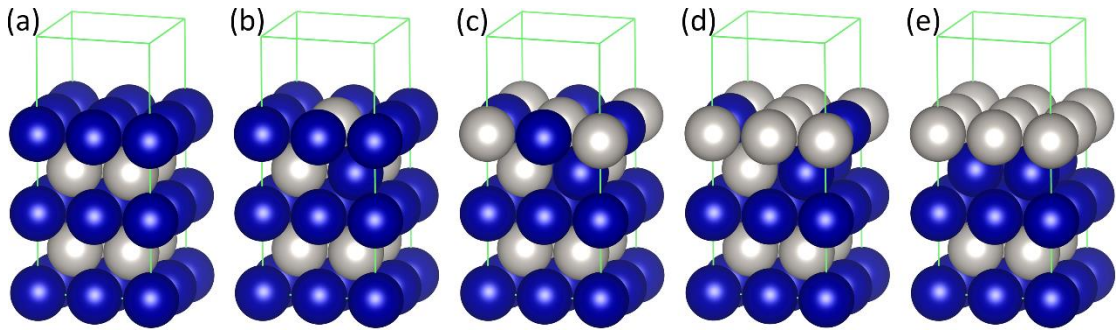

Figure 5.8 Atomistic structure of CoPt (001) surface with (a) bulk-terminated 100 at.% Co termination, (b) 25 at.%, (c) 50 at.%, (d) 75 at.%, and (e) 100 at.% Pt surface segregation. In the figure, the blue balls represent Co atoms and the gray balls represent Pt atoms.

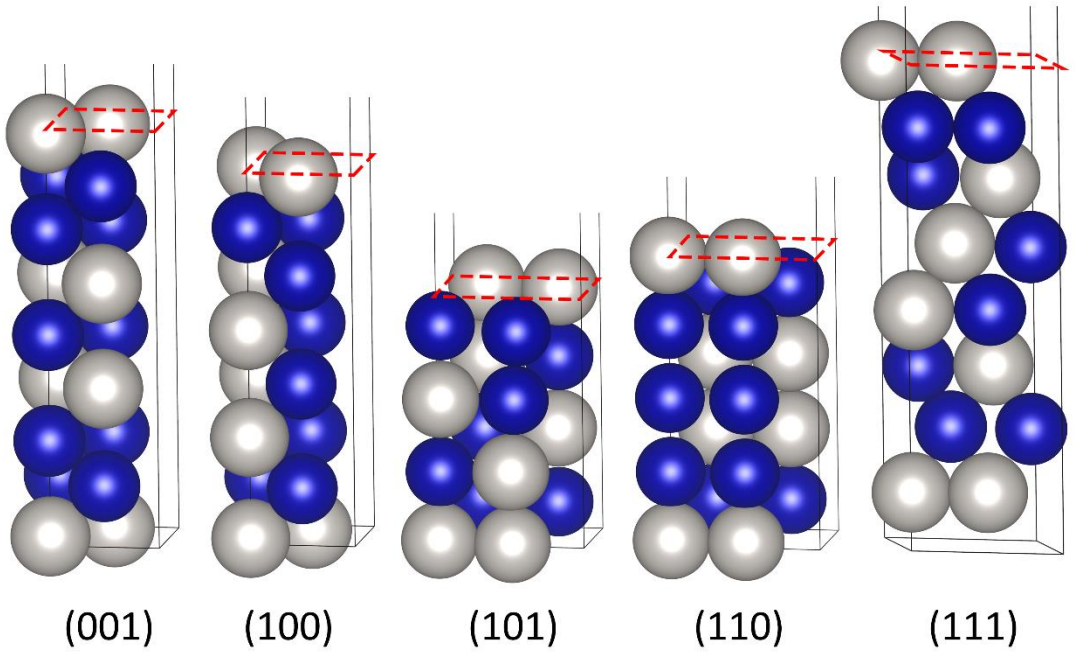

Figure 5.9 Pt-segregated surfaces of $L1_0$ CoPt crystal. In the figure, the blue balls represent Co atoms and the gray balls represent Pt atoms.

Quantitatively, the surface segregation extent of a particular element in the alloy could be gauged in terms of surface segregation energy, which is the energy difference between the configurations with this element in the outermost surface or in the crystal beneath the surface [144]. In this study, we have calculated the Pt surface segregation energy of various $L1_0$ CoPt surfaces by evaluating the energy difference, normalized by the number of segregated Pt atoms, between the Pt-segregated surface and the corresponding bulk-terminated surface. Hence, negative Pt surface segregation energy implies that it is energetically favorable for Pt to segregate to the outermost surface. We present our calculated Pt surface segregation energy in CoPt surfaces in Table 5.7. Our results agree well with previous predictions from the first principles calculation using a low cutoff energy of 400 eV [82].

Table 5.7 Predicted structural and energetic properties of Pt-segregated CoPt surfaces. Δ_{12} and Δ_{23} give the spacing relaxation (in percent), relative to the bulk crystal layer spacing *d* (also given), between the first and second atomic layers and between the second and third atomic layers, respectively. Positive (negative) values of Δ_{12} and Δ_{23} signify expansions (contractions).

Surface	Surface Relaxation			Segregation Energy (eV)	
	Δ_{12} (%)	Δ_{23} (%)	*d* (Å)	This work	Ref.[82]
(001)	-2.5	-16.2	1.862	-0.47	-0.46
(100)	-4.2	-8.9	1.912	-0.46	-0.42
(101)	-5.4	-2.0	1.334	-0.05	-
(110)	-8.7	-6.7	1.352	-0.13	-
(111)	-1.5	-8.1	2.188	-0.37	-0.34

In Table 5.7 we also give the values of interlayer spacing relaxation of the Pt-segregated $L1_0$ CoPt surfaces, relative to the bulk crystal layer spacing. As compared to that of the bulk-terminated surfaces (in Table 5.4), the contraction relaxation between the outermost and second layer become smaller but significant contraction appears between the second and third layer of the Pt-segregated surfaces. We attribute this large contraction between the second and third layer to the high concentration of Co with atomic radius smaller than Pt in this subsurface region. Overall, the Pt-segregated surfaces have larger contraction in the direction normal to the surface than the bulk-terminated surfaces of CoPt crystal.

5.2.2.2 Magnetic Properties

We have also predicted the magnetic properties of the Pt-segregated CoPt surfaces under the magnetization direction normal (out-of-plane) and parallel (in-plane) to these surfaces. In Table 5.8, we report the calculated magnetic moments of Pt and Co atoms in the Pt-segregated surfaces. First, we computed the difference in total magnetic moments (normalized by the number of surface atoms) between the Pt-segregated and the corresponding bulk-terminated surface slabs. Our results show that the Pt surface segregation could cause remarkable reduction in the magnetic moments of the (001), (100), and (111) surfaces, a slight reduction in the magnetic moment of the (101) surface, but appreciable enhancement in the magnetic moment of the (110) surface in $L1_0$ CoPt crystal.

Furthermore, we computed both the spin and orbital magnetic moments of the Pt and Co atoms in the Pt-segregated surfaces and compared these values with those of the atoms in the bulk-terminated surfaces (see Table 5.5). It should be mentioned that the Pt atoms in the outermost layer of the Pt-segregated surfaces consist of the Pt atoms originally at a Pt sub-lattice site (denoted as Pt_{Pt}) and the segregated ones in replace of Co surface atoms (denoted as Pt_{Co}), and the Co atoms in the subsurface layer of the Pt-segregated surfaces consist of the Co atoms originally at a Co sub-lattice site (denoted as Co_{Co}) and ones moved there from the outermost surface (denoted as Co_{Pt}). Our calculation results in Table 5.8 indicate that the two types of the Pt outermost surface atoms and Co subsurface atoms have distinguishable magnetic properties mainly due to their different second-nearest neighbors. For instance, the orbital magnetic moment of the subsurface Co_{Pt} atoms are predicted to be only half of that of the subsurface Co_{Co} atoms in the Pt-segregated (101) surface.

Table 5.8 Predicted magnetic properties of Pt-segregated CoPt surfaces under the magnetization direction normal to the surface. The properties include the total magnetic moment change ($\Delta\mu$) per surface atom due to Pt surface segregation, the spin magnetic moments (μ_s) and orbital magnetic moments (μ_L) of the Pt and Co atoms in the surfaces (the number in parenthesis indicates the layer in which the atoms are. 1: outermost layer, and 2: subsurface layer), and the spin canting angles of the outermost surface Pt atoms.

		(001)	(100)	(101)	(110)	(111)
$\Delta\mu$ (μ_B)		-0.48	-0.21	-0.04	0.13	-0.32
μ_S (μ_B)	Pt_{Co}(1)	0.26	0.32	0.39	0.47	0.23
	Pt_{Pt}(1)	-	0.32	0.46	-	0.21
	Co_{Pt}(2)	1.85	1.88	1.90	1.93	1.89
	Co_{Co}(2)	-	1.88	1.88	-	1.92
μ_L (μ_B)	Pt_{Co}(1)	0.07	0.07	0.13	0.13	0.03
	Pt_{Pt}(1)	-	0.08	0.12	-	0.02
	Co_{Pt}(2)	0.05	0.06	0.05	0.05	0.10
	Co_{Co}(2)	-	0.06	0.10	-	0.10
Canting Angle (°)	Pt_{Co}	0.0	0.0	0.3	0.0	1.1
	Pt_{Pt}	-	0.0	2.3	-	1.0

More importantly, our results in Table 5.8 indicate that the spin and orbital magnetic moments of both the Pt outermost surface atoms and Co subsurface atoms in the Pt-segregated (001), (100), and (111) surfaces are noticeably lower than the values of the atoms in the corresponding bulk-terminated surfaces. This explains the observed remarkable reduction in the

magnetic moments of these three surfaces due to Pt surface segregation. In contrast, the magnetic moments of the Pt outermost surface atoms and Co subsurface atoms in the Pt-segregated (101) surface are found to change little from those values of the atoms in the corresponding bulk-terminated surface. The slight reduction in the total magnetic moment of the Pt-segregated (101) surface as compared to the bulk-terminated (101) surface is attributed to the reduction in the orbital magnetic moments of the subsurface Co_{Pt} atoms in the Pt-segregated (101) surface. Interestingly, we find that the segregated Pt atoms in the outermost layer of the Pt-segregated (110) surface have enhanced magnetic moments (μ_S= 0.47μ_B, μ_L= 0.13μ_B) as compared to that (μ_S= 0.39μ_B, μ_L= 0.07μ_B) of the Pt atoms in the subsurface layer of the corresponding bulk-terminated (110)-Co surface, whereas the segregated Co atoms in the subsurface layer of the Pt-segregated (110) surface have magnetic moments (μ_S= 1.93μ_B, μ_L= 0.05μ_B) only slightly lower than that (μ_S= 1.98μ_B, μ_L= 0.11μ_B) of the Co atoms in the outermost layer of the corresponding bulk-terminated (110)-Co surface. Consequently, Pt surface segregation is predicted to increase the total magnetic moment of the L10 CoPt (110) surface in this study.

Shown in Figure 5.9, Pt surface segregation changes both the chemical composition and the symmetry group of the CoPt surfaces. It is expected that a change in symmetry would affect the spin canting phenomena and magnetic anisotropy of the surfaces. In this study, we still observed the spin canting in the Pt-segregated (101) and (111) surfaces under the magnetization direction normal to the surface. However, our results in Table 5.8 show that the spin canting angles mostly become smaller in the Pt-segregated surfaces as compared to the values (Table 5.5) in the bulk-terminated surfaces. In this study, the value of MAE is the energy difference of the surface under its out-of-plane ($\perp$) magnetization and a high-symmetry in-plane ($\parallel$) magnetization. Comparing the calculated MAE of the Pt-segregated and bulk-terminated surfaces, we notice in

Table 5.9 that the Pt surface segregation in all the CoPt surfaces studied here shifts the MAE values toward more negative. Consequently, our results suggest that Pt surface segregation could potentially to switch the most energetically favored magnetization direction of CoPt surface from in-plane magnetization to out-of-plane magnetization. Indeed, we predict in this work that the out-of-plane magnetization direction of both (101) and (111) CoPt surface becomes preferable than the given in-plane magnetization direction due to Pt surface segregation.

Table 5.9 Comparison of the calculated magnetic anisotropy energy (MAE) of Pt-segregated and bulk-terminated surfaces in $L1_0$ CoPt alloy.

MAE (meV)	(001)	(100)	(101)	(110)	(111)
Pt-segregated	-1.47	0.70	-2.65	-13.28	-1.85
Bulk-terminated	-0.12	9.24	2.06	-1.15	0.21
ΔMAE	-1.35	-8.54	-4.71	-12.13	-2.06

5.2.3 Electronic Structure Origin of Magnetic Anisotropy Energy

Regarding surface magnetic anisotropy, we predict in 5.2.1 that the bulk-terminated CoPt surfaces tend to favor the in-plane magnetization as compared to the corresponding MAE values of bulk CoPt crystal. This phenomenon is particularly interesting for the bulk-terminated (001)-Co and (001)-Pt surfaces, because their out-of-plane [001] magnetization direction is just the easy axis of $L1_0$ CoPt crystal. Moreover, we predict in 5.2.2 that, as compared to the corresponding bulk-terminated surface, the Pt-segregated CoPt surface has a MAE value more negative (i.e., energetically favoring the out-of-plane magnetization). In order to gain understanding on the

observed trend of the MAE for the CoPt surfaces, we discuss qualitatively the influence of the electronic structure of the surface on the value of MAE.

In this study, we define the MAE of a surface as the energy difference between out-of-plane (⊥) vs. in-plane (∥) magnetization configurations (i.e. MAE = E⊥- E∥). Within the second-order perturbation theory [145,146], the MAE of a magnetic system is proportional to the energy change owing to spin-orbital coupling (SOC) interaction. Namely,

$$MAE \propto -\xi^2 \sum_{u,o,\sigma,\sigma'} (2\delta_{\sigma,\sigma'} - 1) \frac{\left|\langle o^\sigma | L_z | u^{\sigma'} \rangle\right|^2 - \left|\langle o^\sigma | L_x | u^{\sigma'} \rangle\right|^2}{\varepsilon_u^{\sigma'} - \varepsilon_o^\sigma} \quad (5.1)$$

where o^σ and $u^{\sigma'}$ represent the eigenstates of the occupied and unoccupied orbitals in spin state $\sigma(\sigma')$ (here, σ, σ' refers to spin up (↑) or spin down (↓)), ε_o^σ and $\varepsilon_u^{\sigma'}$ represent the eigenvalues of the occupied and unoccupied orbitals in spin state $\sigma(\sigma')$, and ξ is a constant representing the strength of spin-orbit coupling effect. In addition, L_z and L_x are angular momentum operators, here z represents the out-of-plane magnetization direction whereas x represents the in-plane magnetization direction. The non-zero matrix elements of the *d* states under L_z and L_x operators are $\langle xz|L_z|yz\rangle = 1$, $\langle x^2 - y^2|L_z|xy\rangle = 2$, $\langle z^2|L_x|yz\rangle = \sqrt{3}$, $\langle x^2 - y^2|L_x|yz\rangle = 1$, and $\langle xy|L_x|xz\rangle = 1$ [145]. It also notes that the denominator of the equation makes only those states in the immediate vicinity of fermi level contribute significantly to the MAE value. Consequently, we focus on the changes of electron densities at the fermi level in below and use equation 5.1 to elaborate the relation between the electronic structure and the MAE of bulk-terminated (001)-Co, bulk-terminated (001)-Pt, Pt-segregated (001), and Pt-segregated (100) CoPt surfaces.

5.2.3.1 Bulk-Terminated (001)-Co and (001)-Pt Surface

Figure 5.10 plots the element and orbital resolved density of states (DOS) of *d* electrons in the $L1_0$ CoPt bulk crystal and in the outermost layer of the bulk-terminated CoPt (001) surface with either Co-termination (i.e., (001)-Co) or Pt-termination (i.e., (001)-Pt). It can be seen in Figure 5.10(a) and (b) that the majority spin-up (↑) states of the Co atoms in bulk crystal and the outermost (001)-Co surface are fully occupied and have nearly zero density in the vicinity of Fermi level. Consequently, the terms involving the coupling of $(\sigma\sigma')$ = (↑↑), (↑↓) and (↓↑) can be neglected in equation 5.1 (Note: the same analysis approach has used in previous study for Co-Pt chains on Pt(111) [147] and FeRh on MgO [148]) whereas the coupling between the unoccupied and occupied minority spin states $(\sigma\sigma')$ = (↓↓) is the dominant component of MAE. Comparing the *d* electron DOS in Figure 5.10(a) and (b), we notice only a significant increase in the density of d_{z^2} with minority spin state (↓) in the vicinity of fermi level for the surface Co atoms of (001)-Co surface. According to equation 5.1, this increase in the density of d_{z^2} states leads to an appreciable positive contribution to the MAE of (001)-Co surface given as follows.

$$\xi_{Co}^2 \sum \frac{\left|\langle z^2|L_x|yz\rangle\right|^2}{\varepsilon_{yz}-\epsilon_{z^2}} \tag{5.2}$$

We compare the predicted *d* electron DOS in Figure 5.10(c) and (d) and also notice an increase in the density of d_{z^2} with minority spin state (↓) in the vicinity of fermi level for the surface Pt atoms of (001)-Pt surface. Similarly, the increase in the density of d_{z^2} states contributes a positive value to the MAE of (001)-Pt surface.

$$\xi_{Pt}^2 \sum \frac{\left|\langle z^2|L_x|yz\rangle\right|^2}{\varepsilon_{yz}-\epsilon_{z^2}} \tag{5.3}$$

Hence, our electronic structure calculation results indicate that the density of minority spin d_{z^2} states for the bulk-terminated (001) surface atoms will increase in the vicinity of the fermi level as compared to those for bulk atoms, and furthermore, our analysis based on the second-order perturbation theory (equation 5.1) suggests that this increase in d_{z^2} DOS adds a positive term to the MAE of the bulk-terminated (001) surfaces as compared to the MAE of CoPt crystal. Thus, we provide an explanation in an electronic scale to our computational results in Table 5.6 showing that the bulk-terminated CoPt surfaces become energetically favor in-plane magnetization as compared to the CoPt bulk crystal. It is worth mentioning that previous computation predicted that the spin-orbit coupling constant ξ_{Pt} (in equation 5.3) was larger by one order of magnitude than ξ_{Co} (in equation 5.2) [149]. Consequently, it is reasonable for us to predict in Table 5.6 that the bulk-terminated CoPt surfaces with Pt-layer termination have more positive MAE values than the same oriented surfaces with Co-layer termination.

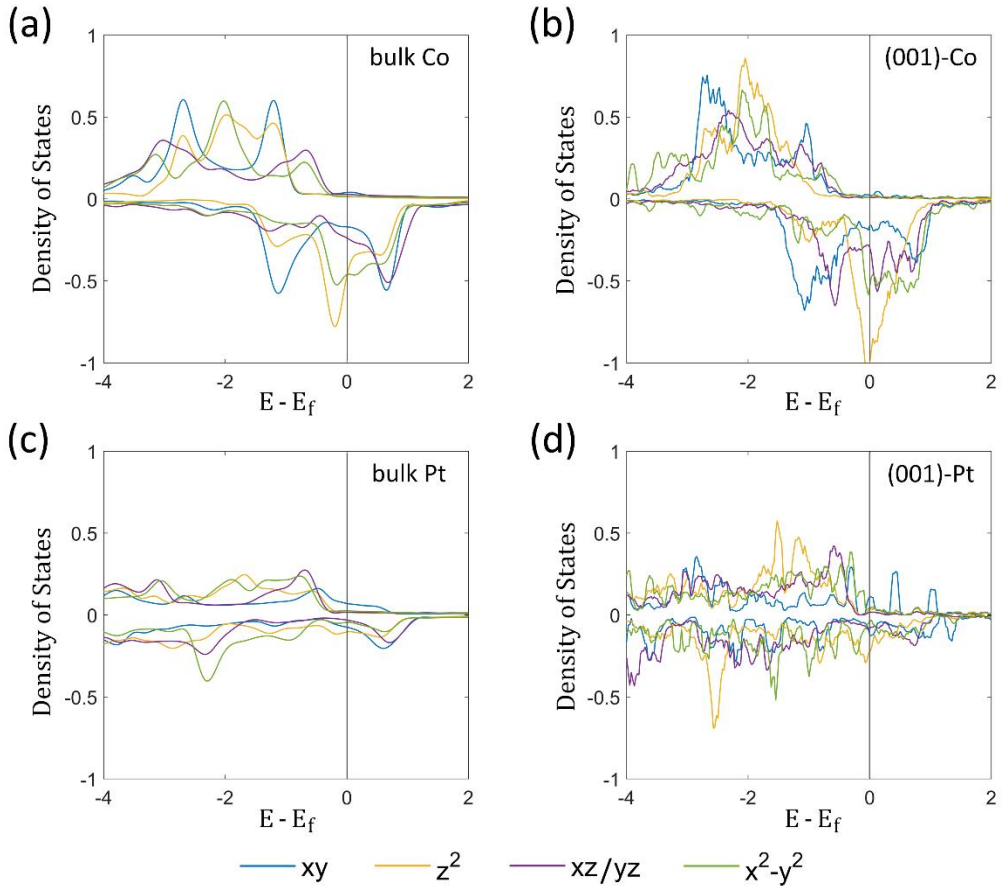

Figure 5.10 Resolved *d* orbital density of states (DOS) of (a) Co atoms in L1$_0$ CoPt crystal, (b) Co atoms in the outermost layer of bulk-terminated (001)-Co surface of CoPt crystal, (c) Pt atoms in L1$_0$ CoPt crystal, and (d) Pt atoms in the outermost layer of bulk-terminated (001)-Pt surface of CoPt crystal.

5.2.3.2 Pt-Segregated (001) and (100) Surface

As depicted in Figure 5.9, the Pt-segregated (001) surface was attained by exchanging the positions of the outermost (whole layer) Co atoms with the second sublayer Pt atoms of the bulk-treminated (001)-Co surface. Our results in Table 5.9 indicate that this Pt surface segregation makes the value of MAE become more negative. To understand this result, we have plotted in Figure 5.11 the *d*

electron DOS of the Co and Pt atoms in the outermost two layers of the bulk-treminated (001)-Co and Pt-segreagted (001) surfaces. It can be seen in Figure 5.11 that, near the Fermi level, the most signifincat change in the *d* electron densities is the redcution of d_{z^2} states with minority spin for the Co atoms segregated from the outermost layer to the second sublayer. Following our discusion above (equation 5.2), we thus attribute the more negative MAE value of the Pt-segreagted (001) with respect to that of the bulk-treminated (001)-Co to the decrease of d_{z^2} states with minority spin for the segreagted Co atoms.

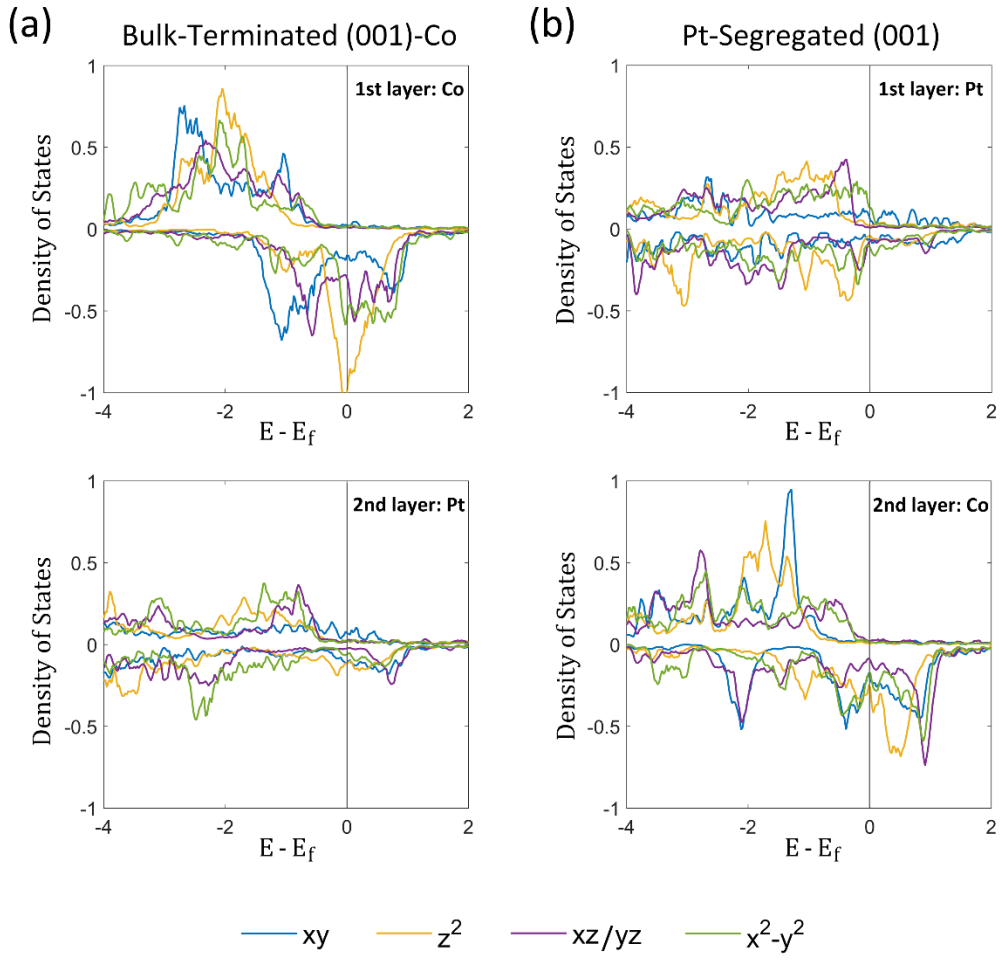

Figure 5.11 Resolved *d* orbital density of states (DOS) of the Co and Pt atoms in the outermost two layers of (a) bulk-terminated (001)-Co surface, and (b) the corresponding Pt-segregated (001) surface of $L1_0$ CoPt crystal.

To further confirm this finding, we plot the orbital resolved *d* electron DOS of the Co atoms in the bulk-terminated and Pt-segregated (100) surfaces in Figure 5.12. In the bulk-terminated (100) surface of CoPt crystal, each surface layer contains 50 at.% of Co atoms and 50 at.% of Pt atoms. Consequently, there are Co atoms in both the outermost and subsurface layers. In contrast, there are no Co atoms in the outermost layer of the Pt-segregated (100) surface. Moreover, the Co atoms in the subsurface layer of the Pt-segregated (100) surface consist of those Co atoms originally at a Co sub lattice site (denoted as Co_{Co}) and those Co atoms segregated to a Pt sub lattice site (denoted as Co_{Pt}) from the outermost layer. Our results in Figure 5.12 show that the *d* electron DOS near the Fermi level of the Co atoms in the subsurface layer of the Pt-segregated (100) are nearly identical to that of the Co atoms in the subsurface layer of the bulk-terminated (100), but differ from that of the Co atoms in the outermost layer of the bulk-terminated (100) mainly in the d_{z^2} states with minority spin. Here, we observe again that the segregated Co atoms in the Pt-segregated (100) surface have a decreased density of d_{z^2} states with minority spin as comparted to the Co atoms in the outermost layer of the bulk-terminated (100) surface. Consequently, our computational results suggest that the decrease in d_{z^2} states with minority spin for the Co atoms segregated from the outermost layer to the subsurface layer could be a primary reason for the observed trend in Table 5.9 that the Pt surface segregation in the $L1_0$ CoPt surfaces leads to a negative contribution to their MAE values as compared to the bulk-terminated surfaces. Here, for simple illustration of principles, we discuss only how the change in the d_{z^2} states would affect the MAE values of the CoPt surfaces. Our present study does not exclude the possibility that the other changes in the electronic structures (shown in Figure 5.12) might also contribute considerably to the difference between the MAE values of the bulk-terminated and Pt-segregated surfaces.

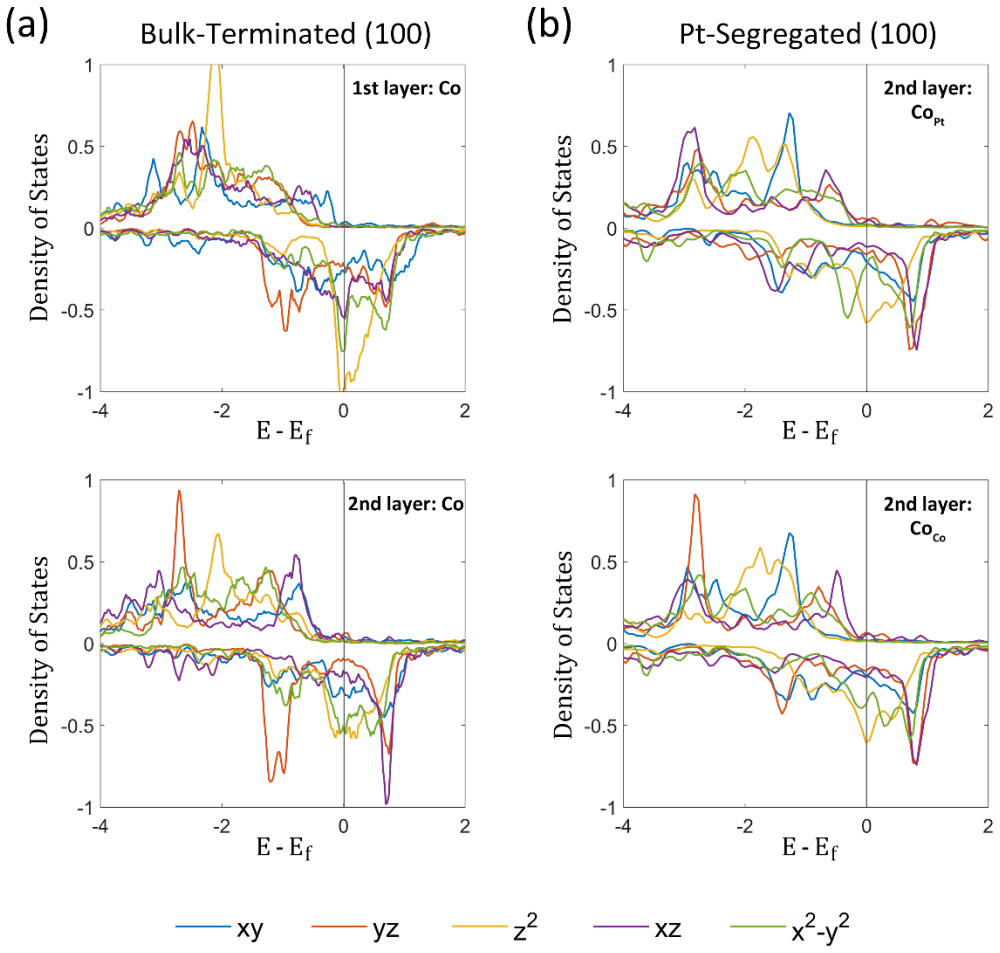

Figure 5.12 Resolved *d* orbital density of states (DOS) of the Co atoms (a) in the outermost and subsurface layer of bulk-terminated (100) surface, and (b) in the subsurface layer of Pt-segregated (100) surface of $L1_0$ CoPt crystal.

5.3 SHAPE EFFECT ON THE MAGNETIC PROPERTIES OF COPT AND FEPT NANOPARTICLES

5.3.1 Shape-dependent magnetic properties

As shown in Figure 5.13, we predicted the magnetic properties of the CoPt and FePt nanoparticles containing 55 atoms (31 Pt atoms and 24 Co (or Fe) atoms), with a diameter of about 1.1 nm, and with three different (cuboctahedral (CO), decahedral (Dh), and icosahedral (Ih)) shapes using the DFT computational method. The cuboctahedral nanoparticle is truncated from $L1_0$ crystal by six (001)/(100) facets and eight (111) facets. The decahedral nanoparticle is comprised of five structural domains which are exposed by (111) and (001) facets and intersect at a five-fold symmetry axis through twin interface. The icosahedral nanoparticle is composed of twenty twin-related tetrahedra packed along (111) interfaces. In its high-symmetric form, the cuboctahedral nanoparticle has one four-fold rotational axis (i.e., c-axis of $L1_0$ crystal, shown by the dashed line in Figure 5.13(a)) and two four-fold rotational axes which are normal to the c-axis of $L1_0$ crystal, the decahedral nanoparticle has a two-fold rotational axis (shown by the dashed line in Figure 5.13(b)) and one five-fold rotational axis normal to this two-fold rotational axis, and the icosahedral nanoparticle has three two-fold rotational axes perpendicular to each other: one is shown by the dashed line in Figure 5.13(c), and other two are normal to it. From our non-collinear magnetism calculations, we found that the CoPt and FePt nanoparticles would have relative lower energy when magnetized along the axis as depicted in Figure 5.13 (i.e., normal to the layers alternatively composed of pure Pt and pure Co (or Fe)) than along those directions normal to these axes. Specifically, our DFT results predict such a magnetic anisotropy energy to be 0.30, 1.24, and

1.84 meV/atom for the CO, Dh, and Ih CoPt nanoparticles, and 1.06, 0.84, and 1.79 meV/atom for the CO, Dh, and Ih FePt nanoparticles, respectively.

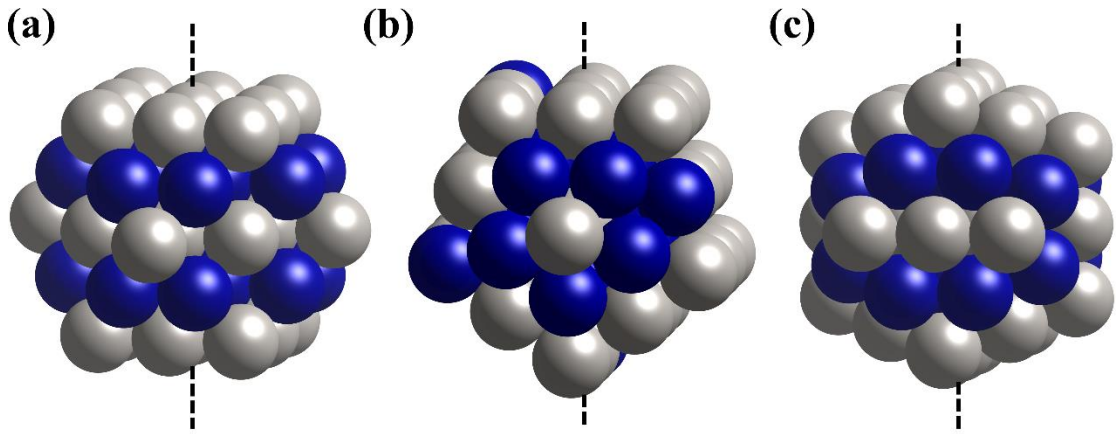

Figure 5.13 Atomistic structures of (a) cuboctahedral, (b) decahedral and (c) icosahedral nanoparticles. In the figure, the gray balls represent Pt atoms and the blue balls represent Co or Fe atoms. The dashed line indicates a four-fold axis of a cuboctahedral particle, a two-fold axis of a decahedral particle, and a two-fold axis of an icosahedral particle.

In Table 5.10, we compare the predicted energetic and magnetic properties of the CoPt and FePt nanoparticles with three different (i.e., CO, Dh and Ih) shapes from both our collinear and non-collinear magnetism DFT calculations. In consistent with previous theoretical predictions [19], our results indicate that the multiply-twinned Dh and Ih nanoparticles all have lowered energies than the $L1_0$ cuboctahedral nanoparticles, and the Ih is the most stable morphology among the three shapes for the CoPt and FePt particles with 55 atoms. Moreover, we found that the non-collinear magnetism with SOC effect gave the exactly same trend about the total energies of the CoPt and FePt nanoparticles. It should be noted that the magnetization axes of the nanoparticles

were chosen to align along the axes (show in Figure 5.13) perpendicular to the Co(Fe)/Pt alternating layers in our non-collinear magnetism calculations presented in Table 5.10.

Table 5.10 Calculated energetic and magnetic properties of CoPt and FePt nanoparticles with different (CO, Dh, and Ih) shapes. Nanoparticle energy is given in term of the energy (ΔE) relative to that of the CO nanoparticle. The presented magnetic properties include the spin magnetic moment (μ_S) and maximum surface canting angle (ϕ_{max}).

	CoPt			FePt		
	CO	Dh	Ih	CO	Dh	Ih
ΔE [a] (meV/atom)	0.0	-39.3	-44.8	0.0	-19.0	-48.2
ΔE [b] (meV/atom)	0.0	-38.8	-49.0	0.0	-20.7	-53.2
μ_S [a] (μ_B/atom)	1.14	1.09	1.16	1.65	1.55	1.67
μ_S [b] (μ_B/atom)	1.11	1.07	1.14	1.52	1.54	1.64
ϕ_{max} [b] (°)	4	12	5	22	12	6

[a] Collinear spin-polarized calculation

[b] Non-collinear magnetism including spin-orbital coupling calculation

Our collinear magnetism DFT results in Table 5.10 also indicate that the spin magnetic moments of the CoPt and FePt nanoparticles exhibit clear dependency on their shapes. Among the three types of the nanoparticles investigated, the Ih particle was found to possess the highest spin magnetic moment whereas the Dh particle had the lowest spin magnetic moment for both CoPt and FePt alloys. In this regard, our non-collinear magnetism DFT calculations gave the same trend for the three CoPt nanoparticles but predicted for the FePt nanoparticles that the spin magnetic moment of the CO particle would be lower than that of the Dh particle. As compared to the collinear magnetism DFT method, the non-collinear magnetism DFT calculation allows both the

magnitude and the direction of magnetic moment vectors to be optimized with reference to a given magnetization direction and thus take spin canting effect (i.e. the direction of magnetic moment deviates from the magnetization direction) into accounts. The effect of the spin canting effect could be gauged using the deviation angle between the direction of local magnetic moment and the given magnetization direction. We present the maximum spin canting angles found in the CoPt and FePt nanoparticles. It is noticeable that all the nanoparticles exhibit appreciable degrees of spin canting. This explains why all the spin magnetic moments of the nanoparticles predicted from the non-collinear magnetism DFT calculations are lower than those from the collinear magnetism DFT calculations. More importantly, our non-collinear magnetism DFT calculations for the FePt nanoparticle with CO shape predicted a maximum canting angle to be 22°, which is about two times larger than that of the Dh particle. Owing to such a strong spin canting effect, the spin magnetic moment of the FePt nanoparticle with CO shape becomes even lower than that with Dh shape in our non-collinear magnetism DFT calculations. Here, our DFT results suggest that the non-collinear spin canting phenomenon could affect remarkably the magnetic properties of small magnetic nanoparticles. Nevertheless, the physical mechanisms underlying the observed shape-dependent spin magnetic moments of the CoPt and FePt nanoparticles should be elaborated even within the collinear magnetism theory.

5.3.2 Shape-dependent surface magnetism

In a first step, we investigated how the shapes affected the variation of atomic spin magnetic moments in the CoPt and FePt nanoparticles. To this end, we performed Bader analysis [150] to evaluate the charge and net spin of the individual atoms, which are confined by the zero-flux surfaces having zero charge density gradient along their normal direction. Specifically, for the 55-

atom CO, Dh and Ih nanoparticles, the inner 13 atoms have complete shell of twelve nearest neighbors and constitute a core with the same symmetry of the overall shape, whereas the other 42 atoms lie on the surface layer. Both the CO and Ih nanoparticles have a core consisting of eight Co (or Fe) and five Pt atoms. In contrast, the core of the Dh nanoparticles contains ten Co (or Fe) and three Pt atoms.

Our DFT calculations predict that the core Pt atoms have an average spin moment of $0.40\mu_B$, $0.48\mu_B$, and $0.46\mu_B$ in the CO, Dh, and Ih nanoparticles of CoPt, $0.44\mu_B$, $0.49\mu_B$, and $0.48\mu_B$ in the CO, Dh, and Ih nanoparticles of FePt, whereas the core Co atoms have an average spin moment of $1.99\mu_B$, $2.01\mu_B$, and $2.04\mu_B$ in the CO, Dh, and Ih nanoparticles of CoPt, the core Fe atoms have an average spin moment of $3.00\mu_B$, $2.95\mu_B$, and $3.00\mu_B$ in the CO, Dh, and Ih nanoparticles of FePt, respectively. Hence, our results show that the core of the Ih nanoparticles possesses clearly higher magnetic moment than that of the CO nanoparticles, although the cores of the Ih and Co nanoparticles have the same chemical composition for both CoPt and FePt.

Moreover, our DFT results indicate that, for both the CO and Ih nanoparticles, the outer surface atoms normally possess magnetic moments higher than that of the inner core atoms. In average, each surface Co atom is predicted to have a magnetic moment about $0.08\mu_B$ and $0.04\mu_B$ higher than the corresponding core Co atoms in the CO and Ih nanoparticles of CoPt, respectively; each surface Fe atom is predicted to have a magnetic moment about $0.23\mu_B$ and $0.26\mu_B$ higher than the corresponding core Fe atoms in the CO and Ih nanoparticles of FePt, respectively. This trend is in general consistent with previous predictions for pure Co and Fe nanoparticles [151]. However, our DFT results indicate that, for the Dh nanoparticles, the average magnetic moment of the surface atoms could be smaller than that of the core atoms. The most prominent change is that each surface Pt atom has an average magnetic moment about $0.10\mu_B$ and $0.09\mu_B$ lower than

the corresponding core Pt atoms in the Dh nanoparticles of CoPt and FePt, respectively. These results suggest that enhanced surface magnetism of the CO and Ih nanoparticles underlies the predictions in Table 5.10 that the CO and Ih nanoparticles have larger magnetic moments than the Dh nanoparticles for both CoPt and FePt alloys.

The surface magnetism of nanoparticles is believed to mainly stem from the broken-symmetry of the surface atoms, which have reduced coordinated numbers and thus enhanced imbalance between majority and minority spins [29]. Indeed, previous studies showed a correlation between the magnetic moment and coordination number of the surface atoms in pure metal nanoparticles. For instance, an experimental measurement on the surface-enhanced magnetism of Ni clusters revealed that the clusters with open geometrical shells had larger magnetic moment per atom than the closed-shell clusters [152]. Moreover, a DFT study on Co nanoparticles showed that the local magnetic moment increased its value when the coordination number of the Co atoms decreased [153]. However, we did not observe a clear correlation between the magnetic moment and coordination number of the surface atoms in our alloy nanoparticles in this study. For the 55-atom nanoparticles studies here, the average coordination number of the surface atoms is 6.57, 6.71, and 7.43 for the CO, Dh, and Ih shapes, respectively. Our results in Table 5.10 indicate that the Ih nanoparticles have a relatively large averaged surface coordination number but exhibit the highest average magnetic moment among the three shapes, inconsistent to the trend observed in pure metal clusters. Instead of coordination number, we did identify a correlation between the magnetic moment and atomic spacing of the surface atoms in our alloy nanoparticles in this study. Our structural analysis shows that the distance between a surface atom and its first-nearest neighbors in the surface of the three alloy nanoparticles normally become shorter than the corresponding separation of adjacent Pt-Pt, Pt-Co (or Pt-Fe), and Co-Co (or Fe-Fe) pairs in

reference $L1_0$ bulk crystal. In average, this contraction of the atomic spacing for the surface atoms is 3.35%, 3.57%, and 0.18% in the CO, Dh, and Ih CoPt nanoparticles, and 3.04%, 3.53%, and 0.27% in the CO, Dh, and Ih FePt nanoparticles, respectively. Consequently, our calculation results suggest that the magnetic moment would increase its value when atomic spacing of the surface atoms increases in the CoPt and FePt nanoparticles. Namely, the Ih nanoparticle with the smallest atomic spacing contraction is found to have the highest magnetic moment whereas the Dh nanoparticle with the largest atomic spacing contraction is predicted to have the lowest magnetic moment. It appears that our finding could be rationalized in terms of the strain effect on the magnetic moment that an increase in atomic spacing leads to band splitting and hence enhanced magnetic moment [29].

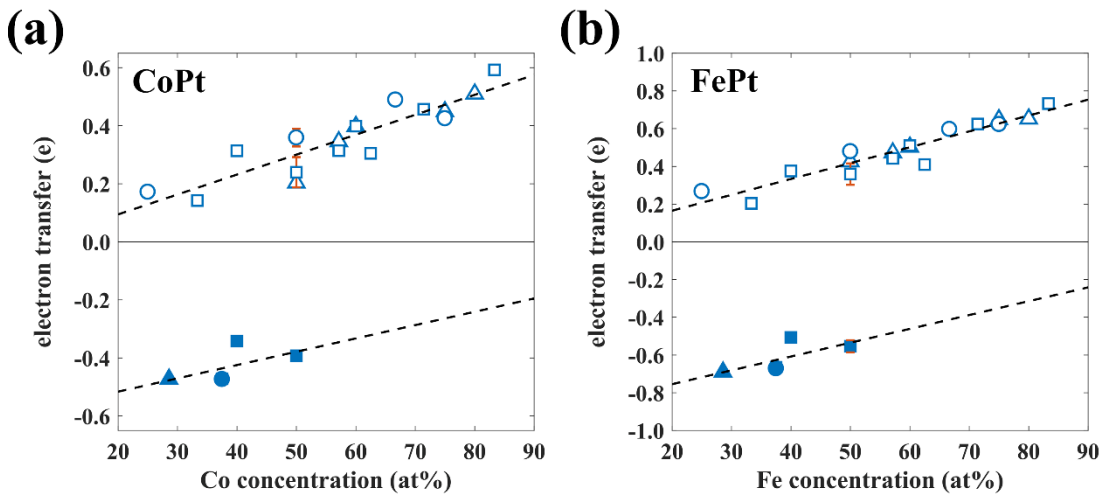

Figure 5.14 Predicted variation of the electron gain on the 5*d* Pt atoms (open symbols) as well as the electron loss on the 3*d* Co and Fe atoms (filled symbols) in the surface of (a) CoPt and (b) FePt nanoparticles as a function of their local chemical composition. In this figure, the triangles, squares, and circles represent the data for the CO, Dh, and Ih nanoparticles, respectively. The dashed lines are linear fitting of the data.

The surface magnetism is also strongly influenced by the local chemical environment in alloy nanostructures [88,154-156]. This is particularly important for the magnetism of CoPt and FePt alloys, since the magnetic moment of Pt atoms is believed to be a result of the charge transfer from neighboring 3*d* transition metals (Co or Fe) [157]. Therefore, we plot the variation of the electron gain of the surface Pt atoms as well as the electron loss of the surface Co (or Fe) atoms as a function of the Co (or Fe) concentration around these atoms in Figure 5.14 (a) and (b). The electron transfers of individual atoms in the nanoparticles were determined by comparing their Bader electron density with that of neutral atoms. Our results (Figure 5.14) show that there exists a proportionally linear relation between the electron transfer and local Co (or Fe) concentration for the CoPt (or FePt) nanoparticles. In particular, we computed the average electron loss of the surface 3*d* transition metal atoms in the nanoparticles to be 0.47e, 0.41e, and 0.47e for Co atoms in the CO, Dh, and Ih CoPt nanoparticles, and 0.71e, 0.64e, and 0.69e for Fe atoms in the CO, Dh, and Ih FePt nanoparticles, respectively. Hence, our DFT calculation results suggest that the electron transfer in the surface atoms is related to the local chemical concentration and varies with a change of the nanoparticle shape. Among the three nanoparticle shapes investigated, the surface Co (or Fe) atoms in the Dh nanoparticle has the highest local Co (or Fe) concentration and resultantly the smallest electron loss to the surface Pt atoms.

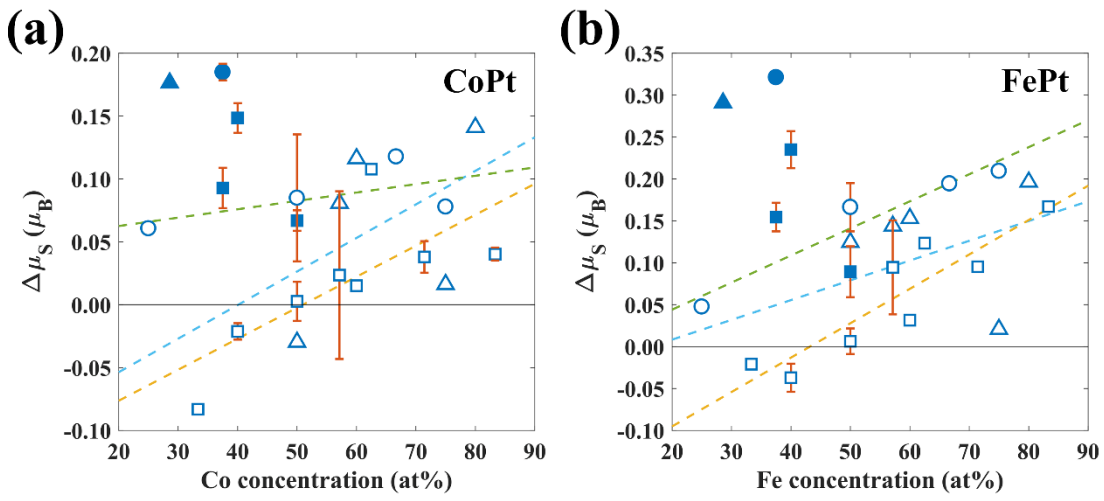

Figure 5.15 Predicted magnetic moment change ($\Delta\mu_S$, relative to the corresponding values in bulk crystal) of the surface Pt (open symbols), Co (filled symbols), and Fe atoms (filled symbols) in the (a) CoPt and (b) FePt nanoparticles as plotted against their local chemical composition. In this figure, the triangles, squares, and circles represent the data for the CO, Dh, and Ih nanoparticles, respectively. The dashed lines are used to guide the eyes for the magnetic moment changes of the surface Pt atoms in the Ih (green), CO (cyan), and Dh (orange) nanoparticles.

Hence, we have just identified that both the geometric factor (atomic spacing contraction) and chemical factor (local 3*d* transition metal concentration) are related to the shape-dependent surface magnetism of the CoPt and FePt nanoparticles. To illustrate this point, we plot in Figure 5.15 the change of the atomic magnetic moments (with respect to bulk values) in the nanoparticle surfaces as a function of local chemical composition. It can be seen that the magnetic moment of the surface Co (and Fe) atoms decreases with an increase in the local Co (and Fe) concentration. As a result, the surface Co (and Fe) atoms in the Dh nanoparticles have the lowest magnetic moments among the three different shapes of the nanoparticles. In addition, our results in Figure

5.15 show that the magnetic moments of the surface 5*d* Pt atoms exhibits increase with increasing local 3*d* Co (and Fe) concentration. This result implies that enhanced hybridization of 3*d*-5*d* electronic orbitals would induce higher magnetic moments on the surface Pt atoms. It is also noticeable in Figure 5.15 that the magnetic moments of the surface Pt atoms in the Dh nanoparticles are consistently lower than those in the Ih and Co nanoparticles. We believe that the larger contraction of atomic spacing in the Dh nanoparticle surface is responsible for this observed discrepancy.

5.3.3 Surface spin canting of cuboctahedral CoPt and FePt nanoparticles

Comparing the predicted magnetic moments in Table 5.10, we found that the predictions from the non-collinear magnetism calculations were always lower than those from the collinear magnetism calculations. We attributed this discrepancy to the surface spin canting in the CoPt and FePt nanoparticles under the non-collinear magnetism with spin-orbital coupling. In particular, we noticed that the surface spin canting caused a reduction of 0.03 μ_B per atom in the CoPt nanoparticle with the CO shape whereas much larger reduction of 0.13 μ_B per atom in the FePt nanoparticle with the CO shape.

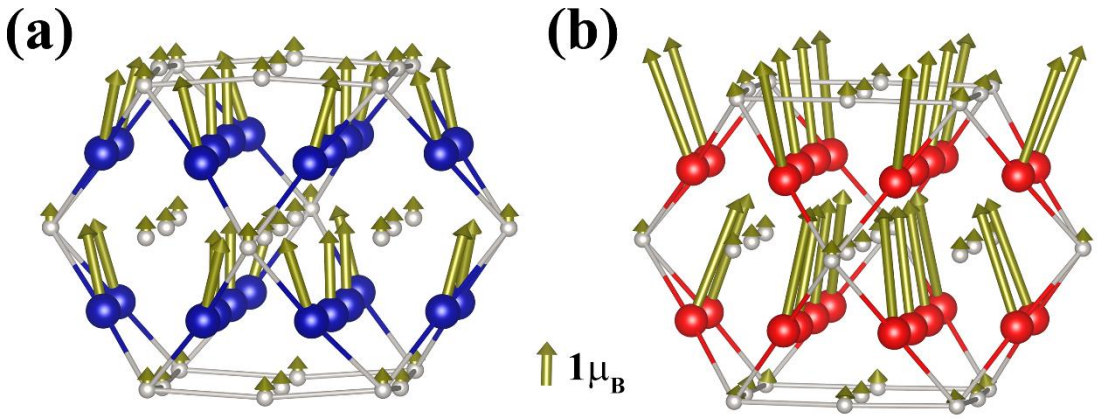

Figure 5.16 Surface magnetic configuration of the 55-atom cuboctahedral (a) CoPt and (b) FePt nanoparticle under vertically upward (i.e., [001] direction) magnetization predicted by the noncollinear magnetism DFT calculations. In the figure, the blue balls represent Co atoms, the gray balls represent Pt atoms, the red balls represent Fe atoms, and the golden arrows represent the atomic magnetic moment changes at each atom with respect to the corresponding bulk magnetic moment of the same element.

To understand this discrepancy, we plot in Figure 5.16 the configuration of spin canting on the surface of the CO nanoparticles. In both CoPt and FePt nanoparticles, the extent of the surface spin canting is predicted to be more pronounced on the surface 3*d* Co and Fe atoms than on the 5*d* Pt atoms. However, our DFT study reveals that the CoPt and FePt nanoparticles manifest dramatically different fashions of surface spin canting, as depicted comparatively in Figure 5.16 for the CO CoPt and FePt nanoparticles under [001] magnetization. Figure 5.16(a) shows that the local magnetic moments of the surface atoms in the bottom half of the CoPt particle are predicted to rotate outwardly whereas those of the surface atoms in the top half of the CoPt particle rotate inwardly with respect to the [001] axis. This configuration is consistent with the so-called

"artichoke" magnetic configuration [128]. Exactly opposite, our DFT results in Figure 5.16(b) indicate that the local magnetic moments of the surface atoms in the bottom half of the FePt particle will rotate inwardly and in the top half of the FePt particle will rotate outwardly with respect to the [001] axis. This configuration is consistent with the so-called "throttled" magnetic configuration [128]. It should be noted that we exaggerate the spin canting angles in Figure 5.16(a) of the CoPt nanoparticles for the purpose of illustration. As reported in Table 5.10, the maximum spin canting angle of the surface Co atoms is merely 4°.

To explain the observed spin canting fashion, in this study, we performed the non-collinear DFT calculations and evaluated the surface anisotropy energy for the extended (100), (001) and (111) surfaces of CoPt and FePt crystal. It notes that these three low-index surfaces are the exposed facets of the CO nanoparticles. We modeled the (100) and (111) surfaces using eight-atomic-layer slabs and the (001) surfaces (i.e., Pt termination and Co (or Fe) termination) using nine-atomic-layer slabs. The magnetic anisotropy energy of the modelled slab was determined as the energy difference between the magnetization in the direction normal and parallel to the surface. Hence, the surface anisotropy energy (ΔE_S) was further calculated as the magnetic anisotropy energy difference per surface formula unit (one CoPt or FePt) between the modeled slab and bulk crystal. For the (001) surface, we calculated the average ΔE_S over the Pt-terminated and Co (or Fe)-terminated slabs. Our DFT calculations predict that the values of ΔE_S are 1.58, 0.86, and 0.17 meV for the CoPt (100), (001) and (111) surfaces, whereas -2.24, -0.55, and 0.34 meV for the FePt (100), (001) and (111) surfaces, respectively.

Consequently, we predict that the (100), (001) and (111) surfaces of $L1_0$ CoPt crystal all have positive ΔE_S and hence prefer an in-plane magnetization more than an out-of-plane magnetization. This explains well why an "artichoke" spin structure was found in Figure 5.16(a)

for the 55-atom CO nanoparticle of CoPt. Moreover, we predict that the (100) and (001) surfaces of $L1_0$ FePt crystal have negative ΔE_S and hence prefer an out-of-plane magnetization more than an in-plane magnetization. It appears that these surfaces with negative ΔE_S lead to the observed "throttled" spin structure of the in Figure 5.16(b) for the 55-atom CO nanoparticle of FePt, even though the FePt (111) surface has a positive ΔE_S. Therefore, our DFT calculation results confirmed well that the surface anisotropy energy underpins the spin structure of magnetic nanostructures.

5.4 NÉEL ANISOTROPY AND MAGNETOELASTIC PROPERTIES

5.4.1 Micromagnetic simulation

Both CoPt and FePt crystal have the same $L1_0$ lattice structure and exhibit similar uniaxial anisotropy with [001] as their easy magnetization axis. However, our DFT study revealed that bulk-terminated CoPt and FePt nanoparticles manifest different fashions of surface spin canting. To gain insights into the observed different fashions of surface spin canting in the CoPt and FePt nanoparticles, we have performed micromagnetic simulations for a cuboctahedral nanoparticle containing 1289 atoms. For simplicity, we assume that the local magnetic moments are continuous variables in direction with a fixed unit magnitude, the nanoparticle has a face centered cubic lattice structure, and the surface spin canting of the particle is mainly attributed to Néel's surface anisotropy. Hence, the total energy of the magnetic particle is expressed as

$$H = -J \sum \overrightarrow{S_i} \overrightarrow{S_j} - K_S \sum \left(\overrightarrow{S_i} \cdot \overrightarrow{e_{ij}} \right)^2 \tag{5.4}$$

where J is the exchange interaction constant (in this work, we set the value of J as 18.7meV), $\overrightarrow{S_i}$ and $\overrightarrow{S_j}$ are the magnetic moments on nearest neighboring atoms i and j, K_S is the Néel's surface anisotropy constant, and $\overrightarrow{e_{ij}}$ is the unit position vector from atoms i to atom j. In equation 5.4, the first term is the energy contribution from exchange interaction and the second term is the energy contribution from Néel's surface anisotropy.

In this work, the equilibrium magnetic configuration of the cuboctahedral nanoparticle at low temperature was derived through a simulated annealing process. Initially, we set the simulation temperature as 800 K at which the nanoparticle was predicted to adopt a paramagnetic state (random distribution of local magnetic moments) based on our value of J. Starting form this initial magnetic configuration, we used the constrained Monte Carlo (MC) simulation method based on the Metropolis algorithm to relax the magnetic configuration of the nanoparticle at gradually decreasing temperatures. In our simulations, we decreased the temperature by 50 K after each MC relaxation and run 400,000 MC steps at each simulation temperature, until the temperature is reduced down to 50K.

Figure 5.17 shows the cross-sectional view of the simulated equilibrium magnetic configuration of a magnetic cuboctahedral particle at 50K. The magnetization direction is constrained to be aligned along [001] direction. Our micromagnetic simulation predicts that the rotations of local magnetic moment agree well with those in the CoPt nanoparticle (Figure 5.16(a)) if the Néel's surface anisotropic constant K_S is positive (Figure 5.17(a)), whereas agree well with those in the FePt nanoparticle (Figure 5.16(b)) if the Néel's surface anisotropic constant K_S is negative (Figure 5.17(b)). Our results are consistent with previous micromagnetic simulation on spherical nanoparticles [96,128,158]. Therefore, the different fashions of surface spin canting could be reproduced by a simple parameter Néel's constant. This parameter could be calculated

ab initio and provide more physical insights on the magnetic behavior in the $L1_0$ CoPt and FePt nanoparticles.

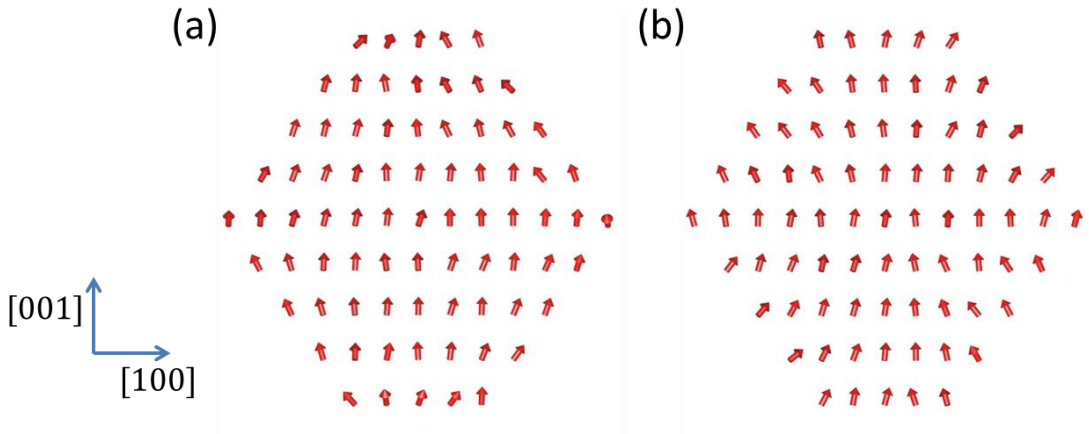

Figure 5.17 Micromagnetic constrained Monte Carlo simulation of a cuboctahedral nanoparticle with 1289 atoms. The figure shows the cross-section of center (010) plane with (a) positive (K_S=+2J) and (b) negative (K_S= -2J) Néel's surface anisotropic constant L in equation 5.4. The red arrows represent the local magnetic moments.

5.4.2 Magnetoelastic coupling of bulk CoPt and FePt

As was introduced in 4.2, magnetoelastic coupling describes the interaction between magnetic polarization and the lattice deformation. The magnetoelastic behavior of magnets is important not only in the fundamental science but also in the practical application such as magnetic sensors and actuators [159,160]. The presence of magnetoelastic energy could change the spin configuration and anisotropy direction and anisotropy magnitude in magnetic materials. For example, the magnetoelastic energy is believed to be one of the driving force that transforms the helical

magnetic structure to ferro-cone phase in rare earth element Ho system [161]. The enhancement of coercivity for CoPt/AlN multilayer was attributed to the in-plane stresses by the magnetoelastic effect [162]. As was described in 2.4, the magnetoelastic coupling constant is directly related to the surface anisotropy in Néel's model. Consequently, the magnetoelastic provides a bridge to the understanding of surface anisotropy in CoPt and FePt nanoparticles. To the best of our knowledge, the magnetostriction constant and magnetoelastic coupling constant for $L1_0$ CoPt and FePt have not been determined yet, neither experimentally nor theoretically. The only available value for CoPt and FePt were measured for disordered fcc phase [163-166]. Therefore, in this work, we devote to investigate the anisotropic magnetoelastic coupling constants for CoPt and FePt in tetragonal symmetry using DFT calculations.

The magnetoelastic coupling constants of bulk $L1_0$ CoPt and FePt are calculated using the expression of magnetoelastic energy subject to given strains, as was introduced in 4.2. The strained unit cells of $L1_0$ structure are schematically shown in **Figure 5.18**, where *z* direction is defined as perpendicular to the alternating planes. The magnetic anisotropy energy (MAE) is computed along various magnetization directions for these deformed structures on which different magnitude of strains is applied. According to equation 4.6, within first order expansion approximation, the MAE is proportional to the applied strains. The slope of the linear relationship is a linear function related to magnetoelastic coupling constants.

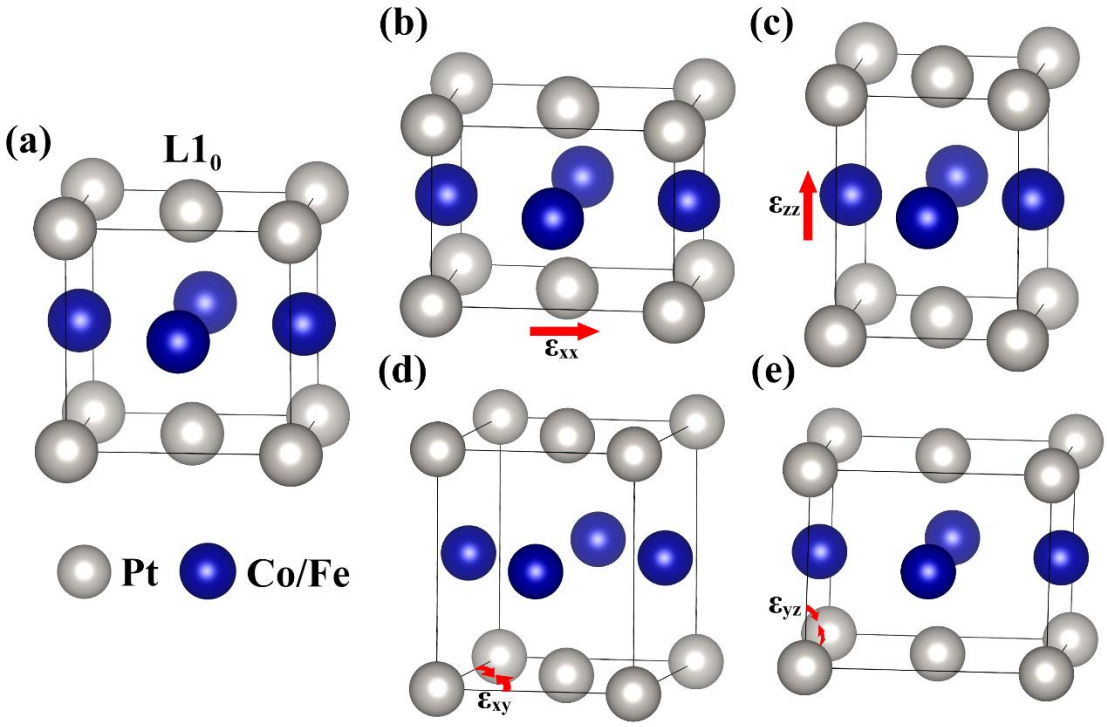

Figure 5.18 Schematic representation of tetragonal $L1_0$ structure under strain.

The calculated MAE of bulk CoPt and FePt under different types of strains are plotted in Figure 5.19-Figure 5.22. It can be seen from Figure 5.19 that under epitaxial strain ε_{xx}, the linear relationship is well preserved. The MAE drop from 1.46 (5.38) meV to 0.12 (3.62) meV when a strain of +2% is applied on CoPt (FePt), respectively, leading to a similar strength of ε_{xx} response in these two materials. Under epitaxial strain along *z* direction, the linear relationship for FePt is still preserved. However, for CoPt, a strong deviation from linearity is observed on the energy difference between the magnetization direction [100] and [010], as is shown in Figure 5.20(a). In this case, the first order expansion on the magnetoelastic energy is invalid. Higher order terms must be included to fully describe this material. The first order coupling coefficient is therefore extracted by performing quadratic fitting on the curve. The nonlinearity also occurs when shear

strain ε_{yz} is applied on CoPt, as in Figure 5.21 (a). Nonetheless, the very small value of MAE itself suggests that the calculation is approaching limit of the numerical accuracy. Meanwhile, the slight variation in MAE under shear strain results in a very weak coupling and thus a small coupling constant. Hence, the ordinary linear regression is performed in this case. Finally, under shear strain ε_{xy}, the linear response in MAE appears once again (Figure 5.22).

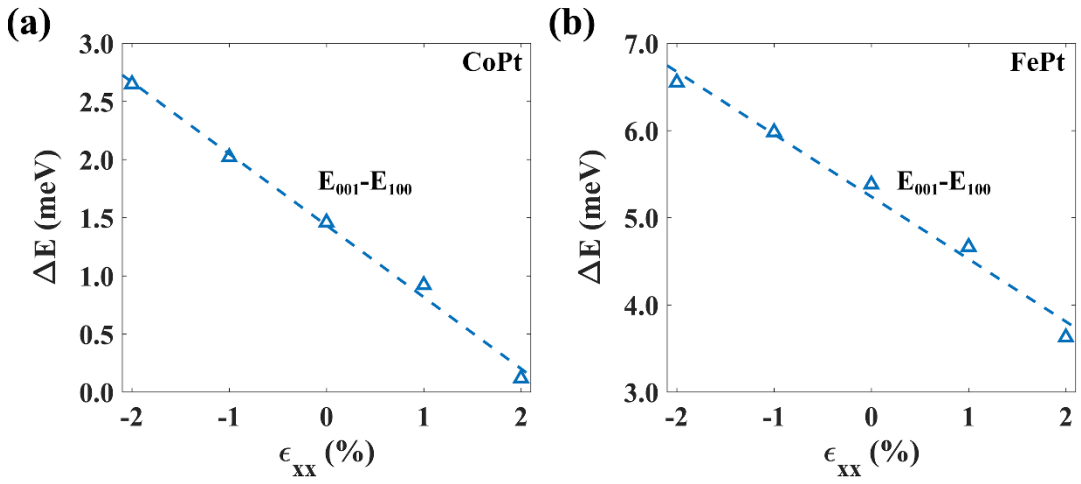

Figure 5.19 Magnetic anisotropy energy of (a) CoPt and (b) FePt under epitaxial strain along *x* direction.

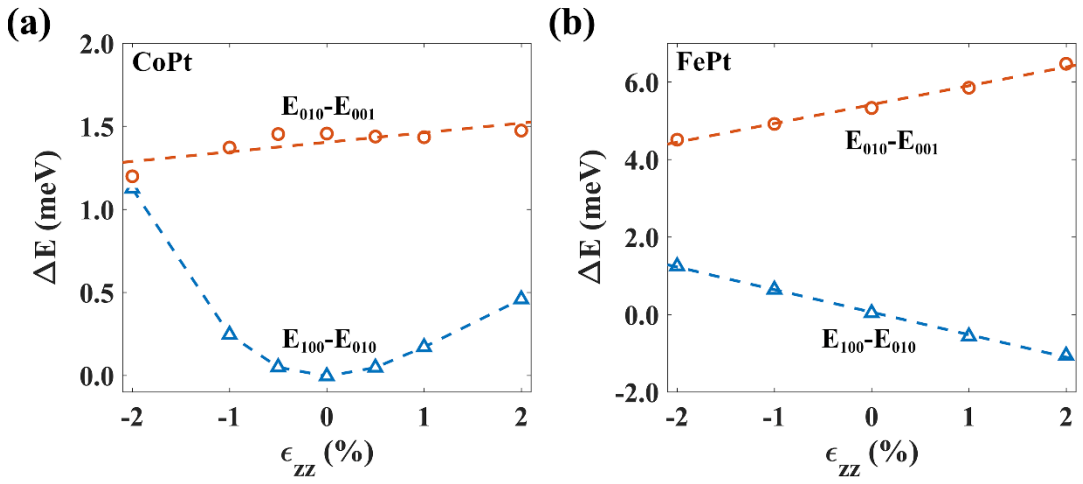

Figure 5.20 Magnetic anisotropy energy of (a) CoPt and (b) FePt under epitaxial strain along *z* direction.

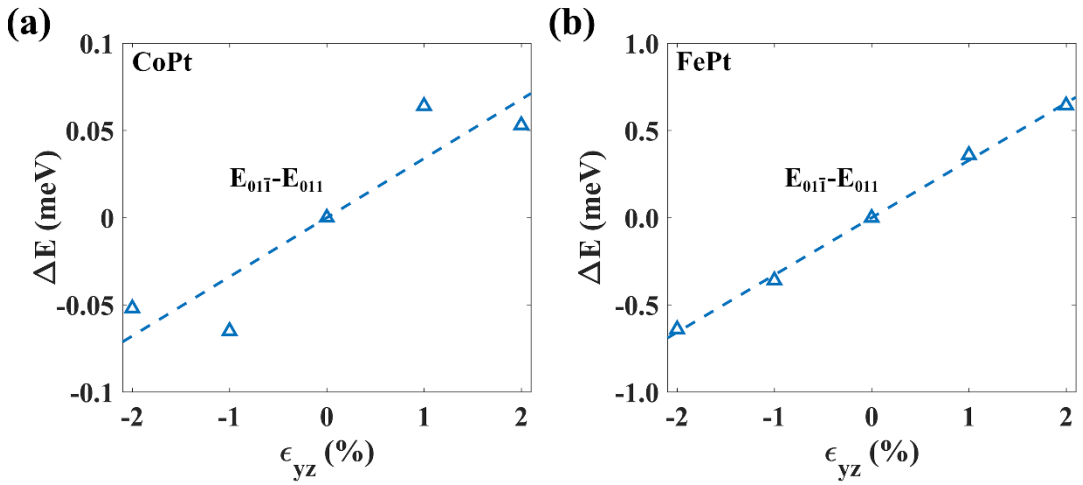

Figure 5.21 Magnetic anisotropy energy of (a) CoPt and (b) FePt under shear strain ε_{yz}.

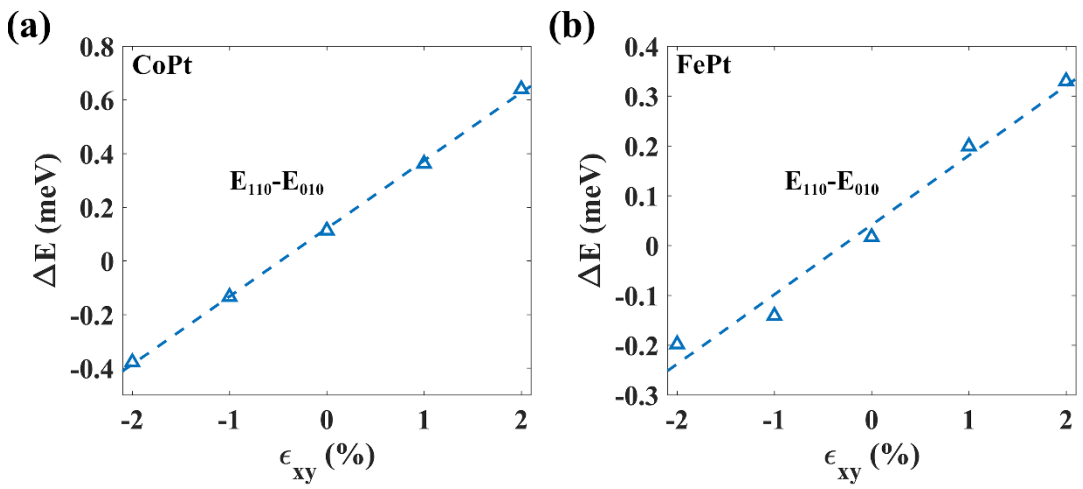

Figure 5.22 Magnetic anisotropy energy of (a) CoPt and (b) FePt under shear strain ε_{xy}.

The extracted magnetoelastic coupling constants are summarized in Table 5.11. The magnetoelastic behavior for CoPt and FePt qualitatively agrees with each other in terms of the sign of the coupling constant. According to equation 4.6, negative b_{21} and b_{22} mean that the lattice would elongate in x and z direction when the material is magnetized along z direction, while a positive b_3 suggests that the contraction along x direction is preferred under [100] magnetization. The shear strain in the direction associated with the applied magnetic field is always negative owing to the positive coupling constant $b_3^{'}$ and b_4. In general, FePt would show stronger response under the action of external magnetic field because of the relatively large magnitude of the calculated coupling constant (with the only exception of $b_3^{'}$ and the corresponding shear strain ε_{xy}).

Table 5.11 Predicted magnetoelastic coupling constant of CoPt and FePt

Magnetoelastic Constant (MPa)	b_{21}	b_{22}	b_3	b_3'	b_4
CoPt	-101.7	-20.5	4.3	149.03	10.0
FePt	-143.4	-81.0	75.7	79.	93.3

5.4.3 Néel's Anisotropy Constant of CoPt and FePt

In Néel's model, the surface anisotropy is a result of magnetostrictive pair interaction between neighboring atoms. The equations that link the Néel's constant and magnetoelastic coupling constant could be derived by equating the magnetoelastic energy f_{me} with Néel's anisotropy energy H_s under given strains. In case of cubic lattice, the volume conserved epitaxial and shear strains were considered. The two variables – Néel's constant and its derivative - are linear superposition of two magnetoelastic coupling constant (equation 2.4), neglecting the pure volume term. The breaking symmetry in $L1_0$ system produces additional degree of freedom. There are three types of interaction that corresponds to three different nearest neighbor pairs, namely Co-Co (Fe-Fe), Co-Pt (Fe-Pt) and Pt-Pt. The interaction between Co-Co (Fe-Fe) and Pt-Pt are averaged into a single parameter since their atomic positions are equivalent and indistinguishable under the applied strains. In the following paragraph, the Néel's constant describing the interaction between elements in same type is labeled as K_{S1}, while the Néel's constant describing the interaction between elements in different type is labeled as K_{S2}. K_{S1}, K_{S2} and their derivatives count for 4 independent variables in $L1_0$ lattice. On the other hand, as was already introduced and calculated in 5.4.2, five independent variables are necessary to capture the magnetoelastic coupling under external magnetic fields. The mismatch in the number of independent variables requires further assumptions or approximations. (It should be noted that more parameters could be taken into consideration for both the two models. For instance, the pair interaction between 2nd nearest neighbor provides two more terms in the expression of anisotropy energy. Higher order approximation could also be made in the sense of magnetoelastic coupling) In the current work, it is assumed that K_S captures anisotropy energy change subject to four particular volume conserved

strains, neglecting pure volume term in f_{me}. These four strains comply exactly the strains used in the calculation of magnetoelastic coupling constants.

In this scheme, the derived K_S as a function of b is expressed as a matrix equation:

$$\begin{bmatrix} 0 & -1 & -\frac{(36m^2)}{(1+m^2)^2} & -\frac{2(1-2m^2)^2}{(1+m^2)^2} \\ 3 & 0 & \frac{6m^2}{(1+m^2)^2} & \frac{3}{(m^2+1)^2} \\ 2 & 0 & \frac{2(1-2m^2)}{(1+m^2)} & \frac{8m^2}{(1+m^2)^2} \\ 0 & 2 & \frac{8}{(1+m^2)} & 0 \end{bmatrix} \begin{bmatrix} K_{S1} \\ \frac{dK_{S1}}{dr} \\ K_{S2} \\ \frac{dK_{S2}}{dr} \end{bmatrix} = \begin{bmatrix} 2b_{21} - 2b_{22} \\ 3/2\, b_3 \\ b_4 \\ b_3' \end{bmatrix} \tag{5.5}$$

where m is the lattice constant c/a ratio. The Néel's constant K_{S1} and K_{S2} are therefore determined by solving this matrix equation. The calculated results are list in Table 5.12. It can be seen that the pair interaction Co-Pt has a negative value of -3.78meV, very close to the interaction of -3.65meV between Fe and Pt atoms. However, there is an appreciable difference in the pair interaction between same elements in these two materials. FePt has a strong negative K_{S1} of -8.62meV while CoPt has a positive value of 3.42meV. The sign of these two quantities is in good agreement with the qualitative results obtained by micromagnetic simulation in 5.4.1. Using these value, the surface magnetic anisotropy energy can be calculated by summing up the nearest neighbor interaction around a surface atom. On (001) surface, the surface anisotropy energy is given by $H_s = const + 0.0103\left(\overrightarrow{S_i}\cdot\vec{n}\right)^2$ for CoPt and $H_s = const - 0.0139\left(\overrightarrow{S_i}\cdot\vec{n}\right)^2$ for FePt, where $\vec{n}$ is the unit vector normal to surface. To minimize the anisotropy energy, the local spins $\overrightarrow{S_i}$ will have a direction perpendicular to $\vec{n}$ for CoPt, while $\overrightarrow{S_i}$ tends to be parallel to the surface normal for FePt. These results perfectly explain the observed spin canting fashions from the DFT calculations on nanoparticles.

Table 5.12 Predicted Néel's constant K_{S1} and K_{S2} for CoPt and FePt

Néel constant (meV)	K_{S1}	dK_{S1}/dr	K_{S2}	dK_{S2}/dr
CoPt	3.42	-17.57	-3.78	-8.60
FePt	-8.62	-6.46	-3.65	-10.95

5.5 TAILORING THE SURFACE SEGREGATION IN COPT AND FEPT

Previous research has demonstrated that surface segregation causes the deterioration of magnetic moment and magnetic anisotropy in CoPt and FePt nanoparticles. Therefore, aiming at an enhanced magnetic performance, the approach to suppress surface segregation needs to be tested. One possible approach is to dope CoPt and FePt with a third element. Experimental results have shown that the addition of Cu, Ag and Au would promote the $L1_0$ ordering in CoPt and FePt nanoparticles [167-174]. This promotion is assumed to be also essential near surface. How the Cu, Ag and Au doping will affect the surface composition in CoPt and FePt will be investigated in this study.

5.5.1 Surface Segregation of additive Cu, Ag and Au elements

To investigate the segregation of Cu, Ag and Au, we doped the additive elements in the surface and subsurface layer of (001) and (100) surfaces in $L1_0$ ordered FePt and CoPt. Each surface structure is modeled by an 8-atomic layer slab, as shown in Figure 5.23. A vacuum region of 12Å is added above the surface to minimize the interactions between the slab and its images. For the same reason - to reduce the interaction between impurities and their periodic image, a 2×2 unit cell

which contains four atoms per layer is chosen. The substitutional dopant atom replaces the matrix element (Co/Fe and Pt) on each atomic layer. The configurations that the impurity replace internal matrix atoms (4th or 5th layer in the slab as is shown in Figure 5.23) are considered as bulk doping. The segregation energy E_{seg} is then evaluated as the energy difference of a doped slab structure relative to bulk doping.

$$E^{X}_{seg\_Co/Fe(l)} = E_{slab}\left[Co/Fe_{N-1}Pt_{N}X^{(l)}\right] - E_{slab}\left[Co/Fe_{N-1}Pt_{N}X^{(5)}\right]$$
$$E^{X}_{seg\_Pt(l)} = E_{slab}\left[Co/Fe_{N}Pt_{N-1}X^{(l)}\right] - E_{slab}\left[Co/Fe_{N}Pt_{N-1}X^{(4)}\right] \quad (5.6)$$

In this equation, $E_{slab}[\cdots X^{(l)}]$ is the energy of a slab with the impurity element *X* at *l*th layer.

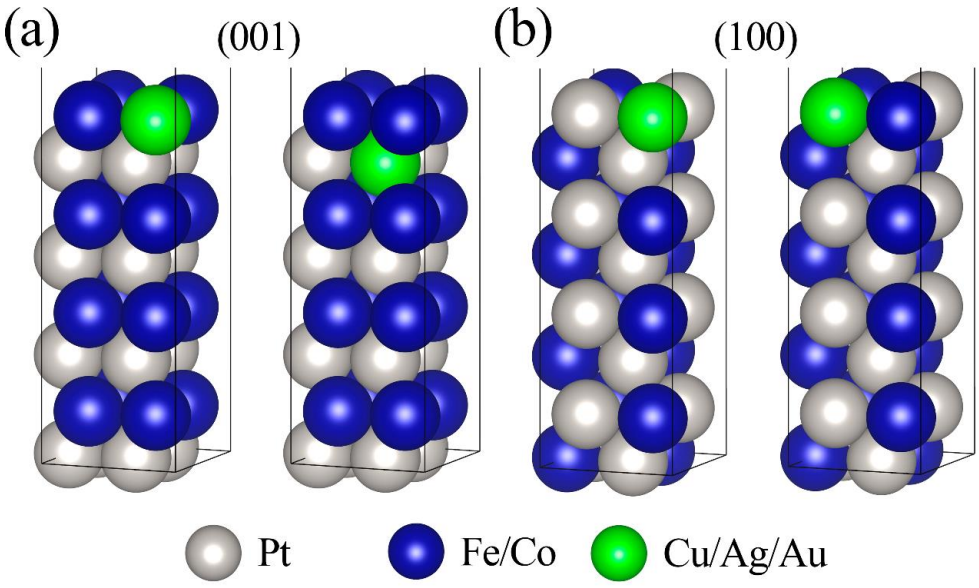

Figure 5.23 Atomistic structures of $L1_0$ CoPt/FePt (001) and (100) surfaces used to evaluate the surface segregation energies. All structures are doped with one Cu/Ag/Au atom. Various layers of substitution position are tested. Here in this figure, only one of each type (substitute Co/Fe atom and substitute Pt atom) are shown.

We plot the segregation energies (E_{seg}) of various dopant on each layer of slabs in Figure 5.24 and Figure 5.25. Layer 1 and layer 8 denotes surface layers. In asymmetric (001) slab model, top surface (layer 1) is terminated by pure Co/Fe atoms while bottom surface (layer 8) is terminated by pure Pt atoms. We therefore evaluated E_{seg} of additive atom replacing Co/Fe atoms at the top surface layers while replacing Pt atoms at bottom surface layers. In symmetric (100) slab model, each layer is composed of 50% Co/Fe and 50% Pt and the top surface is equivalent to the bottom surface. To keep the consistency, we plot in Figure 5.25 E_{seg} in the same scheme as (001) surface (additive atom replacing Co/Fe atoms at the top surface layers and replacing Pt atoms at bottom surface layers.). In all cases, a negative E_{seg} indicates the stability of additive atoms occupying surface atomic sites as compare with the bulk atomic sites.

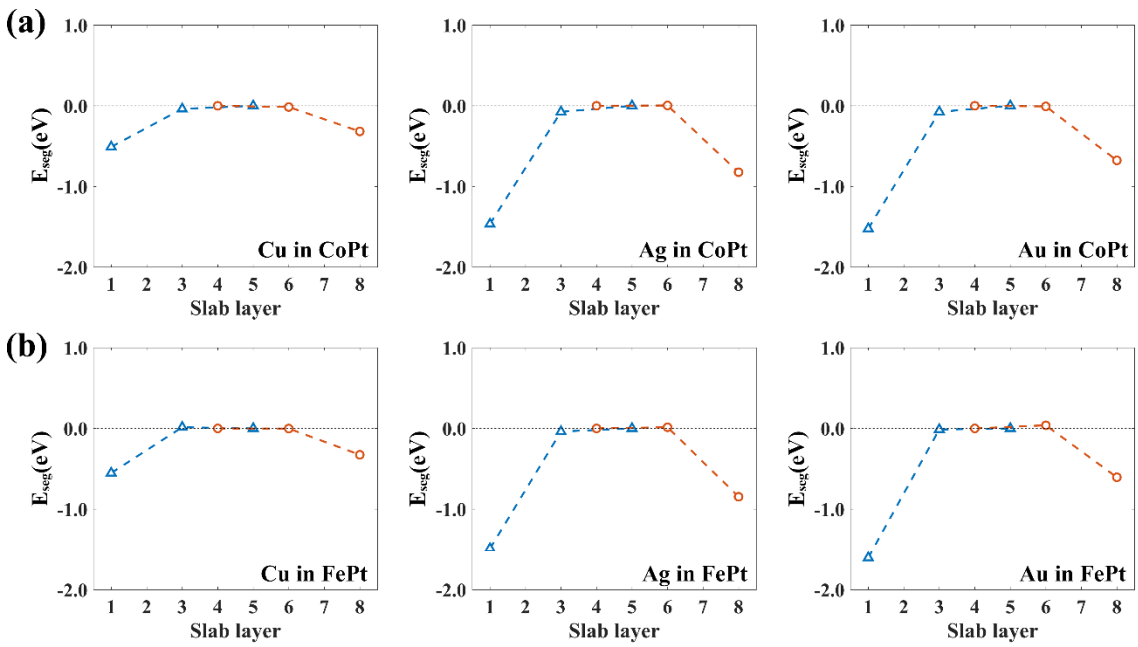

Figure 5.24 Segregation energies of Cu, Ag and Au doped (001) surface calculated using equation 5.6. The red line represents that the dopant substitutes a Pt atom. The blue line represents that the dopant substitutes a Co/Fe atom.

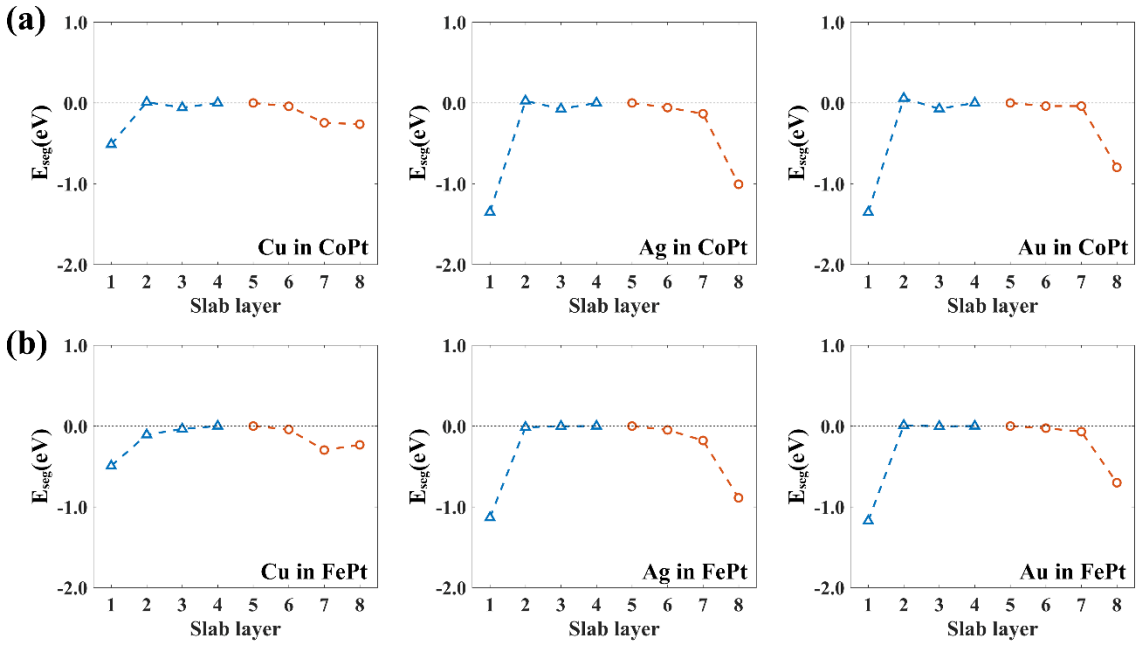

Figure 5.25 Segregation energies of Cu, Ag and Au doped (100) surface calculated using equation 5.6. The red line represents that the dopant substitutes a Pt atom. The blue line represents that the dopant substitutes a Co/Fe atom.

On (001) surface, E_{seg} is found more negative when the substitution site is closer to the surface, indicating a preference of sitting at outermost surface sites for additive Cu, Au and Ag atoms. This implies, the additive atoms have stronger tendencies to migrate to surface than not only 3*d* elements Co/Fe but also 5*d* element Pt which were found to segregate at surface in pure CoPt/FePt. Similar conclusion could be drawn on (100) surface. A strong negative E_{seg} for outermost surface layer substitution is observed for all cases investigated. It should be noted that the segregation energy of Cu substituting Pt at subsurface layer is slightly lower than substituting Pt at outermost surface layer in FePt (Figure 5.25(b)). In that case, it is more stable for Cu to sit at subsurface layer when replacing Pt atoms.

Comparing (001) surface with (100) surface, our results show that Ag and Au doping on (001) is more energetically favorable when replacing Co/Fe atoms, whereas doping on (100) is more energetically favorable when replacing Pt atoms. Contrarily for Cu substitutional solute, the Fe site and Pt site are preferable on (001) surface than on (100) surface and the Co site on (100) surface is more favorable.

As was introduced in 2.3, the surface segregation process in alloy systems is mainly governed by the three aspects: (1) heat of the solution; (2) atomic size; and (3) surface energy will segregate. Through first principles calculations, the additive elements were predicted to have lower surface energies as compare to the matrix elements (Table 5.13) [175], implying a potential tendency of segregation at clean alloy surface. Moreover, according to the binary phase diagram [176-184], the additive elements is almost immiscible with Co and Fe atoms at room temperature and Au and Pt elements does not mix as well, indicating a repulsive interaction between these elements. Meanwhile, Cu and Pt forms an intermetallic compound in $L1_1$ structure at a composition near 50%-50% and an Cu_3Pt phase in $L1_2$ structure in the Cu rich region; analogous to this isoelectronic system, Ag and Pt forms intermetallic compound in $L1_1$ structure as well. However, our results in Figure 5.24 and Figure 5.25 shows Ag substitution behaves more like Au substitution rather than Cu substitution. This suggests that the enthalpy of mixing effect does not dominate the surface segregation in the alloy system investigated. In Table 5.13, we also tabulate the lattice constant of all relevant elements in fcc structure. The lattice constant correlates with the atomic radius. The additive element Ag and Au is much larger than the matrix elements whereas Cu has a size comparable with the matrix elements, resulting a severe strain for Ag and Au doping and a moderate strain for Cu doping. This strain energy effect explains well the observed much more negative E_{seg} for Ag and Au doping.

Table 5.13 Lattice constant a and surface energy γ for elementary bulk crystal. The lattice constant is calculated for each element in fcc structure. Surface energy values are adopted from ref. [175].

	Cu	Ag	Au	Co	Fe	Pt
a(Å)	3.64	4.16	4.17	3.52	3.46	3.99
γ(eV/atom)	0.707	0.553	0.611	0.961*	0.978+	1.004
γ(J/m^2)	1.952	1.172	1.283	2.775*	2.430+	2.299

*Co in hcp structure

+Fe in bcc structure

E_{seg} in Figure 5.24 and Figure 5.25 for Co/Fe substitution is not direction comparable with Pt substitution owing to the composition mismatch in the reference state. To investigate whether additive atoms prefer to segregate at Co/Fe site or Pt site, one must introduce the chemical potential term μ in equation 5.6. The segregation energies difference of outermost surface Co/Fe site and Pt site is given by:

$$\begin{aligned}\Delta E_{seg} &= E^{X}_{seg\_Co/Fe(1)} - E^{X}_{seg\_Pt(8)} \\ &= E_{slab}\left[Co/Fe_{N-1}\,Pt_N X^{(1)}\right] - E_{slab}\left[Co/Fe_{N-1}\,Pt_N X^{(5)}\right] - E_{slab}\left[Co/Fe_N\,Pt_{N-1} X^{(8)}\right] \\ &\quad + E_{slab}\left[Co/Fe_N\,Pt_{N-1} X^{(4)}\right] \\ &= E_{slab}\left[Co/Fe_{N-1}Pt_N X^{(1)}\right] - E_{slab}\left[Co/Fe_N Pt_{N-1} X^{(8)}\right] + \mu_{Co/Fe} - \mu_{Pt} \qquad (5.7)\end{aligned}$$

The chemical potential of atoms in slab equilibrates with bulk $L1_0$ phase which could be extracted from the first principles calculations of bulk (Co/Fe)Pt:

$$\mu_{Co/Fe} + \mu_{Pt} = \mu_{(Co/Fe)Pt} \qquad (5.8)$$

Therefore, the relative stability of surface Co/Fe site with respect to Pt site is a linear function of μ_{Pt}, which is plotted in Figure 5.26. In this figure, the chemical potential of pure fcc Pt is taken as

reference and μ_{Pt}=0 corresponds to the upper limit that the slab equilibrates with fcc Pt. The lower limit could be calculated by set $\mu_{Co/Fe}$ as the those in fcc Fe and Co.

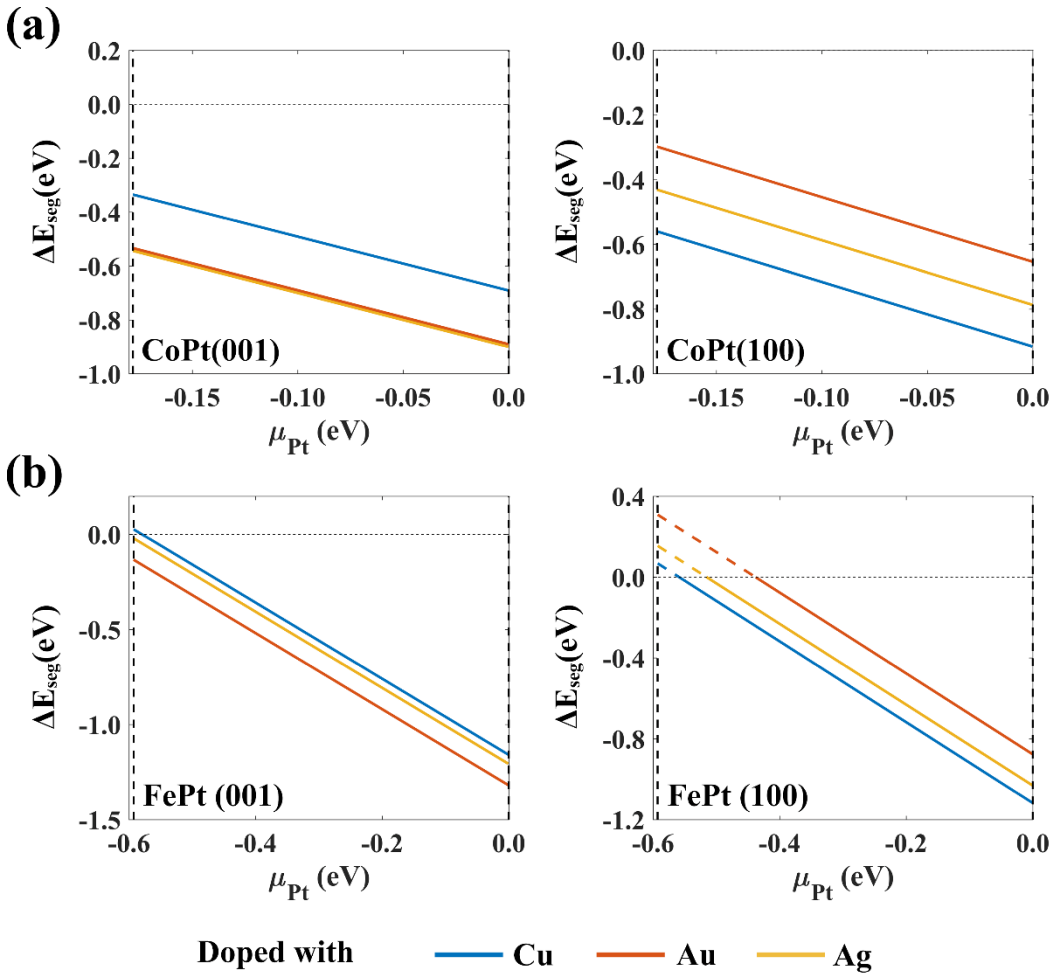

Figure 5.26 The segregation energy difference between the substitution position of surface Co/Fe and surface Pt. The chemical potential of Pt atoms is calculated taking the bulk fcc Pt as reference. In this figure, positive (negative) energy difference indicate that the impurity atom prefers to segregate at surface Pt (Co) site.

Our results in Figure 5.26 show that the on CoPt (001) and (100) surface, ΔE_{seg} is always negative through the chemical potential range investigated, implying that surface Co site is more energetically favorable than Pt site for the substitutional impurity atoms Cu, Ag and Au. Similar behavior is found on FePt (001) surface doped with Au and Ag atoms where ΔE_{seg} is always negative. On the other hand, the segregation energy could become positive when the chemical potential of Pt atoms is low enough (dashed line in Figure 5.26), for example on (001) FePt surface doped with Cu atom, indicating the preferential segregation site transits from surface Fe site to Pt site. This observation is much more pronounced on (100) FePt surface. The transition chemical potential point is found to be -0.56eV, -0.52eV, -0.44 eV for Cu, Ag and Au doping, respectively.

5.5.2 Magnetic Properties of doped CoPt and FePt surfaces

Therefore, we have demonstrated that the additive Cu, Ag and Au atoms prefers to segregate to surface, particularly surface Co/Fe site in $L1_0$ ordered CoPt and FePt slabs. If the concentration of dopant is well controlled, the fully segregated structure would be [X/bulk] on (001) surface and [$X_{0.5}Pt_{0.5}$/bulk] on (100) surface and the Pt surface segregation could be inhibited (X is the additive element). The structures could be conceived by replacing all outermost surface Co/Fe atoms by the additive atoms in Figure 5.23. Compared with the fully segregated surface structure in our previous study, the local ordering near surface is partially repaired.

It is anticipated that the repair of local ordering would recover the magnetic properties of CoPt and FePt slabs. However, the introduction of impurities would in turn be harmful to the magnetic properties due to the hybridization of impurity orbitals with matrix orbitals. In this sense, we summarize the spin magnetic moment μ_s of surface and subsurface atoms on fully segregated

surface slab in Table 5.14 and Table 5.15. For comparison, the μ_s of corresponding bulk terminated surfaces, Pt-segregated surfaces are present as well.

Our results show that the magnetic moment of subsurface Co/Fe is higher than the corresponding atoms in Pt-segregated surfaces, indicating the additive atoms have some advantages in restoring the magnetic properties of CoPt and FePt nanostructures. The magnetic moment of subsurface Co/Fe is still lower than the bulk-terminated value. This finding could be attributed to the interaction of impurity atoms with matrix elements. This interaction is found relatively stronger for CoPt (001) and (100) surface and FePt (001) surface and is much weaker for FePt (100) surface, since the magnetic moment of Fe atoms is improved to the bulk-terminated value of 3.10 μ_B. Nevertheless, the magnetic moment of Pt atoms is always lower than the bulk-terminated value. In some cases, it could be even worse than those of the Pt atoms in Pt-segregated structure. For example, on FePt (001) surface doped with Cu atom, the magnetic moment of subsurface Pt atoms is about 0.10 μ_B lower than the surface Pt atoms on Pt-segregated (001) surface. We notice that on CoPt (001) surface and FePt (100) surface, the magnetic moment of Pt is about the same compared to the Pt-segregated value. Consequently, on these two surfaces, the additive of Cu, Ag and Au atoms are beneficial for the improvement of magnetic properties. However, on the other two surfaces, some additional aspect such as the doping concentration need to be further examined.

In Table 5.15, it can be observed that the additive possesses a finite magnetic moment on (100) surface and zero magnetic moment on (001) surface. The small negative value in the table is due to numerical error. Since all the impurity elements are nonmagnetic elements, the existence of finite moment is therefore attributed to the hybridization with Co/Fe orbitals. On (001) fully segregated surface, the impurity atom has zero nearest neighbor of Co/Fe atoms while on (100)

fully segregated surface, there are two neighboring Co/Fe atoms right below the surface layer. This coordination number of neighboring Co/Fe atoms agrees well with the surface dependence of magnetic moment on impurity atoms.

Table 5.14 Predicted spin magnetic moment μ_s (μ_B) of surface and subsurface atoms on fully segregated surface. The superscript denotes the number of atomic layers that the atom occupies. For comparison, the μ_s of corresponding bulk terminated surfaces, Pt-segregated surfaces are present as well. For bulk-terminated surfaces, the value of Co/Fe atoms correspond to Co/Fe-terminated surface and the value of Pt atoms correspond to Pt-terminated surface.

Surface		Cu		Ag		Au		Bulk-terminated		Pt-segregated	
		Co/Fe	Pt	Co/Fe	Pt	Co/Fe	Pt	Co/Fe	Pt	Co/Fe	Pt
CoPt	(001)	1.89^3	0.24^2	1.90^3	0.27^2	1.90^3	0.28^2	1.96^1	0.36^1	1.85^2	0.26^1
	(100)	1.94^2	0.31^1	1.97^2	0.25^1	1.96^2	0.25^1	1.98^1	0.39^1	1.88^2	0.32^1
FePt	(001)	2.91^3	0.19^2	2.92^3	0.22^2	2.91^3	0.24^2	2.99^1	0.34^1	2.86^2	0.29^1
	(100)	3.10^2	0.36^1	3.10^2	0.32^1	3.10^2	0.31^2	3.10^1	0.37^1	2.90^2	0.33^1

Table 5.15 Predicted spin magnetic moment μ_s of impurity atoms on fully segregated surface.

Surface		Impurity Atoms		
		Cu	Ag	Au
CoPt	(001)	0.00	-0.01	-0.01
	(100)	0.07	0.01	0.03
FePt	(001)	0.00	-0.01	0.00
	(100)	0.10	0.03	0.06

6.0 CONCLUSIONS AND PROSPECTS

This work focuses on the prediction and explanation of magnetic properties of CoPt and FePt nanoparticles using atomistic computation method. Several surface related phenomena have been carefully investigated, e.g. surface segregation, surface spin canting, shape dependent magnetism, surface anisotropy and magnetostriction. This work involves several levels of simulations, from the structure of bulk, surface slabs through nanoclusters, and from the first principles calculation to micromagnetic modeling. Specifically, the surface segregation effect has been evaluated in cuboidal, cuboctahedral nanoparticles and the related low index surfaces of $L1_0$ ordered CoPt alloy. How the magnetic properties of $L1_0$ CoPt and FePt nanoparticles are affected by particle shape (i.e., cuboctahedral, decahedral, and icosahedra shapes with same composition) has been investigated. The magnetoelastic analysis and micromagnetic simulation have been performed to explain the different surface spin canting fashion between FePt and CoPt nanoparticles. Finally, an approach to modify the surface composition profile as well as the surface magnetic properties has been suggested.

In summary, the hypotheses proposed in 3.0 have been evaluated and the main conclusions are drawn as follow:

1. Pt surface segregation to the outermost surface of the CoPt nanoparticles is thermodynamically favorable. This segregation can directly cause the break in local structural and chemical ordering at particle surface. As compared to the corresponding bulk-terminated

nanoparticles, the surface-segregated nanoparticles exhibit reduced magnetic moment and magnetic anisotropy energy.

2. The structural and magnetic properties of the (001), (100), (101), (110) and (111) CoPt surfaces have been evaluated. Among the five types of surfaces, (111) surface has the least extent of surface relaxation and the lowest surface energy. The magnetic moment of surface atoms in the bulk-terminated CoPt surfaces is normally higher than that of bulk atoms. The surface atoms provide a noticeable contribution to the magnetic anisotropy energy (MAE) favoring in-plane (parallel to the surface) magnetization.

It is energetically favorable for the sublayer Pt atoms to segregate to the outermost layer of the bulk-terminated surfaces. The Pt segregation energy of (001) surface is about 0.47 eV energy gain per segregated atom and is found to be the most pronounced among the five surfaces studied. As compared to the corresponding bulk-terminated surface, these Pt-segregated CoPt surfaces would have larger contraction relaxation, reduced magnetic moments (with a notable exception of (110) surface) and a MAE favoring out-of-plane (perpendicular to the surface) magnetization.

Within the second order perturbation theory, a qualitative link between the *d* electron density of states of the surface atoms and the MAE has been established. The observed MAE term in bulk-terminated (segregated) surface correlates with the increased (decreased) d_{z^2} state density of surface Co atoms in the minority spin channel.

3. Among the three particle shapes (cuboctahedral, decahedral, and icosahedra) investigated, the decahedral nanoparticles had appreciably lower surface magnetic moment. This reduction in the surface magnetism is found related to large contraction of atomic spacing and high local Co (or Fe) concentration in the surface of the decahedral nanoparticles. CoPt and FePt cuboctahedral nanoparticles exhibit dramatically different surface spin canting fashions, i.e.

“artichoke” structure for CoPt and “throttled” structure for FePt. The surface spin structure can be explained by surface anisotropy energy calculated from low index surfaces.

4. The observed spin canting fashions are reproduced by micromagnetic simulation using Néel’s surface anisotropy model. The “artichoke” structure corresponds to a positive Néel’s constant while the “throttled” structure corresponds to negative Néel’s constant.

The magnetoelastic coupling constant has been calculated using DFT method and FePt is found to show stronger response under the action of external magnetic field than CoPt. Higher order expansion of magnetoelastic coupling is needed in CoPt.

The equations that links Néel’s constant with the magnetoelastic coupling constant have been derived, with the postulation that the Néel’s constant captures anisotropy energy change subject to 4 particular volume conserved strains and pure volume term is neglected. The Néel’s constant for the Co-Co(Pt-Pt) pair in CoPt are calculated to be +3.42 meV while in contrast, the Néel constant for the Fe-Fe(Pt-Pt) pair in FePt are calculated to be -8.62 meV. These results are consistent with micromagnetic simulation.

5. The additive elements Cu, Ag and Au in CoPt and FePt surface slabs favor the outermost surface sites rather than the bulk sites. Throughout a very wide range of Pt chemical potential, the additive atoms prefer substitute surface Co/Fe atoms over Pt atoms. This segregation correlates well with the surface energy and atomic size of impurity atoms. Therefore, the doping of Cu, Ag and Au facilitates the suppression of Pt segregation in CoPt and FePt. In this way, the magnetic moment of surface Co/Fe atoms is restored to the value of bulk-terminated surface. On CoPt (001) surface and FePt (100) surface, these additive atoms are proved to be beneficial for the improvement of magnetic properties.

Therefore, our DFT computational results give physical insights into how the surface magnetism are affected by the structure and composition of the surface. These insights are helpful for future design of CoPt and FePt alloy nanoparticles with enhanced magnetic properties.

There are still challenges on the prediction and design of magnetic properties of CoPt and FePt nanoparticles. In the computer simulation point of view, the following outlooks can be anticipated: DFT is only capable for simulating material system composed of 10s to 100s of atoms because of the limited computer capability and resources. This limits the application of DFT in simulating realistic materials system such as disordered alloys, nanoparticles sized 3nm or more. At this point, the Monte Carlo (MC) and Molecular Dynamics (MD) simulations based on the empirical interatomic potential such as Modified Embedded Atom Method (MEAM) are more advantageous. The MEAM potential that fully captures the surface segregation in CoPt and FePt needs to be developed. If the impurity elements effect is to be simulated, the ternary interaction need also to be parametrized. The MEAM based MC or MD simulation can be further incorporated with the micromagnetic simulation assuming different magnitude of spin moment on each atomic site. The spin dynamics could also be included utilizing the Landau–Lifshitz–Gilbert equation [185,186]. In this way, the structural and magnetic response of more realistic materials as a function of time evolution could be simulated simultaneously.

BIBLIOGRAPHY

[1] A. Moser, K. Takano, D. T. Margulies, M. Albrecht, Y. Sonobe, Y. Ikeda, S. H. Sun, and E. E. Fullerton, Magnetic recording: advancing into the future, J. Phys. D Appl. Phys. **35**, R157 (2002).

[2] seagate tech talk - HDD Areal Density, seagate tech talk - HDD Areal Density http://www.seagate.com/investors/tech-and-trends/tech-talks/.

[3] T. C. Arnoldussen and E. M. Rossi, Materials for Magnetic Recording, Annu. Rev. Mater. Sci. **15**, 379 (1985).

[4] S. N. Piramanayagam and K. Srinivasan, Recording media research for future hard disk drives, J. Magn. Magn. Mater. **321**, 485 (2009).

[5] H. N. Bertram and M. Williams, SNR and density limit estimates: A comparison of longitudinal and perpendicular recording, IEEE Trans. Magn. **36**, 4 (2000).

[6] H. N. Bertram, H. Zhou, and R. Gustafson, Signal to noise ratio scaling and density limit estimates in longitudinal magnetic recording, IEEE Trans. Magn. **34**, 1845 (1998).

[7] C. H. Hee, Y. Y. Zou, and J. P. Wang, Tilted media by micromagnetic simulation: A possibility for the extension of longitudinal magnetic recording?, J. Appl. Phys. **91**, 8004 (2002).

[8] R. H. Victora, J. H. Xue, and M. Patwari, Areal density limits for perpendicular magnetic recording, IEEE Trans. Magn. **38**, 1886 (2002).

[9] S. N. Piramanayagam, Perpendicular recording media for hard disk drives, J. Appl. Phys. **102**, 2 (2007).

[10] Density Multiplication and Improved Lithography by Directed Block Copolymer Assembly for Patterned Media at 1Tbit/in2 and Beyond, HGST - Patterned Media White Paper https://www.hgst.com/.

[11] C. Ross, Patterned magnetic recording media, Ann. Rev. Mater. Res. **31**, 203 (2001).

[12] D. Weller, A. Moser, L. Folks, M. E. Best, W. Lee, M. F. Toney, M. Schwickert, J. U. Thiele, and M. F. Doerner, High K-u materials approach to 100 Gbits/in(2), IEEE Trans. Magn. **36**, 10 (2000).

[13] K. Rajan, Materials informatics, Mater. Today **8**, 38 (2005).

[14] D. Weller and A. Moser, Thermal effect limits in ultrahigh-density magnetic recording, IEEE Trans. Magn. **35**, 4423 (1999).

[15] S. H. Whang, Q. Feng, and Y. Q. Gao, Ordering, deformation and microstructure in L1(0) type FePt, Acta Materialia **46**, 6485 (1998).

[16] ASM handbook. Volume 3, Alloy phase diagrams (ASM International, Materials Park, OH, 1992).

[17] D. Alloyeau, C. Ricolleau, C. Mottet, T. Oikawa, C. Langlois, Y. Le Bouar, N. Braidy, and A. Loiseau, Size and shape effects on the order-disorder phase transition in CoPt nanoparticles, Nat. Mater. **8**, 940 (2009).

[18] C. Di Paola, R. D'Agosta, and F. Baletto, Geometrical Effects on the Magnetic Properties of Nanoparticles, Nano Lett. **16**, 2885 (2016).

[19] M. E. Gruner, G. Rollmann, P. Entel, and M. Farle, Multiply twinned morphologies of FePt and CoPt nanoparticles, Phys. Rev. Lett. **100**, 087203 (2008).

[20] A. Dannenberg, M. E. Gruner, A. Hucht, and P. Entel, Surface energies of stoichiometric FePt and CoPt alloys and their implications for nanoparticle morphologies, Phys. Rev. B **80**, 245438 (2009).

[21] Z. R. Dai, S. H. Sun, and Z. L. Wang, Shapes, multiple twins and surface structures of monodisperse FePt magnetic nanocrystals, Surf. Sci. **505**, 325 (2002).

[22] Z. A. Li, M. Spasova, Q. M. Ramasse, M. E. Gruner, C. Kisielowski, and M. Farle, Chemically ordered decahedral FePt nanocrystals observed by electron microscopy, Phys. Rev. B **89**, 161406 (2014).

[23] Z. R. Dai, S. H. Sun, and Z. L. Wang, Phase transformation, coalescence, and twinning of monodisperse FePt nanocrystals, Nano Lett. **1**, 443 (2001).

[24] R. M. Wang, H. Z. Zhang, M. Farle, and C. Kisielowski, Structural stability of icosahedral FePt nanoparticles, Nanoscale **1**, 276 (2009).

[25] R. M. Wang, O. Dmitrieva, M. Farle, G. Dumpich, M. Acet, S. Mejia-Rosales, E. Perez-Tijerina, M. J. Yacaman, and C. Kisielowski, FePt Icosahedra with Magnetic Cores and Catalytic Shells, J. Phys. Chem. C **113**, 4395 (2009).

[26] J. Penuelas, P. Andreazza, C. Andreazza-Vignolle, H. C. N. Tolentino, M. De Santis, and C. Mottet, Controlling structure and morphology of CoPt nanoparticles through dynamical or static coalescence effects, Phys. Rev. Lett. **100**, 115502 (2008).

[27] V. Nandwana, K. E. Elkins, N. Poudyal, G. S. Chaubey, K. Yano, and J. P. Liu, Size and shape control of monodisperse FePt nanoparticles, J. Phys. Chem. C **111**, 4185 (2007).

[28] R. M. Wang, O. Dmitrieva, M. Farle, G. Dumpich, H. Q. Ye, H. Poppa, R. Kilaas, and C. Kisielowski, Layer resolved structural relaxation at the surface of magnetic FePt icosahedral nanoparticles, Phys. Rev. Lett. **100**, 017205 (2008).

[29] C. A. F. Vaz, J. A. C. Bland, and G. Lauhoff, Magnetism in ultrathin film structures, Rep. Prog. Phys. **71**, 056501 (2008).

[30] M. Respaud, J. M. Broto, H. Rakoto, A. R. Fert, L. Thomas, B. Barbara, M. Verelst, E. Snoeck, P. Lecante, A. Mosset, J. Osuna, T. Ould-Ely, C. Amiens, and B. Chaudret, Surface effects on the magnetic properties of ultrafine cobalt particles, Phys. Rev. B **57**, 2925 (1998).

[31] J. Osuna, D. deCaro, C. Amiens, B. Chaudret, E. Snoeck, M. Respaud, J. M. Broto, and A. Fert, Synthesis, characterization, and magnetic properties of cobalt nanoparticles from an organometallic precursor, J. Phys. Chem. **100**, 14571 (1996).

[32] I. M. L. Billas, A. Chatelain, and W. A. Deheer, Magnetism from the Atom to the Bulk in Iron, Cobalt, and Nickel Clusters, Science **265**, 1682 (1994).

[33] F. Luis, J. M. Torres, L. M. Garcia, J. Bartolome, J. Stankiewicz, F. Petroff, F. Fettar, J. L. Maurice, and A. Vaures, Enhancement of the magnetic anisotropy of nanometer-sized Co clusters: Influence of the surface and of interparticle interactions, Phys. Rev. B **65**, 094409 (2002).

[34] S. Oyarzun, A. Tamion, F. Tournus, V. Dupuis, and M. Hillenkamp, Size effects in the magnetic anisotropy of embedded cobalt nanoparticles: from shape to surface, Sci. Rep. **5**, 14749 (2015).

[35] P. Gambardella, S. Rusponi, M. Veronese, S. S. Dhesi, C. Grazioli, A. Dallmeyer, C. I, R. Zeller, P. H. Dederichs, K. Kern, C. Carbone, and H. Brune, Giant magnetic anisotropy of single cobalt atoms and nanoparticles, Science **300**, 1130 (2003).

[36] D. L. Peng, T. Hihara, K. Sumiyama, and H. Morikawa, Structural and magnetic characteristics of monodispersed Fe and oxide-coated Fe cluster assemblies, J. Appl. Phys. **92**, 3075 (2002).

[37] F. Bodker, S. Morup, and S. Linderoth, Surface Effects in Metallic Iron Nanoparticles, Phys. Rev. Lett. **72**, 282 (1994).

[38] G. van der Laan, Microscopic origin of magnetocrystalline anisotropy in transition metal thin films, J. Phys.: Condens. Mat. **10**, 3239 (1998).

[39] G. M. Pastor, J. Dorantesdavila, S. Pick, and H. Dreysse, Magnetic-Anisotropy of 3d Transition-Metal Clusters, Phys. Rev. Lett. **75**, 326 (1995).

[40] G. M. Pastor and J. Dorantesdavila, Magnetic anisotropy of 3D transition metal clusters and ultrathin films, Mat. Sci. Eng. A **217**, 286 (1996).

[41] O. Hjortstam, J. Trygg, J. M. Wills, B. Johansson, and O. Eriksson, Calculated spin and orbital moments in the surfaces of the 3d metals Fe, Co, and Ni and their overlayers on Cu(001), Phys. Rev. B **53**, 9204 (1996).

[42] A. J. Freeman and R. Q. Wu, Electronic-Structure Theory of Surface, Interface and Thin-Film Magnetism, J. Magn. Magn. Mater. **100**, 497 (1991).

[43] F. Tournus, A. Tamion, N. Blanc, A. Hannour, L. Bardotti, B. Prevel, P. Ohresser, E. Bonet, T. Epicier, and V. Dupuis, Evidence of L1(0) chemical order in CoPt nanoclusters: Direct observation and magnetic signature, Phys. Rev. B **77**, 144411 (2008).

[44] F. Tournus, N. Blanc, A. Tamion, M. Hillenkamp, and V. Dupuis, Synthesis and magnetic properties of size-selected CoPt nanoparticles, J. Magn. Magn. Mater. **323**, 1868 (2011).

[45] X. C. Sun, Z. Y. Jia, Y. H. Huang, J. W. Harrell, D. E. Nikles, K. Sun, and L. M. Wang, Synthesis and magnetic properties of CoPt nanoparticles, J. Appl. Phys. **95**, 6747 (2004).

[46] T. Klemmer, D. Hoydick, H. Okumura, B. Zhang, and W. A. Soffa, Magnetic Hardening and Coercivity Mechanisms in L1(0) Ordered Fepd Ferromagnets, Scripta Metall. Mater. **33**, 1793 (1995).

[47] V. Tzitzios, D. Niarchos, G. Margariti, J. Fidler, and D. Petridis, Synthesis of CoPt nanoparticles by a modified polyol method: characterization and magnetic properties, Nanotechnology **16**, 287 (2005).

[48] B. Rellinghaus, S. Stappert, M. Acet, and E. F. Wassermann, Magnetic properties of FePt nanoparticles, J. Magn. Magn. Mater. **266**, 142 (2003).

[49] S. H. Sun, C. B. Murray, D. Weller, L. Folks, and A. Moser, Monodisperse FePt nanoparticles and ferromagnetic FePt nanocrystal superlattices, Science **287**, 1989 (2000).

[50] S. Okamoto, O. Kitakami, N. Kikuchi, T. Miyazaki, Y. Shimada, and Y. K. Takahashi, Size dependences of magnetic properties and switching behavior in FePt L1(0) nanoparticles, Phys. Rev. B **67**, 094422 (2003).

[51] J. Y. Fang, L. D. Tung, K. L. Stokes, J. B. He, D. Caruntu, W. L. L. Zhou, and C. J. O'Connor, Synthesis and magnetic properties of CoPt-poly(methylmethacrylate) nanostructured composite material, J. Appl. Phys. **91**, 8816 (2002).

[52] S. Rohart, C. Raufast, L. Favre, E. Bernstein, E. Bonet, W. Wernsdorfer, and V. Dupuis, Interface effect on the magnetic anisotropy of CoPt clusters, J. Magn. Magn. Mater. **316**, E355 (2007).

[53] O. Dmitrieva, M. Spasova, C. Antoniak, M. Acet, G. Dumpich, J. Kastner, M. Farle, K. Fauth, U. Wiedwald, H. G. Boyen, and P. Ziemann, Magnetic moment of Fe in oxide-free FePt nanoparticles, Phys. Rev. B **76**, 064414 (2007).

[54] E. V. Shevchenko, D. V. Talapin, H. Schnablegger, A. Kornowski, O. Festin, P. Svedlindh, M. Haase, and H. Weller, Study of nucleation and growth in the organometallic synthesis of magnetic alloy nanocrystals: The role of nucleation rate in size control of CoPt3 nanocrystals, J. Am. Chem. Soc. **125**, 9090 (2003).

[55] C. B. Rong, D. R. Li, V. Nandwana, N. Poudyal, Y. Ding, Z. L. Wang, H. Zeng, and J. P. Liu, Size-dependent chemical and magnetic ordering in L1(0)-FePt nanoparticles, Adv. Mater. **18**, 2984 (2006).

[56] U. Pustogowa, J. Zabloudil, C. Uiberacker, C. Blaas, P. Weinberger, L. Szunyogh, and C. Sommers, Magnetic properties of thin films of Co and of (CoPt) superstructures on Pt(100) and Pt(111), Phys. Rev. B **60**, 414 (1999).

[57] Z. X. Tang, C. M. Sorensen, K. J. Klabunde, and G. C. Hadjipanayis, Size-Dependent Curie-Temperature in Nanoscale Mnfe2o4 Particles, Phys. Rev. Lett. **67**, 3602 (1991).

[58] M. P. Morales, S. Veintemillas-Verdaguer, M. I. Montero, C. J. Serna, A. Roig, L. Casas, B. Martinez, and F. Sandiumenge, Surface and internal spin canting in gamma-Fe2O3 nanoparticles, Chem. Mater. **11**, 3058 (1999).

[59] S. Srivastava and N. S. Gajbhiye, Exchange coupled L1(0)-FePt/fcc-FePt nanomagnets: Synthesis, characterization and magnetic properties, J. Magn. Magn. Mater. **401**, 969 (2016).

[60] Y. S. Yang, C. C. Chen, M. C. Scott, C. Ophus, R. Xu, A. Pryor, L. Wu, F. Sun, W. Theis, J. H. Zhou, M. Eisenbach, P. R. C. Kent, R. F. Sabirianov, H. Zeng, P. Ercius, and J. W. Miao, Deciphering chemical order/disorder and material properties at the single-atom level, Nature **542**, 75 (2017).

[61] G. F. Wang, M. A. Van Hove, P. N. Ross, and M. I. Baskes, Quantitative prediction of surface segregation in bimetallic Pt-M alloy nanoparticles (M = Ni, Re, Mo), Prog. Surf. Sci. **79**, 28 (2005).

[62] G. F. Wang, M. A. Van Hove, P. N. Ross, and M. I. Baskes, Monte Carlo simulations of segregation in Pt-Ni catalyst nanoparticles, J. Chem. Phys. **122**, 024706 (2005).

[63] G. F. Wang, M. A. Van Hove, P. N. Ross, and M. I. Baskes, Surface structures of cubo-octahedral Pt-Mo catalyst nanoparticles from Monte Carlo simulations, J. Phys. Chem. B **109**, 11683 (2005).

[64] Z. Y. Duan, J. Zhong, and G. F. Wang, Modeling surface segregation phenomena in the (111) surface of ordered Pt3Ti crystal, J. Chem. Phys. **133**, 114701 (2010).

[65] Z. Y. Duan and G. F. Wang, Monte Carlo simulation of surface segregation phenomena in extended and nanoparticle surfaces of Pt-Pd alloys, J. Phys.: Condens. Mat. **23**, 475301 (2011).

[66] Y. H. Zhang, Z. Y. Duan, C. Xiao, and G. F. Wang, Density functional theory calculation of platinum surface segregation energy in Pt3Ni (111) surface doped with a third transition metal, Surf. Sci. **605**, 1577 (2011).

[67] F. F. Abraham and C. R. Brundle, Surface Segregation in Binary Solid-Solutions - a Theoretical and Experimental Perspective, J. Vac. Sci. Technol. **18**, 506 (1981).

[68] P. A. Dowben and A. Miller, Surface segregation phenomena (CRC Press, Boca Raton, Fla., 1990).

[69] K. J. J. Mayrhofer, K. Hartl, V. Juhart, and M. Arenz, Degradation of Carbon-Supported Pt Bimetallic Nanoparticles by Surface Segregation, J. Am. Chem. Soc. **131**, 16348 (2009).

[70] J. Shu, B. E. W. Bongondo, B. P. A. Grandjean, A. Adnot, and S. Kaliaguine, Surface Segregation of Pd-Ag Membranes Upon Hydrogen Permeation, Surf. Sci. **291**, 129 (1993).

[71] V. Stamenkovic, T. J. Schmidt, P. N. Ross, and N. M. Markovic, Surface segregation effects in electrocatalysis: kinetics of oxygen reduction reaction on polycrystalline Pt3Ni alloy surfaces, J. Electroanal. Chem. **554**, 191 (2003).

[72] K. J. J. Mayrhofer, V. Juhart, K. Hartl, M. Hanzlik, and M. Arenz, Adsorbate-Induced Surface Segregation for Core-Shell Nanocatalysts, Angew. Chem. Int. Edit. **48**, 3529 (2009).

[73] G. E. Ramirez-Caballero, Y. G. Ma, R. Callejas-Tovar, and P. B. Balbuena, Surface segregation and stability of core-shell alloy catalysts for oxygen reduction in acid medium, Phys. Chem. Chem. Phys. **12**, 2209 (2010).

[74] L. Zou, C. Yang, Y. Lei, D. Zakharov, J. Wiezorek, D. Su, Q. Yin, J. Li, Z. Liu, E. Stach, J. Yang, L. Qi, and G. Wang, Facilitating dislocation nucleation through atomic segregation, Nat. Mater., accepted for publication.

[75] M. Polak and L. Rubinovich, The interplay of surface segregation and atomic order in alloys, Surf. Sci. Rep. **38**, 127 (2000).

[76] P. Wynblatt and R. C. Ku, Surface-Energy and Solute Strain-Energy Effects in Surface Segregation, Surf. Sci. **65**, 511 (1977).

[77] J. B. Miller, B. D. Morreale, and A. J. Gellman, The effect of adsorbed sulfur on surface segregation in a polycrystalline Pd70Cu30 alloy, Surf. Sci. **602**, 1819 (2008).

[78] D. Tomanek, S. Mukherjee, V. Kumar, and K. H. Bennemann, Calculation of Chemisorption and Absorption Induced Surface Segregation, Surf. Sci. **114**, 11 (1982).

[79] J. Luyten, S. Helfensteyn, and C. Creemers, Segregation in ternary alloys: an interplay of driving forces, Appl. Surf. Sci. **212**, 833 (2003).

[80] A. M. Tarditi and L. M. Cornaglia, Novel PdAgCu ternary alloy as promising materials for hydrogen separation membranes: Synthesis and characterization, Surf. Sci. **605**, 62 (2011).

[81] A. Lopes, G. Treglia, C. Mottet, and B. Legrand, Ordering and surface segregation in Co 1-c Pt-c nanoparticles: A theoretical study from surface alloys to nanoalloys, Phys. Rev. B **91**, 035407 (2015).

[82] R. V. Chepulskii and W. H. Butler, Tuning of L1(0) atomic order in Co-Pt nanoparticles: Ab initio insights, Phys. Rev. B **86**, 155401 (2012).

[83] R. V. Chepulskii, W. H. Butler, A. van de Walle, and S. Curtarolo, Surface segregation in nanoparticles from first principles: The case of FePt, Scripta Mater. **62**, 179 (2010).

[84] L. Y. Han, U. Wiedwald, B. Kuerbanjiang, and P. Ziemann, Fe oxidation versus Pt segregation in FePt nanoparticles and thin films, Nanotechnology **20**, 285706 (2009).

[85] D. L. Wang, H. L. L. Xin, R. Hovden, H. S. Wang, Y. C. Yu, D. A. Muller, F. J. DiSalvo, and H. D. Abruna, Structurally ordered intermetallic platinum-cobalt core-shell nanoparticles with enhanced activity and stability as oxygen reduction electrocatalysts, Nat. Mater. **12**, 81 (2013).

[86] F. Tournus, K. Sato, T. Epicier, T. J. Konno, and V. Dupuis, Multi-L1(0) Domain CoPt and FePt Nanoparticles Revealed by Electron Microscopy, Phys. Rev. Lett. **110**, 055501 (2013).

[87] M. Bohra, P. Grammatikopoulos, R. E. Diaz, V. Singh, J. L. Zhao, J. F. Bobo, A. Kuronen, F. Djurabekova, K. Nordlund, and M. Sowwan, Surface Segregation in Chromium-Doped NiCr Alloy Nanoparticles and Its Effect on Their Magnetic Behavior, Chem. Mater. **27**, 3216 (2015).

[88] W. Grange, M. Maret, J. P. Kappler, J. Vogel, A. Fontaine, F. Petroff, G. Krill, A. Rogalev, J. Goulon, M. Finazzi, and N. B. Brookes, Magnetocrystalline anisotropy in (111) CoPt3 thin films probed by x-ray magnetic circular dichroism, Phys. Rev. B **58**, 6298 (1998).

[89] W. Grange, I. Galanakis, M. Alouani, M. Maret, J. P. Kappler, and A. Rogalev, Experimental and theoretical x-ray magnetic-circular-dichroism study of the magnetic properties of Co50Pt50 thin films, Phys. Rev. B **62**, 1157 (2000).

[90] D. L. Mills, Surface Anisotropy and Surface Spin Canting in the Semi-Infinite Ferromagnet, Phys. Rev. B **39**, 12306 (1989).

[91] L. Neel, *Anisotropie Magnetique Superficielle Et Surstructures Dorientation, Journal De Physique Et Le Radium **15**, 225 (1954).

[92] R. Skomski, Magnetoelectric Neel anisotropies, IEEE. Trans. Magn. **34**, 1207 (1998).

[93] R. Skomski, A. Kashyap, A. Solanki, A. Enders, and D. J. Sellmyer, Magnetic anisotropy in itinerant magnets, J. Appl. Phys. **107**, 09A735 (2010).

[94] M. Jamet, W. Wernsdorfer, C. Thirion, D. Mailly, V. Dupuis, P. Melinon, and A. Perez, Magnetic anisotropy of a single cobalt nanocluster, Phys. Rev. Lett. **86**, 4676 (2001).

[95] C. Chen, O. Kitakami, S. Okamoto, and Y. Shimada, Surface anisotropy in giant magnetic coercivity effect of cubic granular FeCo/SiO2 and NiCo/SiO2 films: A comparison with Neel's theory, J. Appl. Phys. **86**, 2161 (1999).

[96] M. Jamet, W. Wernsdorfer, C. Thirion, V. Dupuis, P. Melinon, A. Perez, and D. Mailly, Magnetic anisotropy in single clusters, Phys. Rev. B **69**, 024401 (2004).

[97] P. Hohenberg and W. Kohn, Inhomogeneous Electron Gas, Phys. Rev. **136**, B864 (1964).

[98] W. Kohn and L. J. Sham, Self-Consistent Equations Including Exchange and Correlation Effects, Phys. Rev. **140**, 1133 (1965).

[99] D. M. Ceperley and B. J. Alder, Ground-State of the Electron-Gas by a Stochastic Method, Phys. Rev. Lett. **45**, 566 (1980).

[100] C. S. Wang, B. M. Klein, and H. Krakauer, Theory of Magnetic and Structural Ordering in Iron, Phys. Rev. Lett. **54**, 1852 (1985).

[101] J. P. Perdew and Y. Wang, Accurate and Simple Analytic Representation of the Electron-Gas Correlation-Energy, Phys. Rev. B **45**, 13244 (1992).

[102] J. P. Perdew, M. Emzerhof, and K. Burke, Rationale for mixing exact exchange with density functional approximations, J. Chem. Phys. **105**, 9982 (1996).

[103] J. P. Perdew, A. Ruzsinszky, G. I. Csonka, O. A. Vydrov, G. E. Scuseria, L. A. Constantin, X. L. Zhou, and K. Burke, Restoring the density-gradient expansion for exchange in solids and surfaces, Phys. Rev. Lett. **100**, 136406 (2008).

[104] R. Armiento and A. E. Mattsson, Functional designed to include surface effects in self-consistent density functional theory, Phys. Rev. B **72**, 085108 (2005).

[105] J. M. Tao, J. P. Perdew, V. N. Staroverov, and G. E. Scuseria, Climbing the density functional ladder: Nonempirical meta-generalized gradient approximation designed for molecules and solids, Phys. Rev. Lett. **91**, 146401 (2003).

[106] J. Heyd, G. E. Scuseria, and M. Ernzerhof, Hybrid functionals based on a screened Coulomb potential, J. Chem. Phys. **118**, 8207 (2003).

[107] U. von Barth and L. Hedin, A local exchange-correlation potential for the spin polarized case. i, J. Phys. C Solid State **5**, 1629 (1972).

[108] S. V. Beiden, W. M. Temmerman, Z. Szotek, G. A. Gehring, G. M. Stocks, Y. Wang, D. M. C. Nicholson, W. A. Shelton, and H. Ebert, Real-space approach to the calculation of magnetocrystalline anisotropy in metals, Phys. Rev. B **57**, 14247 (1998).

[109] D. Weller, G. R. Harp, R. F. C. Farrow, A. Cebollada, and J. Sticht, Orientation Dependence of the Polar Kerr-Effect in Fcc and Hcp Co, Phys. Rev. Lett. **72**, 2097 (1994).

[110] G. Kresse and J. Hafner, Ab-Initio Molecular-Dynamics Simulation of the Liquid-Metal Amorphous-Semiconductor Transition in Germanium, Phys. Rev. B **49**, 14251 (1994).

[111] G. Kresse and D. Joubert, From ultrasoft pseudopotentials to the projector augmented-wave method, Phys. Rev. B **59**, 1758 (1999).

[112] D. Hobbs, G. Kresse, and J. Hafner, Fully unconstrained noncollinear magnetism within the projector augmented-wave method, Phys. Rev. B **62**, 11556 (2000).

[113] D. Fritsch and C. Ederer, First-principles calculation of magnetoelastic coefficients and magnetostriction in the spinel ferrites CoFe2O4 and NiFe2O4, Phys. Rev. B **86**, 014406 (2012).

[114] N. Metropolis, A. W. Rosenbluth, M. N. Rosenbluth, A. H. Teller, and E. Teller, Equation of State Calculations by Fast Computing Machines, J. Chem. Phys. **21**, 1087 (1953).

[115] J. A. Purton and N. L. Allan, Multi-million atom Monte Carlo simulation of oxide materials and solid solutions, Comp. Mater. Sci. **103**, 244 (2015).

[116] P. Vargas, D. Altbir, and J. D. E. Castro, Fast Monte Carlo method for magnetic nanoparticles, Phys. Rev. B **73**, 092417 (2006).

[117] L. B. Ho, T. N. Lan, and T. H. Hai, Monte Carlo simulations of core/shell nanoparticles containing interfacial defects: Role of disordered ferromagnetic spins, Physica B-Condensed Matter **430**, 10 (2013).

[118] M. Woinska, J. Szczytko, A. Majhofer, J. Gosk, K. Dziatkowski, and A. Twardowski, Magnetic interactions in an ensemble of cubic nanoparticles: A Monte Carlo study, Phys. Rev. B **88**, 144421 (2013).

[119] V. Russier, C. de-Montferrand, Y. Lalatonne, and L. Motte, Magnetization of densely packed interacting magnetic nanoparticles with cubic and uniaxial anisotropies: A Monte Carlo study, J. Appl. Phys. **114**, 143904 (2013).

[120] E. Restrepo-Parra, G. Orozco-Hernandez, and J. C. Riano-Rojas, Monte Carlo simulation of surface anisotropy in La2/3Ca1/3MnO3 nanoparticles, J. Magn. Magn. Mater. **344**, 44 (2013).

[121] Y. Labaye, O. Crisan, L. Berger, J. M. Greneche, and J. M. D. Coey, Surface anisotropy in ferromagnetic nanoparticles, J. Appl. Phys. **91**, 8715 (2002).

[122] E. De Biasi, C. A. Ramos, R. D. Zysler, and H. Romero, Large surface magnetic contribution in amorphous ferromagnetic nanoparticles, Phys. Rev. B **65**, 144416 (2002).

[123] J. Mazo-Zuluaga, J. Restrepo, and J. Mejia-Lopez, Effect of surface anisotropy on the magnetic properties of magnetite nanoparticles: A Heisenberg-Monte Carlo study, J. Appl. Phys. **103**, 113906 (2008).

[124] J. Mazo-Zuluaga, J. Restrepo, and J. Mejia-Lopez, Surface anisotropy of a Fe3O4 nanoparticle: A simulation approach, Physica B-Condensed Matter **398**, 187 (2007).

[125] G. Salazar-Alvarez, J. Qin, V. Sepelak, I. Bergmann, M. Vasilakaki, K. N. Trohidou, J. D. Ardisson, W. A. A. Macedo, M. Mikhaylova, M. Muhammed, M. D. Baro, and J. Nogues, Cubic versus spherical magnetic nanoparticles: The role of surface anisotropy, J. Am. Chem. Soc. **130**, 13234 (2008).

[126] R. Yanes, O. Chubykalo-Fesenko, R. F. L. Evans, and R. W. Chantrell, Temperature dependence of the effective anisotropies in magnetic nanoparticles with Neel surface anisotropy, J. Phys. D Appl. Phys. **43**, 474009 (2010).

[127] O. Iglesias and A. Labarta, Finite-size and surface effects in maghemite nanoparticles: Monte Carlo simulations, Phys. Rev. B **63**, 184416 (2001).

[128] L. Berger, Y. Labaye, M. Tamine, and J. M. D. Coey, Ferromagnetic nanoparticles with strong surface anisotropy: Spin structures and magnetization processes, Phys. Rev. B **77**, 104431 (2008).

[129] P. Asselin, R. F. L. Evans, J. Barker, R. W. Chantrell, R. Yanes, O. Chubykalo-Fesenko, D. Hinzke, and U. Nowak, Constrained Monte Carlo method and calculation of the temperature dependence of magnetic anisotropy, Phys. Rev. B **82**, 054415 (2010).

[130] H. Y. Lv, Y. K. Lei, A. Datta, and G. F. Wang, Influence of surface segregation on magnetic properties of FePt nanoparticles, Appl. Phys. Lett. **103**, 132405 (2013).

[131] J. M. Montejano-Carrizales, F. Aguilera-Granja, C. Goyhenex, V. Pierron-Bohnes, and J. L. Moran-Lopez, Structural, electronic and magnetic properties of ConPtM-n for M=13, 19, and 55, from first principles, J. Magn. Magn. Mater. **355**, 215 (2014).

[132] M. F. Chi, C. Wang, Y. K. Lei, G. F. Wang, D. G. Li, K. L. More, A. Lupini, L. F. Allard, N. M. Markovic, and V. R. Stamenkovic, Surface faceting and elemental diffusion behaviour at atomic scale for alloy nanoparticles during in situ annealing, Nat. Commun. **6**, 8925 (2015).

[133] D. A. Garanin and H. Kachkachi, Surface contribution to the anisotropy of magnetic nanoparticles, Phys. Rev. Lett. **90**, 065504 (2003).

[134] H. Kachkachi and E. Bonet, Surface-induced cubic anisotropy in nanomagnets, Phys. Rev. B **73**, 224402 (2006).

[135] L. Suber and D. Peddis, in Magnetic Nanomaterials, edited by C. S. S. R. Kumar (Wiley-VCH, Weinheim, Germany, 2011).

[136] V. Dupuis, G. Khadra, S. Linas, A. Hillion, L. Gragnaniello, A. Tamion, J. Tuaillon-Combes, L. Bardotti, F. Tournus, E. Otero, P. Ohresser, A. Rogalev, and F. Wilhelm, Magnetic moments in chemically ordered mass-selected CoPt and FePt clusters, J. Magn. Magn. Mater. **383**, 73 (2015).

[137] V. Zolyomi, L. Vitos, S. K. Kwon, and J. Kollar, Surface relaxation and stress for 5d transition metals, J. Phys.: Condens. Mat. **21**, 095007 (2009).

[138] R. Guirado-Lopez, Magnetic anisotropy of fcc transition-metal clusters: Role of surface relaxation, Phys. Rev. B **63**, 174420 (2001).

[139] J. F. v. d. Veen and M. A. Van Hove, The Structure of surfaces II : proceedings of the 2nd International Conference on the Structure of Surfaces (ICSOS II), Amsterdam, The Netherlands, June 22-25, 1987 (Springer Science & Business Media, 1988).

[140] I. G. Rau, S. Baumann, S. Rusponi, F. Donati, S. Stepanow, L. Gragnaniello, J. Dreiser, C. Piamonteze, F. Nolting, S. Gangopadhyay, O. R. Albertini, R. M. Macfarlane, C. P. Lutz, B. A. Jones, P. Gambardella, A. J. Heinrich, and H. Brune, Reaching the magnetic anisotropy limit of a 3d metal atom, Science **344**, 988 (2014).

[141] I. E. Dzialoshinskii, Thermodynamic Theory of Weak Ferromagnetism in Antiferromagnetic Substances, Sov. Phys. Jetp-Ussr **5**, 1259 (1957).

[142] T. Moriya, Anisotropic Superexchange Interaction and Weak Ferromagnetism, Phys. Rev. **120**, 91 (1960).

[143] M. Heide, G. Bihlmayer, P. Mavropoulos, A. Bringer, and S. Blügel, Spin Orbit Driven Physics at Surfaces, Newsletter of the Psi-K Network **78** (2006).

[144] A. V. Ruban, H. L. Skriver, and J. K. Norskov, Surface segregation energies in transition-metal alloys, Phys. Rev. B **59**, 15990 (1999).

[145] D. S. Wang, R. Q. Wu, and A. J. Freeman, 1st-Principles Theory of Surface Magnetocrystalline Anisotropy and the Diatomic-Pair Model, Phys. Rev. B **47**, 14932 (1993).

[146] S. Brahimi, H. Bouzar, and S. Lounis, Giant perpendicular magnetic anisotropy energies in CoPt thin films: impact of reduced dimensionality and imperfections, J. Phys.: Condens. Mat. **28**, 496002 (2016).

[147] T. R. Dasa, P. A. Ignatiev, and V. S. Stepanyuk, Effect of the electric field on magnetic properties of linear chains on a Pt(111) surface, Phys. Rev. B **85**, 205447 (2012).

[148] D. Odkhuu, Magnetization reversal of giant perpendicular magnetic anisotropy at the magnetic-phase transition in FeRh films on MgO, Phys. Rev. B **93**, 064412 (2016).

[149] Y. Kota and A. Sakuma, Relationship between Magnetocrystalline Anisotropy and Orbital Magnetic Moment in L1(0)-Type Ordered and Disordered Alloys, J. Phys. Soc. Jpn. **81**, 084705 (2012).

[150] G. Henkelman, A. Arnaldsson, and H. Jonsson, A fast and robust algorithm for Bader decomposition of charge density, Comp. Mater. Sci. **36**, 354 (2006).

[151] R. Singh and P. Kroll, Structural, electronic, and magnetic properties of 13-, 55-, and 147-atom clusters of Fe, Co, and Ni: A spin-polarized density functional study, Phys. Rev. B **78**, 245404 (2008).

[152] S. E. Apsel, J. W. Emmert, J. Deng, and L. A. Bloomfield, Surface-enhanced magnetism in nickel clusters, Phys. Rev. Lett. **76**, 1441 (1996).

[153] J. Souto-Casares, M. Sakurai, and J. R. Chelikowsky, Structural and magnetic properties of large cobalt clusters, Phys. Rev. B **93**, 174418 (2016).

[154] Z. Liu, Y. Lei, and G. Wang, First-principles computation of surface segregation in L1(0) CoPt magnetic nanoparticles, J. Phys.: Condens. Mat. **28**, 266002 (2016).

[155] Z. Liu and G. Wang, Surface magnetism of L1 0 CoPt alloy: First principles predictions, J. Phys.: Condens. Mat. **29**, 355801 (2017).

[156] H. Lv, Y. Lei, A. Datta, and G. Wang, Influence of surface segregation on magnetic properties of FePt nanoparticles, Appl. Phys. Lett. **103**, 132405 (2013).

[157] S. Bhattacharjee, S. J. Yoo, U. V. Waghmare, and S. C. Lee, NH3 adsorption on PtM (Fe, Co, Ni) surfaces: Cooperating effects of charge transfer, magnetic ordering and lattice strain, Chem. Phys. Lett. **648**, 166 (2016).

[158] P. A. Lindgard and P. V. Hendriksen, Estimation of Electronic and Structural Influence on the Thermal Magnetic-Properties of Clusters, Phys. Rev. B **49**, 12291 (1994).

[159] R. L. Snyder, V. Q. Nguyen, and R. V. Ramanujan, Design parameters for magneto-elastic soft actuators, Smart Mater. Struct. **19**, 055017 (2010).

[160] D. C. Jiles and C. C. H. Lo, The role of new materials in the development of magnetic sensors and actuators, Sensor Actuat. A-Phys. **106**, 3 (2003).

[161] M. R. J. Gibbs, Modern trends in magnetostriction study and application (Springer Science & Business Media, 2001).

[162] Y. X. Yu, J. Shi, and Y. Nakamura, Enhancement of perpendicular coercivity for CoPt top layer in CoPt/AIN multilayer structure, J. Appl. Phys. **108**, 023912 (2010).

[163] J. Rouchy and A. Waintal, Elastic-Constants of Ordered and Disordered Crystallographic Ptco Phases, Solid State Commun. **17**, 1227 (1975).

[164] H. Takahashi, S. Tsunashima, S. Iwata, and S. Uchiyama, Measurement of Magnetostriction Constants in Polycrystalline Alloy and Multilayer Films of Pdco and Ptco, J. Magn. Magn. Mater. **126**, 282 (1993).

[165] J. A. Aboaf, T. R. Mcguire, S. R. Herd, and E. Klokholm, Magnetic, Transport, and Structural-Properties of Iron-Platinum Thin-Films, IEEE Trans. Magn. **20**, 1642 (1984).

[166] F. E. Spada, F. T. Parker, C. L. Platt, and J. K. Howard, X-ray diffraction and Mossbauer studies of structural changes and L1(0) ordering kinetics during annealing of polycrystalline Fe51Pt49 thin films, J. Appl. Phys. **94**, 5123 (2003).

[167] N. Sehdev, R. Medwal, and S. Annapoorni, Enhanced phase stabilization of CoPt in the presence of Ag, J. Appl. Phys. **110**, 033901 (2011).

[168] T. T. Huang, F. Wang, J. H. Guo, and X. H. Xu, Effect of Cu additive on the structure and magnetic properties of (CoPt)(1-x)Cu-x films, Rare Metals **28**, 14 (2009).

[169] N. Sehdev, R. Medwal, and S. Annapooni, Ag assisted evolution of ordered L1(0) CoPt alloy nanoparticles, J. Alloy. Compd. **522**, 85 (2012).

[170] Y. X. Wang, X. L. Zhang, Y. Liu, S. Q. Lv, Y. H. Jiang, Y. J. Zhang, H. L. Liu, Y. Q. Liu, and J. H. Yang, L1(0) CoPt-Cu nanoparticles for high-density magnetic recoding by sol-gel technique, J. Alloy. Compd. **582**, 511 (2014).

[171] C. L. Platt, K. W. Wierman, E. B. Svedberg, R. van de Veerdonk, J. K. Howard, A. G. Roy, and D. E. Laughlin, L1(0) ordering and microstructure of FePt thin films with Cu, Ag, and Au additive, J. Appl. Phys. **92**, 6104 (2002).

[172] T. Yokota, L. Gao, S. H. Liou, M. L. Yan, and D. J. Sellmyer, Effect of Au spacer layer on L1(0) phase ordering temperature of CoPt thin films, J. Appl. Phys. **95**, 7270 (2004).

[173] T. Maeda, T. Kai, A. Kikitsu, T. Nagase, and J. Akiyama, Reduction of ordering temperature of an FePt-ordered alloy by addition of Cu, Appl. Phys. Lett. **80**, 2147 (2002).

[174] S. S. Kang, D. E. Nikles, and J. W. Harrell, Synthesis, chemical ordering, and magnetic properties of self-assembled FePt-Ag nanoparticles, J. Appl. Phys. **93**, 7178 (2003).

[175] L. Vitos, A. V. Ruban, H. L. Skriver, and J. Kollar, The surface energy of metals, Surf. Sci. **411**, 186 (1998).

[176] I. Karakaya and W. Thompson, The Ag− Co (Silver-Cobalt) system, Bulletin of Alloy Phase Diagrams **7**, 259 (1986).

[177] H. Okamoto, T. Massalski, T. Nishizawa, and M. Hasebe, The Au-Co (gold-cobalt) system, Bulletin of Alloy Phase Diagrams **6**, 449 (1985).

[178] H. Okamoto and T. Massalski, The Au− Pt (Gold-Platinum) system, J. Phase Equilb. **6**, 46 (1985).

[179] L. Swartzendruber, The Ag− Fe (Silver-Iron) system, Bulletin of Alloy Phase Diagrams **5**, 560 (1984).

[180] H. Okamoto, T. Massalski, L. Swartzendruber, and P. Beck, The Au− Fe (gold-iron) system, Bulletin of Alloy Phase Diagrams **5**, 592 (1984).

[181] T. Nishizawa and K. Ishida, The Co− Cu (Cobalt-Copper) system, J. Phase Equilb. **5**, 161 (1984).

[182] Q. Chen and Z. Jin, The Fe-Cu system: A thermodynamic evaluation, METALL. MATER. TRANS. A **26**, 417 (1995).

[183] G. L. Hart, L. J. Nelson, R. R. Vanfleet, B. J. Campbell, M. H. Sluiter, J. H. Neethling, E. J. Olivier, S. Allies, C. I. Lang, and B. Meredig, Revisiting the revised Ag-Pt phase diagram, Acta Mater. **124**, 325 (2017).

[184] T. Abe, B. Sundman, and H. Onodera, Thermodynamic assessment of the Cu− Pt system, J. Phase Equilib. Diff. **27**, 5 (2006).

[185] L. D. Landau and E. Lifshitz, On the theory of the dispersion of magnetic permeability in ferromagnetic bodies, Phys. Z. Sowjet. **8**, 153 (1935).

[186] T. L. Gilbert, A phenomenological theory of damping in ferromagnetic materials, IEEE Trans. Magn. **40**, 3443 (2004).